UPPSALA
UNIVERSITET

Digital Comprehensive Summaries of Uppsala Dissertations from the Faculty of Science and Technology 2055

Structural, Electronic and Reactive Properties of Pentapyridyl - Base Metal Complexes

Relevance for Water Oxidation Catalysis

MANUEL BONIOLO

ACTA
UNIVERSITATIS
UPSALIENSIS
UPPSALA
2021

ISSN 1651-6214
ISBN 978-91-513-1248-4
URN urn:nbn:se:uu:diva-447009

Dissertation presented at Uppsala University to be publicly examined in Siegbahnsalen, Ångströmlaboratoriet, Lägerhyddsvägen 1, Uppsala län, Friday, 10 September 2021 at 13:00 for the degree of Doctor of Philosophy. The examination will be conducted in English. Faculty examiner: Antoni Llobet (Institut Català d'Investigació Química).

Abstract

Boniolo, M. 2021. Structural, Electronic and Reactive Properties of Pentapyridyl - Base Metal Complexes. Relevance for Water Oxidation Catalysis. *Digital Comprehensive Summaries of Uppsala Dissertations from the Faculty of Science and Technology* 2055. 146 pp. Uppsala: Acta Universitatis Upsaliensis. ISBN 978-91-513-1248-4.

The rationalization of chemical-physical proprieties of transition metal complexes is fundamental in order to understand and tune their reactivity. In this thesis, a systematic investigation of the geometrical and electronic properties of $[M(Py5OH)Cl]^+$ complexes (M= Mn, Fe, Co, Ni) has been performed, and their ability to act as molecular water oxidation catalysts has been probed. Through this scientific journey, new insights into their chemical and physical properties have been revealed. The spin crossover behavior of the ferrous chloride complex ($[Fe(Py5OH)Cl]PF_6$) is the first example of a molecular Fe(II) complex coordinated to a weak-field ligand that can be thermodynamically stable in a low-spin electron configuration (Chapter 3). The spin state also dictates the electrochemical proprieties of the one-electron oxidized state of all the metal complexes investigated in our study (Chapter 4). The atypical rhombicity of the manganese complex ($[Mn(Py5OH)Cl]PF_6$) gives an unusual anisotropic EPR signal for a Mn(II, S = 5/2) complex. This is compared with the analog $[Mn(Py5OMe)Cl]PF_6$ complex providing, in combination with DFT calculations, insight into how the magnetic parameters (i.e., zero field splitting) are affected by small structural changes (Chapter 5). Finally, I investigated the role of water as substrate for water oxidation catalysis with the $[M(Py5OH)Cl]^+$ complexes. The addition of small amounts of water into a non-aqueous medium allowed trapping possible water-bound intermediates for the Fe complex in the M(III) oxidation state but not for the other complexes. Nevertheless, all Py5OH-metal complexes are not particularly active catalysts with a maximum turnover number (TON) of 2. By introducing two methoxy functional groups, we obtained $[Fe(Py5OMe)Cl]^+$ that turns out to facilitate water oxidation catalysis with a TON = 133 in a light-driven experiment. Further electrochemical experiments and post-catalytic solution analysis reveals that the oxygen evolution is generated by iron oxo/hydroxo species formed from the degradation of the methoxy-substituted Fe complex. This study highlights the difficulty of obtaining a stable base metal molecular catalyst and the importance of conducting a multi-technique analysis to attest firmly the nature of the catalysis (Chapter 6).

Keywords: Water oxidation, Base metal complexes, Redox potential, Spin crossover, Magnetic anisotropy

Manuel Boniolo, Department of Chemistry - Ångström, Molecular Biomimetics, Box 523, Uppsala University, SE-75120 Uppsala, Sweden.

© Manuel Boniolo 2021

ISSN 1651-6214
ISBN 978-91-513-1248-4
URN urn:nbn:se:uu:diva-447009 (http://urn.kb.se/resolve?urn=urn:nbn:se:uu:diva-447009)

To my family

List of Papers

This thesis is based on the following papers, which are referred to in the text by their Roman numerals.

I. Boniolo, M.; Shylin, S. I.; Chernev, P.; Cheah, M. H.; Heizmann, P. A.; Huang, P.; Salhi, N.; Hossain, K.; Thapper, A.; Lundberg, M.; Messinger, J.; (2020) Spin Transition in a Ferrous Chloride Complex Supported by a Pentapyridine Ligand. *Chem. Commun. 56* (18), 2703-2706.
Author's contribution: Performed the synthesis of the complex. Discovered the color change of the complex upon freezing. Participated in the SQUID and XAS experiments. Contributed to the writing of the paper and prepared the figures, as well as the journal cover.

II. Boniolo, M.; Chernev, P.; Cheah, M. H.; Heizmann, P. A.; Huang, P.; Shylin, S. I.; Salhi, N.; Hossain, M. K.; Gupta, A. K.; Messinger, J.; Thapper, A.; Lundberg, M.; (2021) Electronic and Geometric Structure Effects on One-Electron Oxidation of First-Row Transition Metals in the Same Ligand Framework. *Dalton. Trans. 50* (2), 660-674.
Author's contribution: Contributed to the planning of the project. Performed the synthesis and characterization of the complexes. Carried out and analyzed the electrochemical and UV/Vis experiments and participated in the XAS experiments. Made major contributions to the layout and writing of the paper, designed and prepared the figures, and led the submission process.

III. Huang, P.; Boniolo, M.; Rapatskiy, L.; Salhi N.; Chernev, P.; Cheah, M. H.; Shylin, S. I.; Hossain, M. K.; Thapper, A.; Schnegg, A.; Messinger J.; Lundberg M.; Exploring the Relations Between Orbital Energies, Redox Potentials, and Zero-Field Splitting Parameters in a Mn(II)-Py5OH-Cl Complex and its Methylated Analog. (Manuscript)
Author's contribution: Contributed to the planning of the project.

Performed the synthesis and characterization of the complexes. Carried out and analyzed the electrochemical experiments, participated in XAS experiments, and initiated EPR measurements. Contributed to the writing of the text and edited the figures.

IV. Boniolo, M.; Hossain, M. K.; Chernev, P.; Suremann N. F.; Heizmann, P.; Lyvik A.S.; Beyer, P.; Mebs, S.; Shylin, S. I.; Huang, P.; Salhi, N.; Cheah, M. H.; Lundberg, M.; Thapper, A.; Messinger J.; Pentapyridyl Base Metal Complexes: Apical Ligand Exchange, Redox Potential, Stability and Water Oxidation. (Manuscript)
Author's contribution: Contributed to the planning of the project. Performed the synthesis and characterization of the complexes. Carried out and analyzed the electrochemical experiments and participated in the XAS experiments. Optimized, performed, and analyzed the different water oxidation experiments. Wrote the manuscript with input from the other authors, and designed and prepared the figures.

Papers not included in this thesis

I. Kawde, A.; Annamalai, A.; Amidani, L.; Boniolo, M.; Kwong, W. L., Sellstedt, A.; Glatzel, P.; Wågberg T.; Messinger, J.; Photo-electrochemical Hydrogen Production from Neutral Phosphate Buffer and Seawater Using Micro-Structured p-Si Photo-Electrodes Functionalized by Solution-Based Methods; (2018) *Sustain. Energy Fuels*, (2), 2215-2223.
Author's contribution: Contributed to hydrogen and oxygen evolution measurements.

Contents

Chapter 1 Introduction 17
- 1.1 Motivation 17
- 1.2 The water-splitting reaction and its catalysis 20
  - 1.2.1 How water-splitting is energetically driven in studying artificial systems 22
  - 1.2.2 Mechanism of the O–O bond formation 24
- 1.3 Natural Photosynthesis 25
- 1.4 Artificial Photosynthesis using rare metals 31
  - 1.4.1 From where all started. Ruthenium-based molecular water oxidation catalysts 31
  - 1.4.2 The birth of mono-metallic complexes as water oxidation catalysts 33
  - 1.4.3 Iridium based complexes 35
- 1.5 Artificial Photosynthesis using base metals 36
  - 1.5.1 Manganese 36
  - 1.5.2 Iron 38
  - 1.5.3 Cobalt 40
  - 1.5.4 Nickel 41
- 1.6 The flexibility of the Pentapyridyl – Py5 – scaffold 42
- 1.7 Aim of the thesis 44

Chapter 2 Materials and Methods 45
- 2.1 Synthesis and characterization 45
  - 2.1.1 Py5OH: the design of a new synthetic route 45
  - 2.1.2 Py5OMe 47
  - 2.1.3 Synthesis of the chloride ligated complexes $[M^{II}(Py5OH)Cl]PF_6$ and $[M^{II}(Py5OMe)Cl]PF_6$ 48
  - 2.1.4 Synthesis of $[Fe^{II}(Py5OH)Solv](ClO_4)_2$ 48
  - 2.1.5 Synthesis of $[Ru^{II}(bpy)_3](ClO_4)_2$ and $[Ru^{III}(bpy)_3](ClO_4)_3$ 49
- 2.2 X-ray techniques 50
  - 2.2.1 XAS 50
  - 2.2.2 XPS 52
  - 2.2.3 XRD 52

2.3 Magnetic methods 53
  2.3.1 EPR 53
  2.3.2 SQUID and the Spin crossover 56
2.4 Computational methods 57
  2.4.1 General introduction 57
  2.4.2 DFT procedure 60
2.5 Electrochemical method 61
  2.5.1 General introduction of cyclic voltammetry 62
  2.5.2 CV's experimental details 63
  2.5.3 Controlled potential electrolysis 65
2.6 O_2 detection 67

Chapter 3 An Unexpected Spin Crossover Behavior 71
3.1 Introduction 71
3.2 SQUID measurement 73
3.3 XAS measurements 74
3.4 DFT calculations 75
3.5 Conclusion 76

Chapter 4 Electrochemical and Structural Overview of Base Metal Py5OH Complexes 77
4.1 Introduction 77
4.2 Structural trends of M^{II} complexes and the molecular orbital configuration 78
4.3 Solvent effects 80
4.4 Structural trends of the oxidized M^{III} complexes 81
4.5 Trends of the experimental redox potentials 82
4.6 Apical ligand exchange 84
4.7 Comparison with the $[M(Py5OMe)Cl]^+$ complexes 86
4.8 Conclusion 88

Chapter 5 Magnetic Anisotropy of Mn-Py5-Cl Complexes 91
5.1 Introduction 91
5.2 X-band EPR 92
5.3 W-band EPR 94
5.4 EPR simulations 95
5.5 DFT calculations 95
5.6 Conclusion 96

Chapter 6 Base Metal Pentapyridyl Complexes: Do they Work as Molecular WOCs? 99
6.1 Introduction 99
6.2 Water addition effect on the redox behavior 100

6.3 XAS analysis on the reduced and oxidized compounds 103
6.4 Water oxidation activity 106
6.5 Molecular catalysis versus iron nanoparticles 109
6.6 Conclusion 112

Chapter 7 Summary 115

Abbreviations

ATP	adenosine triphosphate
bpm	2,2´-bipyrimidine
bpp	3,5-bis(2-pyridyl)pyrazolate
bpy	2,2’-bipyridine
BQCN	N,N’-dimethyl-N,N’-bis(8-quinolyl)-cyclohexanediamine
BQEN	N,N’-dimethyl-N,N’-bis(8-quinolyl)-ethane-1,2-diamine
BuCN	butyronitrile
CAN	ceric ammonium nitrate
CGTO	contracted Gaussian type orbital
Cp*	cyclopentadienyl
CPE	controlled potential electrolysis
CV	cyclic voltammetry
CyT	cytochrome
DCM	dichloromethane
DFT	density functional theory
DLS	dynamic light scattering
DMF	dimethylformamide
DZ	double zeta
EPR	electron paramagnetic resonance
EXAFS	extended X-ray absorption fine structure
Fc	ferrocene
FeOOH	iron oxo/hydroxo species
FRET	Förster resonance energy transfer
FT-IR	Fourier-transform infrared (spectroscopy)
GC	glassy carbon
GGA	generalized gradient approximation
GTO	Gaussian type orbital
HF	Hartree-Fock
HFHF	high-field high-frequency
HS	high spin
I2M	coupling of two metal-oxyl radicals
IPCC	intergovernmental panel on climate change
KS	Kohn-Sham
LDA	local density approximation
LS	low spin

MeCN	acetonitrile
MeOH	methanol
MO	molecular orbital
mox	N^1,N$^{1\prime}$- (1,2-phenylene)bis(N^2-methyloxalamide)
MS	mass spectrometer/spectrometry
NADPH	nicotinamide-adenine dinucleotide phosphate
n-Buli	*n*-butyl-lithium
NMR	nuclear magnetic resonance
OEC	oxygen evolving complex in photosystem II
PC	plastocyanin
PCET	proton coupled electron transfer
PCM	polarizable continuum models
PGTO	primitive Gaussian type orbital
POM	polyoxometalate
ppy	2-(2-phenylido)pyridine
PQ	plastoquinone
PSI	photosystem I
PSII	photosystem II
Py	pyridine
Py5	pentapyridyl
Py5Me	2,6-bis(1,1-bis(2-pyridyl)ethyl)pyridine
Py5OH	pyridine-2,6-diylbis[di-(pyridin-2-yl)methanol
Py5OMe	pyridine-2,6-diylbis[di-(pyridin-2-yl)methoxymethane
RVC	reticulated vitreous carbon
R.T.	room temperature
SCF	self-consistent field
SCO	spin crossover
SHE	standard hydrogen electrode
SMD	solvation model based on density
SOC	spin-orbit coupling
SQUID	superconductive quantum interference device
SS	spin-spin interaction
SMM	single molecule magnet
SV	split-valence
TAML	tetra-amido macrocycles ligand
TBACl	tetrabutylammonium chloride
TBAPF$_6$	tetrabutylammonium hexafluorophosphate
THF	tetrahydrofurane
TLC	thin layer chromatography
TOF	turnover frequency
TON	turnover number
tpm	tris(2-pyridylmethane)
tpy / trpy	2,2';6',2"-terpyridine
TR-MIMS	time-resolved membrane inlet mass spectrometry

TZ	triple zeta
UV-Vis	ultraviolet-visible (spectroscopy)
WNA	water nucleophilic attack
WOC	water oxidation catalyst
XANES	X-ray absorption near edge structure
XAS	X-ray absorption spectroscopy
XPS	X-ray photoelectron spectroscopy
XRD	X-ray diffraction
ZFS	zero field splitting

Chapter 1

Introduction

> "On the arid lands there will spring up industrial colonies without smoke and without smokestacks; forests of glass tubes will extend over the plains and glass buildings will rise everywhere; inside of these will take place the photochemical processes that hitherto have been the guarded secret of the plants, but that will have been mastered by human industry which will know how to make them bear even more abundant fruit than nature, for nature is not in a hurry and mankind is. And if in a distant future the supply of coal becomes completely exhausted, civilization will not be checked by that, for life and civilization will continue as long as the sun shines".[1]
>
> Giacomo Ciamician 1912

1.1 Motivation

The technological progress of humankind has been connected with the exploitation of nature. Perhaps the first example is the invention of agriculture dated approximately 10 000 BC, i.e., the beginning of the Neolithic age.[2] Nevertheless, the domestication of animals, soil usage, and deforestation did not have global effects because of its small scale compared to nature's ability for regeneration. A drastic change occurred in the nineteenth century with the start of the industrial revolution. New technologies allowed replacing human power with machines fed by fossil fuels. These innovations scaled up the production of goods and fertilizers, enabling an increased food production that supported a drastic growth of the world population and further demand for energy. It is from this point in history that the fragile equilibrium between humankind and nature started to break. The use of energy from fossil carbon resources resulted in increased concentrations of 'greenhouse gases' such as carbon dioxide, methane, and nitrous oxides. Greenhouse gases absorb infrared radiation emitted from the Earth's surface that otherwise would be dissipated into space.[3] The absorbed energy is partially emitted back to Earth, causing an increase in the planet's temperature.

The 5th IPCC assessment (Intergovernmental Panel on Climate Change), published by the United Nations in 2014, has shown the tight correlation between the increase of the average temperature (Figure 1.1a), the sea level rise due to polar ice and glacier melting (Figure 1.1b), the greenhouse gas concentration (Figure 1.1c) and the anthropogenic carbon dioxide emission (Figure 1.1d) compared to pre-industrial levels. A recent study reported how the slow but constant melting of the polar ice-cap since 1990 had drifted the Earth's rotation axis at a rate of 3.26 mm per year due to the redistribution of the water mass. In the long run, this will lead to additional changes in climate.[4]

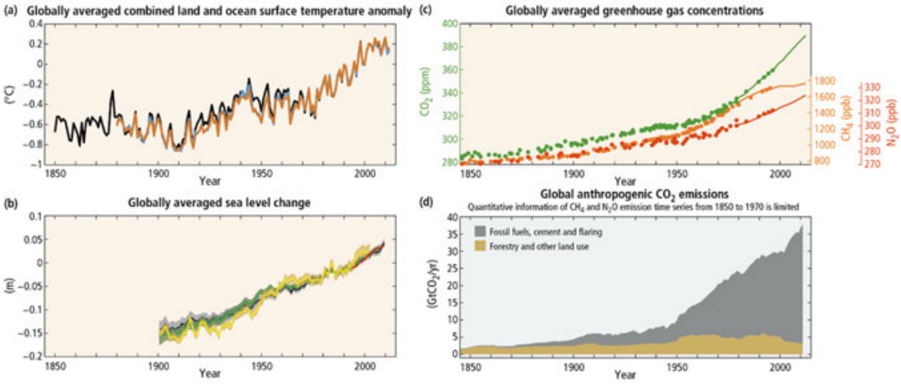

Figure 1.1 *– The tight relation between climate changing phenomena (a and b) and the increasing greenhouse gas emissions (c and d) from the pre-industrial era. Reproduced with permission from the 5th IPCC assessment, 2014.*

Sadly, the number of disasters caused by extreme weather conditions has increased dramatically in the last decades, with abrupt changes between drought and sudden heavy rain periods, winter storms, and wildfire. If the temperature continues to rise, these atmospheric events will become even more frequent with serious social-economic consequences, starvation in emerging countries and many lives lost. The threshold for the temperature rise above pre-industrial levels has been estimated, by the 5th IPCC assessment, to 2 °C. This is the 'point of no return', i.e., the maximum positive temperature anomaly; beyond this point, it will no longer be possible to restore the initial climate equilibrium.[3, 5] In 2015, the Paris agreement had the ambitious goal to limit the temperature increase to 1.5 °C by imposing a legal binding to the 196 nations which have signed the pact. Despite the efforts of many countries to promote a transition into a carbon-free economy, the concentration of carbon dioxide in the atmosphere reached 409 ppm in 2019.[6] In 2020, the Covid-19 pandemic crisis has reduced carbon emissions by 5.8%.[7] However, the same year has also been the second warmest with a temperature anomaly of +1.27 °C.[8] The newly calculated rate for the temperature rise is 0.25–0.32 °C per decade, as compared to 0.20 °C predicted in 2014 by the IPCC.[9] At this pace, the warning limit of 1.5 °C could be reached by 2030.[10]

Paradoxically, the emission of other pollutants that are no greenhouse gases but which damage crops, vegetation and negatively affect public health in local geographic areas can have slowed the global temperature rise. A study reported by Salzmann highlights how anthropogenic aerosols scatter the sunlight and thereby may have helped to slow the temperature rise on our planet.[11,10] In this way, the sulfur dioxide emission from China's coal power plants may have masked climate change for a while, and the reduction of these emissions by 7-14% between 2014 and 2016 may now lead to a faster change.[12]

The reasons behind the slower than predicted climate change until 2020 may, in part, also be connected to natural phenomena. For example, the Pacific Ocean undergoes a periodic cycle that occurs every two decades with a phenomenon called 'Interdecadal Pacific Oscillation'.[13] We are currently entering a warming-up period that affects the equatorial Pacific and North America temperatures. Likewise, also the mixing of deep and surface water in the oceans was reported to slow down with the consequent release of heat into the atmosphere.[14]

For the year 2021, a new burst of greenhouse emission is predicted as a response to the end of the Covid-19 pandemic with the consequent growth of energy demand to sustain the global economic recovery. According to the last Energy Review of the International Energy Agency, the global energy demand has grown, on average, by 3% every year since 1990 (excluding 2020). However, for 2021 a rise of at least 6% is predicted due to restarting the economy (Figure 1.2).[15]

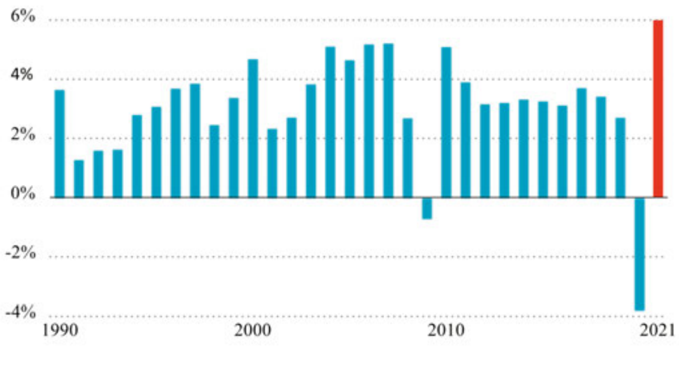

__Figure 1.2__ – Annual rate change in energy demand relative to the previous year. Reproduced with permission from the Energy Review of the International Energy Agency, 2021.

Because of this discouraging forecast, now - more than ever - it is time to find new solutions to sustain the transition into a carbon-free economy. Single countries are independently moving towards this direction with roadmaps to reduce carbon emissions in all the industrial and transportation sectors. In 2020, European Union established the Green Deal, which aims to zero greenhouse gas emissions by 2050. The United States, with the new Biden administration, and China are setting similar goals.

In the last years, electrification in the transportation sector has taken a big leap. The most significant example is the electric car sector, with a sale increase of 43% in 2020 with respect to the previous year.[16] This technology becomes a good choice due to more competitive prices, governmental incentives, the growth of the network of recharging stations, more efficient batteries, and faster-charging technologies. Likewise, industrial activities are aiming towards electrification and decarbonized transformations. According to BP's Energy Outlook, most of the emissions are currently caused by aviation and those industrial sectors that require high-temperature processes, such as in the iron, steel, cement, and chemical industries.[17]

Diversification of energy resources is therefore needed. High-density energy carriers (fuels) are essential whenever high power is required (i.e., metallurgical industry), the connection to a power grid is not possible, and the battery capacity is not sufficient for the type of application (i.e., aviation or maritime transportation).

Hydrogen as an energy carrier is a green solution because the combustion process exhausts only water. Currently, up to 96% of hydrogen production is carbon-based, i.e., it relies on processes such as steam reforming of natural gas and coal gasification.[18, 19] Hydrogen can be produced with high purity and in an eco-friendly fashion from the electrolysis of water (also called water-splitting) with a reaction described in Eq. 1.1

$$2\ H_2O \xrightarrow{237.2\ \mathrm{kJ\ mol^{-1}}} O_2 + 2\ H_2 \qquad \text{Eq. 1.1}$$

Electrolytic hydrogen production is presently economically not competitive for large-scale applications. This is due to the still too high costs for renewable electricity, the low hydrogen evolution rate, and the instability of the electrodes under neutral or acid conditions.[20] Different research fields focus on bringing hydrogen production on a larger scale by developing different technologies like biomass and base metal electrocatalytic cells.

1.2 The water-splitting reaction and its catalysis

Even if Eq.1.1 represents a very basic textbook reaction, the mechanistic aspects of it are complex. The water-splitting reaction is a redox reaction that is composed of two half-cell reactions. The cathodic process (reducing reaction) generates hydrogen from protons and electrons produced by the anodic water oxidation reaction. Therefore, Eq. 1.1 can be divide into:

$2\ H_2O \rightarrow O_2 + 4\ H^+ + 4\ e^-$ Eq. 1.2a

$4\ H^+ + 4\ e^- \rightarrow 2\ H_2$ Eq. 1.2b

Eq. 1.2a implies the scavenging of four electrons and four protons from two water molecules through a process called Proton Coupled Electron Transfer (PCET). The remaining two oxygen atoms are then combined in a dioxygen molecule, O_2. PCET allows reducing the redox potential of subsequent electron transfer events. However, due to the intrinsic proton-coupled nature of the reaction, the thermodynamic potential, which is 1.23 V *vs.* SHE (standard hydrogen electrode) at pH 0, is pH-dependent (Eq.1.3). Therefore, the higher the pH, the lower is the potential required for the water oxidation reaction.

$E = E^0 - 0.059\ pH\ V$ *vs.* SHE Eq. 1.3

While protons can exist freely in solution (as hydrated form H_3O^+) and the hydrogen evolution is a two-protons-two-electrons process, O^{2-} is highly reactive, and the oxidation of two water molecules must happen in the same reaction cite.

Because of the mechanistic complexity of this reaction, an energetic activation barrier is present. This is often referred to the kinetic energy or overpotential, and it is the extra energy added to the thermodynamic energy of Eq. 1.1. Therefore, a mediator species (catalyst) is needed for both reactions to reduce the overpotential. Its role is to: (i) coordinate the substrate species (i.e., protons or waters molecules); (ii) activate the substrate by imposing electronic and geometric constraints; (iii) guide electron and proton transfer in a stepwise manner; (iv) stabilize the intermediate species with decreasing energetic steps to disfavor backwords reactions, (v) release the final product.

Eq. 1.2a is undoubtedly the most challenging reaction, and it is considered the bottleneck of the entire process. Therefore, research has been focused on the anodic reaction side for many years in order to develop efficient water oxidation catalysts (WOCs) as molecular complexes (homogenous catalysts) or modified material interfaces (heterogeneous catalysts).

The latter found significant interest because of their direct applicability in connection with hydrogen evolution electrocatalytic cells. They are primarily based on metal oxides like the classical RuO_2 couple with IrO_x catalyst. Nowadays, the attention moved toward cheaper base metal oxides such as layered double hydroxides made with a combination of Co, Fe, and Ni. [21]Aside from promising results when operating in tuned experimental conditions, most of these catalysts are unstable in neutral or acidic pH due to their oxide nature.

Homogenous catalysis is interesting because of its tunability from a synthetic point of view. This allows the rational design of the structural and electronic propriety through the ligand design and selection of the metal ion, making it possible to select a wide range of pH operativity. Moreover, *in-situ* mechanistic studies by spectroscopic techniques are easily accessible. The main limitation of molecular WOCs is their limited stability under oxidative conditions and the possibility of being easily regenerated. Even if their industrial application is limited, studying a homogenous system is essential as ‘proof of concept’ to understand the mechanisms, which can then be applied in better performing heterogeneous systems.

The anchoring of molecular WOCs onto an electrode surface gives the possibility to create hybrid systems. This concept is considered the link between the two types of catalysis to enhance the respective advantages. However, as will be seen in this thesis, the tuning of the ligand, even in peripherical positions from the reaction center, might result in a drastic change of the chemical-physical proprieties of the molecular complex.

When comparing the activity of molecular WOC, the important parameters are the turnover number (TON) and the turnover frequency (TOF). TON denotes the number of catalytic cycles the molecule undergoes before it inactivates, indicating its stability. TOF represents how fast are the catalytic cycles pointing out the overall activity.

1.2.1 How water-splitting is energetically driven in studying artificial systems

The molecular catalysts reported below are usually tested with three methods that supply the driving force for evaluating molecular catalysts regarding the water oxidation reaction.

Chemical-driven water oxidation. – The most straightforward method uses a chemical oxidant added in significant excess to the molecular complex under investigation. Ceric ammonium nitrate ($Ce(NH_4)_2(NO_3)_6$), also known as CAN or Ce^{IV} is the most widely used oxidant employed for rare metal-based molecular catalysts. It is a one-electron irreversible electron acceptor with a strong UV absorption band, making it suitable for quantitative analysis. Moreover, it has a high oxidation potential of 1.75 V *vs.* SHE, and this makes it the primary choice whenever a new alleged catalyst is synthesized. The main drawback lies in its stability which is guaranteed only for at $pH < 3$. This is not suitable for most of the base metal catalysts.

Sodium periodate ($NaIO_4$) and potassium peroxymonosulfate ($KHSO_5$) are two oxidants employed from acidic to almost neutral pH. The most significant disadvantage is their tendency to transfer an O atom during the oxidation process. This imposes the ^{18}O labeling of the water substrate to ensure the origin of the O_2 produced.

The most used oxidant with regard to base-metal molecular catalysts is ruthenium(III) tris (bipyridine) cation ($[Ru^{III}(bpy)_3]^{3+}$). As CAN, it is a one-electron oxidant with a strong UV-Vis absorption. However, it is stable at pH < 4.0, and the oxidation potential of only 1.21 *vs.* SHE makes it not suitable for testing catalysts with high overpotential in acidic conditions (since the oxidative driving force for water oxidation might not be sufficient).[22] It is therefore employed in neutral or basic pH, where its low stability can be a problem. This is especially the case if catalysts with low efficiency are studied because $[Ru^{III}(bpy)_3]^{3+}$ can oxidized water by itself. Moreover, it has to be used fresh and in pure conditions since it can act as a precursor for forming highly active water oxidation catalysts, such as Ru-oxides and the blue dimer (see Section 1.4.1 below).

Light-driven water oxidation – Inspired by the photosynthetic processes, the oxidant required to drive the catalytic water oxidation can be generated *in situ* by using light, a photosensitizer molecule, and a sacrificial electron acceptor. The most employed assay uses $[Ru^{II}(bpy)_3]^{2+}$ as light absorber and sodium persulfate $S_2O_8^{2-}$ anion. Upon illumination, the triplet excited state $*[Ru^{II}(bpy)_3]^{2+}$ is generated (Eq. 1.4a), which then undergoes oxidative quenching by $S_2O_8^{2-}$ (Eq. 1.4b-c) to yield $[Ru^{III}(bpy)_3]^{3+}$ species. As abovementioned, $[Ru^{III}(bpy)_3]^{3+}$ acts as an oxidant for the catalytic complex under investigation, and after four oxidation equivalents, an oxygen molecule is released (Eq. 1.4d). The performance of this oxidative method is similar to what is observed for the direct addition of the oxidant. However, some complications might arise from the sulfate radical present in the solution (oxidizing potential of ~ 2.5–3.1 V *vs.* SHE),[23] which might contribute to the oxidative degradation of the photosensitizer and the molecular catalyst.[24, 25] Moreover, in the presence of oxygen, the quenching of excited triple-state can compete with the electron transfer to the electron acceptor.[26, 27] Therefore, the relative amount of light, $[Ru^{II}(bpy)_3]^{2+}$, $S_2O_8^{2-}$, and catalytic complex must be tuned to ensure the highest catalytic performance.

$$[Ru^{II}(bpy)_3]^{2+} \xrightarrow{hv} *[Ru^{II}(bpy)_3]^{2+} \qquad \text{Eq. 1.4a}$$

$$*[Ru^{II}(bpy)_3]^{2+} + S_2O_2^{2-} \rightarrow [Ru^{III}(bpy)_3]^{3+} + SO_4^{2-} + SO_4^{\bullet -} \qquad \text{Eq. 1.4b}$$

$$[Ru^{II}(bpy)_3]^{2+} + SO_4^{\bullet -} \rightarrow [Ru^{III}(bpy)_3]^{3+} + SO_4^{2-} \qquad \text{Eq. 1.4c}$$

$$4\ [Ru^{III}(bpy)_3]^{3+} + 2\ H_2O \rightarrow 4\ [Ru^{II}(bpy)_3]^{2+} + 4\ H^+ + O_2 \qquad \text{Eq. 1.4d}$$

Electrochemically-driven water oxidation – Controlled potential electrolysis (CPE) is a ‘clean’ method for testing the performance of new catalysts, which does not require other chemical components, except for the supporting electrolyte. The oxidation reaction occurs on the electrode surface at the fixed overpotential determined by other electrochemical techniques (i.e., cyclic voltammetry). The measured current and the evolved oxygen are compared to obtain the Faradaic efficiency, an important parameter to quantify the relative amount of charges used for the water-to-oxygen conversion. CPE is also essential to demonstrate the suitability of the studied complex for future device applications (i.e., electrocatalytic cells for H_2 production), and it is a recommended technique to increase the interest of a new catalytic compound in the research community. More details on this technique can be found in Section 2.5.3.

1.2.2 Mechanism of the O–O bond formation

An important aspect discussed in this chapter is the proposed elementary reaction pathway for the molecular O–O bond formation. When studying a new molecular WOC, the mechanistic understanding is important because it opens doors for further geometrical and electronic improvements.

In the water nucleophilic attack (WNA) pathway, a water molecule attacks the highly electrophilic oxygen of a metal-oxo group. Molecular WOCs following this mechanism are suitable for electrode functionalization since their reactivity is essentially monometallic.

On the other hand, the intermolecular interaction of two mono radical metal oxides (oxyl radicals) can result in the formation of a peroxo intermediate MOOM. This oxygen coupling reaction (I2M) imposes the participation of two metal centers. However, in multi-metallic complexes, the I2M pathway can occur intramolecularly, as will be seen in Section 1.4.1.

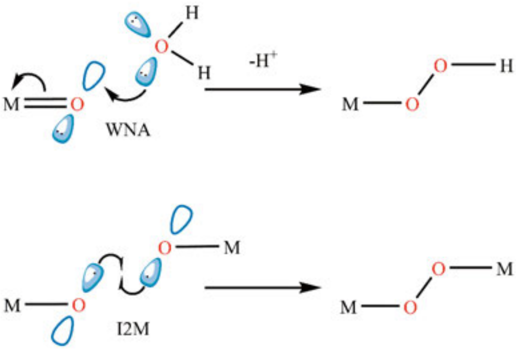

Figure 1.3 *– O–O bond formation pathways.*

The design of new molecular WOCs takes inspiration from the natural photosynthesis reaction. For this reason, it is worthwhile to introduce the functions of the different components of this photo-induced transformation and have a closer look at the metal cofactor that catalyzes the water-splitting reaction. The 'state of the art' of the 'artificial' molecular WOCs will be presented thereafter.

1.3 Natural Photosynthesis

Oxygenic photosynthesis is a photoreaction performed by plants, algae, and cyanobacteria that converts water and carbon dioxide into carbohydrate molecules, whereby oxygen is released as a side-product. This process developed about three billion years ago in predecessors of today's cyanobacteria. Over this long period, primordial photoautotrophic organisms drastically changed the atmospheric composition by injecting a massive amount of oxygen. If at the early stage of the Earth's life the atmosphere was primarily composed of nitrogen, methane, and carbon dioxide, in a few hundred million years, the amount of greenhouse gases reduced, and oxygen became the second most abundant gas (see Figure 1.4).[28, 29] This sudden surge of oxygen concentration caused by cyanobacteria triggered what is called 'the great oxidation event', dated to 2.45 billion years ago. The overshoot of oxygen production caused the oxidation of atmospheric components such as methane and the sudden formation of different oxygen-containing minerals at the Earth's surface.[30] After this short time, nature found a new equilibrium, and multicellular organisms started to develop.[31]

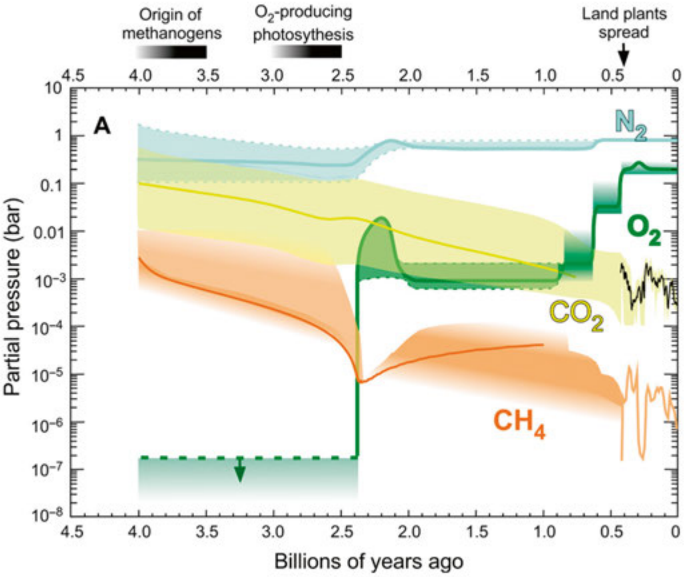

***Figure 1.4** – Timelaps of the atmospheric composition since the first life form. From ref.[29]. Reprinted with permission from AAAS (The Archean atmosphere 2020).*

Oxygenic photosynthesis is a multistep process that uses photons to produce high-energy molecules such as nicotinamide-adenine dinucleotide phosphate (NADPH) and adenosine triphosphate (ATP) that are involved in carbon fixation (in the Calvin-Benson cycle) and other essential metabolic functions. Oxygenic photosynthesis occurs in the thylakoid membranes of chloroplast and cyanobacteria, and it is performed by four transmembrane proteins (see Figure 1.5). The first event occurs in Photosystem II (PSII); here, photons, which are harvested by an antenna system, are used to extract electrons and protons from water. A detailed mechanism will be described further below. While protons are released in the inner membrane side (lumen), electrons are transferred to Photosystem I (PSI). Two mobile carriers accomplish this: plastoquinone (PQ) and plastocyanin (PC), and the cytochrome (Cyt) b_6f complex. The Cyt b_6f complex acts as a 'hub' for the electron and proton transfer from the reduced two-electron carrier PQ (PQH_2) and the one-electron carrier PC, a Cu protein. PQH_2 releases protons into the lumen, and the Cyt b_6f complex pumps one additional proton into the lumen via the Q-cycle. PC carries the electron to the third protein complex, PSI. Here, the reaction center P700 undergoes a photo-induced charge separation. Holes are refilled by electrons carried by PC while the excited electrons are involved in the synthesis of NADPH from NADP$^+$. Finally, ATP is synthesized by the ATP synthase enzyme. The driving force of this reaction comes from the transmembrane proton and electric field gradients formed by the light-induced reactions.[32]

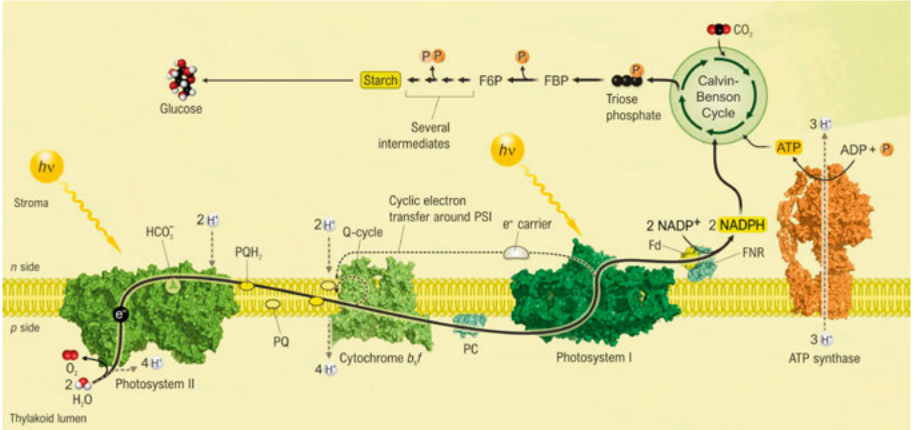
CO$_2$
Calvin-Benson Cycle
Glucose
Starch
P P
F6P
P
FBP
P
Triose phosphate
Several intermediates
hv
hv
3 H$^+$
ATP
ADP + P
Stroma
n side
p side
HCO$_3^-$
2 H$^+$
PQH$_2$
2 H$^+$
Q-cycle
Cyclic electron transfer around PSI
e$^-$ carrier
2 NADP$^+$
2 NADPH
Fd
FNR
e$^-$
PQ
PC
4 H$^+$
Cytochrome b_6f
Photosystem I
3 H$^+$
ATP synthase
O$_2$
2 H$_2$O
4 H$^+$
Photosystem II
Thylakoid lumen

Figure 1.5 *– Schematic overview of the oxygenic photosynthesis occurring in the thylakoid membrane and carbon fixation. Image kindly provided by Dmitry Shevela.*

For the work of this thesis, PSII is undoubtedly the most relevant protein of the oxygenic photosynthesis process. As described above, it accomplishes two redox reactions: the reduction of the plastoquinone and water oxidation. The latter is accomplished by a cofactor known as the Oxygen Evolving Complex

(OEC). The thermodynamic driving force of these two redox reactions is provided by the light energy that is harvested by an antenna system composed of spatially organized pigment molecules (i.e., chlorophylls and carotenoids). The excitation energy is transferred via a Förster Resonance Energy Transfer (FRET) mechanism to the reaction center P680. The resulting excited P680* initiates the charge separation by transferring the excited electron to the neighboring pheophytin molecule. Subsequently, the electron is transferred further to reduce the plastoquinones, PQ_A, and finally PQ_B. Interestingly, the two-electron plastoquinone reduction dictates the turnover frequency of the water oxidation reaction to about 50 O_2 s^{-1}.[33]

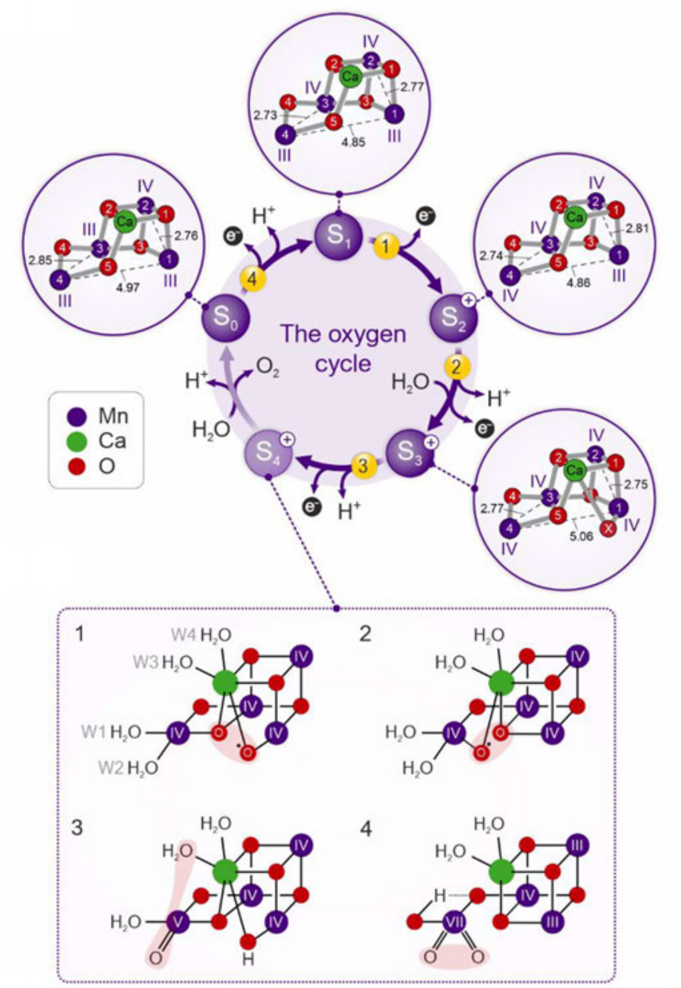
The oxygen cycle
S1
S2
S3
S4
S0
H+
e
O2
H2O
1
2
3
4
Mn
Ca
O
IV
III
V
VII
2.77
2.73
4.85
2.76
2.85
4.97
2.81
2.74
4.86
2.75
2.77
5.06
W4 H2O
W3 H2O
W1 H2O
W2 H2O
H

Figure 1.6 – Kok's cycle of the Mn_4CaO_5 cluster and the structures of its redox state intermediates in photosystem II (PSII). Below currently proposed mechanism for O–O bond formation as explained in the text. Image kindly provided by Dmitry Shevela

The resulting cation radical, P680$^{\bullet+}$, which has the outstanding oxidative potential of 1.2-1.3 V,[34] withdraws an electron from the OEC via the tyrosine residual (Y_Z) of the D1 protein. Importantly, these electron transfer steps on both the acceptor and donor sides of PSII increase the distance between the positive and negative charges and reduce the potential difference. Both allow stabilizing the charge separation for long enough to allow the two slow redox chemical reactions to take place and reduce wasteful and damaging charge recombination reactions.

In 2011, Umena et al. reported the first high-resolution crystal structure (1.9 Å), allowing to describe the geometry and composition of OEC.[35] This cofactor consists of a Mn_4CaO_5 cluster, in which a cubane-like structure is formed by three atoms of manganese (named Mn1–3) and one calcium atom, all linked by oxygen bridges (μ-O). Two μ-O bridges connect the fourth manganese (Mn4) to Mn3 of the cubane structure so that overall a 'chair-like' structure is obtained (Figure 1.6).

As described in Eq. 1.2a, the extraction of four electrons is required to evolve one oxygen molecule. The Mn_4CaO_5 cluster undergoes four oxidation processes before forming the oxygen-oxygen bond. As we will see also for artificial systems, PCET allows accumulating four oxidizing equivalents with similar relative midpoint redox potential in the OEC. This basic concept was proven to occur in the OEC by the four flashes associated with the four oxidation steps needed between oxygen evolution maxima (see Figure 1.7). This allowed formulating the five S-state (redox intermediates) of the so-called Kok cycle in which $S_{0\text{-}3}$ are the four redox intermediates, while S_4 is a transient state (see Figure 1.6).[36, 37]

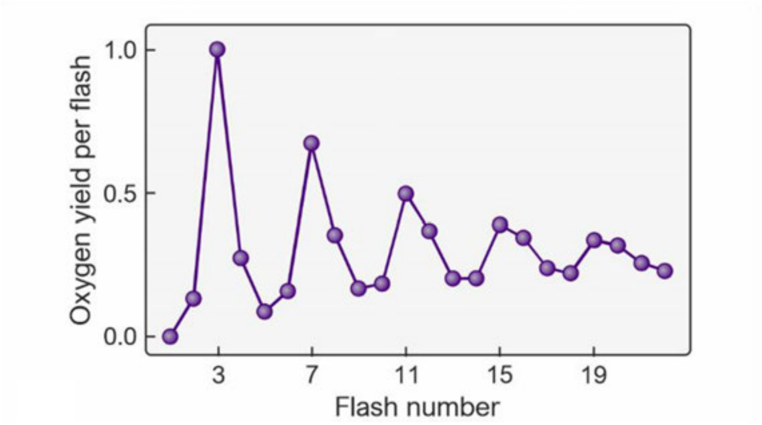

Figure 1.7 *– Flash-induced oxygen yields from dark-adapted PSII samples as a function of flash number. Image kindly provided by Dmitry Shevela*

From S_0 composed by Mn1,3,4(III,III,III) and Mn2(IV), the manganese centers are progressively oxidized during the $S_0 \rightarrow S_3$ transitions to four Mn1-4(IV,IV,IV,IV), whereby the last oxidation step includes the binding of an additional water molecule between Mn1 and Ca. In $S_3 \rightarrow S_4$, this new μ-OH bridge oxidized and deprotonated to form an oxyl radical. Oxygen is formed and released under the binding of a new substrate water molecule during the S_4-S_0 transition. The S_1 state is stable when the sample is dark-adapted, as supported by the finding that only three flashes are required to release the first oxygen molecule (Figure 1.7). For the $S_{0\text{-}3}$ intermediate states, isotopic labeling experiments, X-ray crystal structures, and various spectroscopic techniques (e.g., EPR, XAS) have helped clarify the conformational changes occurring between different intermediate states and identify crucial water molecules as the ultimate substrates for the molecular oxygen formation.[38-40] Unfortunately, the isolation of the S_4 and its further development into the O–O bond formation is still inaccessible.

Different mechanistic pathways have been developed based on DFT calculations and experimental evidences obtained in the S_0-S_3 states. In Figure 1.6, mechanisms 1 and 2 are somewhat similar to the I2M pathways but involving an oxo-oxyl radical coupling,[41-43] and mechanism 3 is the WNA of water coordinated to Ca to the Mn_4 oxo species.[44] Even though, WNA pathway was supported, for example, by DFT calculation and XAS interpretation by Batista and Brudvig,[45, 46] more recent DFT calculations conducted by Siegbahn suggest that this pathway has very high energy barriers compared to the oxo-oxyl radical coupling. One of the main reasons lies in the lower energy of the formed Mn-O-O-Mn product with respect to the protonated peroxo (OOH or OOH_2) deriving from a WNA pathway.[47] Moreover, another feature supporting the coupling mechanism is that alternating spin alignment in $Mn(IV)\alpha$-O_β-O_α-$Mn_\beta(IV)$ (α = spin up and β = spin down) is necessary for the oxygen bond formation.[48] More recently, the coupling of two oxo ligands coordinated to the same Mn(VII) ion was proposed by Sun (4 in Figure 1.6).[49]

Although many theoretical studies were conducted, doubts on the actual mechanism remain because of the absence of firm experimental evidences. Nevertheless, the research on this topic is still vivid, and progress made in the last years gives hope that this riddle will be solved soon.

1.4 Artificial Photosynthesis using rare metals

Mimicking the OEC of PSII has been the research focus for many scientists in the past 30 years. In this section, the state of the art of rare metal molecular biomimetic systems for water oxidation is presented.

1.4.1 From where all started. Ruthenium-based molecular water oxidation catalysts

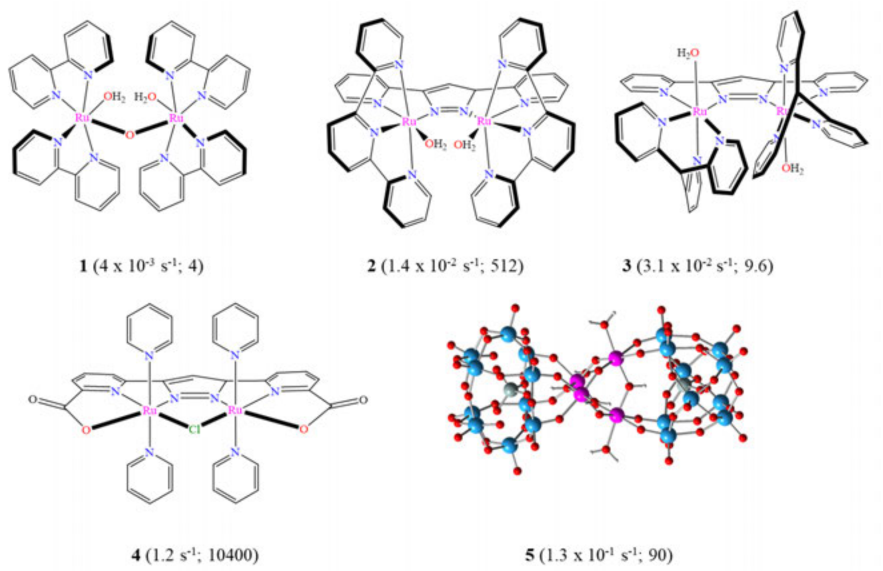

1 (4 x 10^{-3} s^{-1}; 4) **2** (1.4 x 10^{-2} s^{-1}; 512) **3** (3.1 x 10^{-2} s^{-1}; 9.6)

4 (1.2 s^{-1}; 10400) **5** (1.3 x 10^{-1} s^{-1}; 90)

Figure 1.8 *– Selected multi-metallic ruthenium water oxidation catalyst. The TOF and TON are given within parenthesis. Values obtained from water oxidation using CAN. Structure* ***5*** *kindly provided by Bonchio´s group.*

The first example of a molecular water oxidation catalyst was reported by Mayer et al. in 1982 with the name of ‘Blue Dimer’.[50] The complex has a dimeric ruthenium structure, $[Ru^{III}(bpy)_2H_2O]_2O^{4+}$, in which a μ-O bridge connects the metal centers. Initially, a TON of 4 was measured when CAN was used as a one-electron sacrificial electron acceptor at pH 1 and a TOF of 4 x 10^{-3} s^{-1}. The low TON is the result of the reductive cleavage of the μ-oxo-bridge, leading to the decomposition of the catalyst, which is inactive in its monomeric form. Further studies were conducted to elucidate the water oxidation mechanism for guiding further synthetic improvement. At pH 1, the complexes undergo four PCET processes on the two water-bound ligands forming $[Ru^{V}(bpy)_2O_2]_2O^{4+}$. The two newly formed Ru^{V}=O groups are in close proximity, which might suggest an intramolecular coupling reaction, I2M, for O–O bond formation. Instead, kinetic and labeling studies have pointed towards a nucleophilic attack pathway, WNA. A solvent water molecule in the proximity of one of the electrophilic oxo atoms forms a peroxo intermediate (step c in Scheme 1.1). Subsequent proton and electron rearrangements assisted by the second Ru^V=O moiety allow closing the catalytic cycle and releasing one oxygen molecule (Scheme 1.1).[51-53]

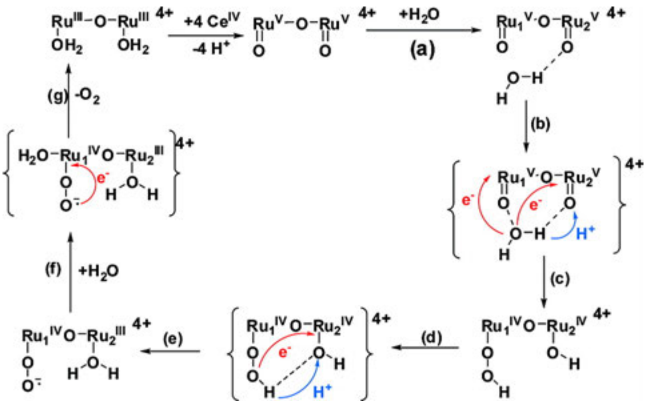

Scheme 1.1 *– Water oxidation mechanism (WNA) of the Blue Dimer, $[Ru^{III}(bpy)_2H_2O]_2O^{4+}$. Bipyridine ligands are omitted for clarity. Transition states are in brackets. Reprinted with permission from ref.[53]. Copyright 2008 American Chemical Society.*

From the well-characterized complex **1**, the μ-O bridge could be substituted with a more rigid and robust organic ligand. For example, using pyrazolate as link, $[Ru^{II}(tpy)_2H_2O]_2(\mu\text{-bpp})^{3+}$ (tpy = 2,2′:6′,2′′-terpyridine, bpp = 3,5-bis(2-pyridyl)pyrazolate, **2**) was obtained. [54] This modification permitted to tune the catalytic proprieties with an increased TOF of 1.4 x 10^{-2} s^{-1}. Interestingly, for this complex, an I2M mechanism was determined by isotopic studies.[55] The two Ru-OH_2 moieties are rigidly oriented towards each other, decreasing the entropic contribution to the activation energy barrier for intramolecular O–O bond formation. The more resistant backbone allowed the complex to reach a TON of 512. A similar modified complex, in which the two water ligands are now facing in the opposite direction is the $[Ru^{II}(tpm)_2H_2O]_2(\mu\text{-bpp})^{3+}$ (**3**, tpm = tris(2-pyridylmethane)). In this case, the mechanism is a bimolecular intermolecular coupling I2M pathway.[56] Despite the similarity in the structure, complexes **1-3** elegantly show how it is possible to obtain different reaction pathways by tuning the ligand coordination sphere.

Inspired by the OEC, Sun et al. differentiate from the N-aromatic ligand-type by introducing carboxylates in the ligand backbone to increase the electron density on the ruthenium metallic center. The synthesized complex **4** has an outstanding stability (TON = 10400) and high activity (1.2 s^{-1}).[57, 58]

A different type of complex was reported almost simultaneously by Bonchio and Hill group.[59, 60] Inspired by the OEC, a tetra-ruthenium complex with μ-O ligand was designed. The catalytic center is embedded in a highly robust polyoxometalate ligand (POM). This all-inorganic complex was designed to be particularly resistant to oxidative conditions. Despite these features, Bonchio reported for the complex (**5** in Figure 1.8) a relatively moderate stability (TON = 90) but a good activity (TOF = $1.3 \times 10^{-1}\ s^{-1}$) in comparison with other multi-metallic ruthenium complexes.

1.4.2 The birth of mono-metallic complexes as water oxidation catalysts

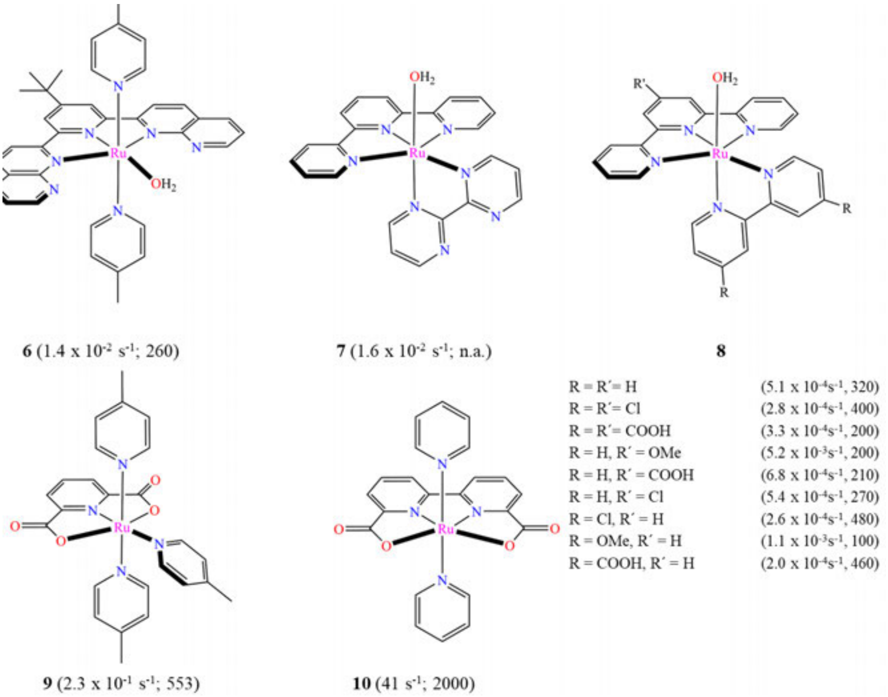

6 (1.4 x 10^{-2} s^{-1}; 260)

7 (1.6 x 10^{-2} s^{-1}; n.a.)

8

R = R′= H	(5.1 x $10^{-4}s^{-1}$, 320)
R = R′= Cl	(2.8 x $10^{-4}s^{-1}$, 400)
R = R′= COOH	(3.3 x $10^{-4}s^{-1}$, 200)
R = H, R′ = OMe	(5.2 x $10^{-3}s^{-1}$, 200)
R = H, R′ = COOH	(6.8 x $10^{-4}s^{-1}$, 210)
R = H, R′ = Cl	(5.4 x $10^{-4}s^{-1}$, 270)
R = Cl, R′ = H	(2.6 x $10^{-4}s^{-1}$, 480)
R = OMe, R′ = H	(1.1 x $10^{-3}s^{-1}$, 100)
R = COOH, R′ = H	(2.0 x $10^{-4}s^{-1}$, 460)

9 (2.3 x 10^{-1} s^{-1}; 553)

10 (41 s^{-1}; 2000)

Figure 1.9 *– Selected monomeric ruthenium water oxidation catalyst. The TOF and TON are given within parenthesis. Values obtained from water oxidation using CAN.*

Despite the need for a multi-metallic catalyst to efficiently distribute the four oxidation equivalents required for water oxidation, from 2005 onward, the scientific interest moved towards mono-metallic complexes. One of the major problems for the stability of dimeric complexes is the degradation of the bridging backbone and the loss of the contribution of a second metallic site, which might be essential for catalysis. Moreover, their fabrication required a significant and time-consuming synthetic effort.[61] To keep up in the emergent field of water oxidation, the study on monometallic complexes allowed a faster screening of different ligand moieties for more rapid performance optimization.

The first monomeric ruthenium WOC was reported by Thummel's group (**6**, Figure 1.9). The performance of the first mono-ruthenium complex was undoubtedly lower compared to the above-mentioned di-ruthenium complexes: for **6**, the TOF was 1.4 x 10^{-2} s^{-1} with a TON of 260.[62] Nevertheless, this inspired the work on further N-aromatic based ligands and new mechanistic insights. Despite the absence of a second metallic center, which may act as a redox mediator, the mechanistic study on complex **7** ($[Ru^{II}(tpy)(bpm)OH_2]$, bpm = 2,2′-bipyrimidine) showed that Ru^{II}-OH_2 undergoes two PCET processes and an additional oxidation to form an electrophilic Ru^{V}=O intermediate. The following WNA pathway is straightforward: upon solvent water addition, the Ru^{III}-OOH intermediate is formed. This undergoes another oxidative process before releasing a molecule of oxygen (Scheme 1.2).[63]

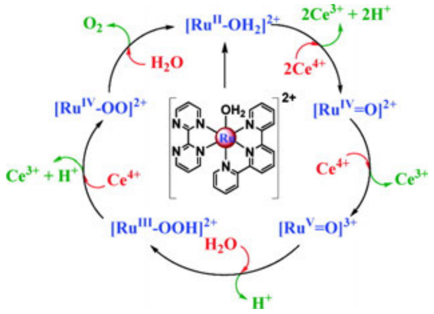

Scheme 1.2 *– Water oxidation mechanism for monomeric* ***6****. Reprinted with permission from ref.*[63]*. Copyright 2010 American Chemical Society.*

An extensive work was conducted to functionalize the aromatic ligands of **8** to tune the electron density on the metallic site. Modification on the tpy and bpy moieties, conducted by the Yagi and Berlinguette groups, respectively, highlighted the need for a balance between reactivity and stability of these complexes as shown by the TON and TOF reported in Figure 1.9.[64, 65]

Simultaneously, Sun's group applied the anionic carboxylate ligands concept to a single metallic center obtaining complex **9** with an outstanding activity (TOF = 0.23 s^{-1}) and catalytic stability (TON = 533).[66] The breakthrough in Sun's group came with the synthesis of complex **10** having the unprecedented TOF of 41 s^{-1} and a TON of 2000. Moreover, it was one of the few reported mono-metallic complexes with intermolecular I2M pathway for water oxidation. This result was supported by isolating the Ru^{IV} peroxo dimeric intermediate, which was resolved by single-crystal X-ray diffraction (XRD).[67]

These finds were also supported by the joined work of Sun and Llobet with an intense study on the catalytic mechanism. Important features are the heptacoordination of the complex with a hydroxo derivate upon oxidation and the identification of the dimer formation as the rate-limiting step of the water reaction catalysis.[68]

1.4.3 Iridium based complexes

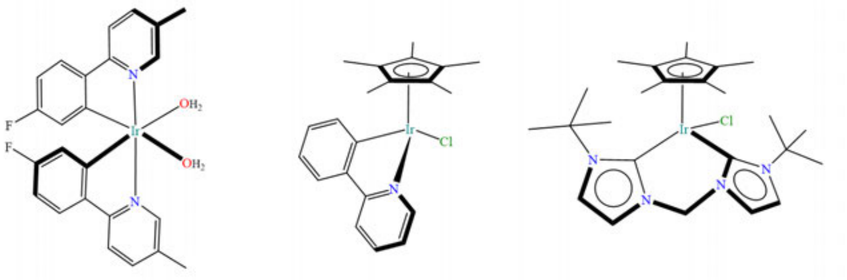

11 (4.1 x 10^{-3} s^{-1}; 2760) **12** (1.7 x 10^{-1} s^{-1}; 1500) **13** (2.0 x 10^{-1} s^{-1}; 1582)

Figure 1.10 *– Selected monomeric iridium-based WOCs. The TOF and TON are given within parenthesis. Values obtained from water oxidation using CAN*

Simultaneously to the prolific study on the ruthenium-based catalysts for water oxidation, also iridium was investigated as a metallic center for the same application. The first series of iridium complexes, with the general formula $[Ir^{III}(ppy)_2(H_2O)_2]^+$, were reported in 2008 by Bernhard's group.[69] It is worth noticing that this was the first example of an organometallic complex adopted for water oxidation catalysis. Among the functionalizations tested in this study, the most successful was the fluoride and methyl substitutions in the same ppy ligand (**11**, Figure 1.10). The resulting electronic push-pull effect seems to be the winning strategy to reach the highest TOF (0.0041 s^{-1}) and TON (2760) among the series. This might be related to the higher oxidation potential, which is required for water-splitting.

Subsequently, Crabtree and Brudvig substituted one of the two ppy based ligands with a Cp* (cyclopentadienyl), obtaining the complex **12**. This showed an improved reactivity (TOF = 0.17 s^{-1}) but with lower stability (TON = 1500).[70] The research on iridium molecular complexes continued until now without significant improvements. For example, one of the last examples was recently published by Tubaro et al. In this case, a chelating carbene ligand (diNHC) was employed to have a robust electron-donating metal-carbene bond. This synthetic effort led to complex **13**, which has good but not outstanding activity and stability (TOF = 0.20 s^{-1}, TON = 1582).[71]

Recent reinvestigations of the reported iridium-based complexes put severe doubts on the molecular nature of the catalysis. This is due to the instability of the Cp* ligand and the high activity of Ir-oxide for water oxidation. It has thus been suggested that the synthesized iridium complexes act only as precatalysts.[72, 73]

1.5 Artificial Photosynthesis using base metals

The use of rare metals has boosted the development and understanding of molecular water oxidation catalysis. However, ruthenium and iridium-based complexes are far too expensive to be employed in scalable and affordable applications. The last decade's focus has been to transfer what has been learned to the more abundant and sustainable base metal complexes. Unfortunately, first-raw transition metals, employed as coordination sites for WOC, suffer the significant drawback of poor stability and low reactivity. Nevertheless, the research is still vivid and aims to solve these problems to reach the performance (and maybe improve) of the comparatively stable (TON about 100 000) and highly efficient (TOF 50-100 s^{-1}, limited by acceptor side) OEC in photosystem II.
Because of the instability of the vast majority of the complexes at low pH, CAN as a one-electron oxidant agent is barely employed. Instead, other methods such as light-driven oxidation, the use of other chemical oxidants, or CPE are used. This made it difficult to have a consistent comparison of the performance. For this reason, in the following reported examples, the TOF and TON are no longer reported in the figures but instead given in the text in some cases.

1.5.1 Manganese

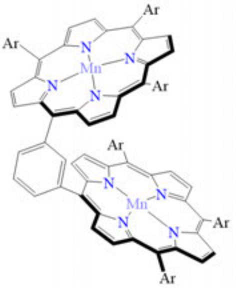

14a Ar = 4-tBuC_6H_4

14b Ar = 2,4,6-$Me_3C_6H_2$

14c Ar = C_6F_5

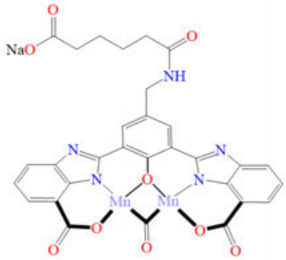

15

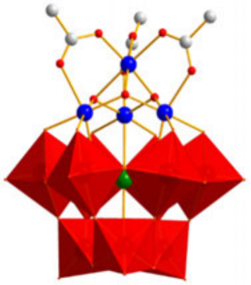

16

Figure 1.11 – Selected manganese catalyst for water oxidation. Structure ***16*** *kindly provided by Bonchio´s group.*

The first notable example of manganese-based molecular complexes for water oxidation catalysis was reported by Naruata et al. in 1994. In particular, a series of complexes (**14** in Figure 1.11) with the common structure of a dimeric face-to-face porphyrin complex and aryl-substituted groups were obtained. CPE in a 5% H_2O-MeCN mixture achieved a Faradaic efficiency (defined as moles of detected O_2 oxygen over the moles of electrons passed in solution) of about 5–17% in a 1.2–2.0 V vs. Ag/AgCl potential range. As expected, electron-donating functionalization (i.e. tris-methyl-aryl substituents) starts to evolve O_2 at the lower potential compared to the hexafluoro-aryl functionalization.[74]

Later on, Crabtree and Brudvig, probably inspired by the ruthenium-based complex **2**, decided to explore the manganese chemistry with a trpy ligand-based dimeric complex.[75] Further studies support a WNA pathway for the water oxidation reaction with the formation of a $Mn^{V}{=}O$ intermediate as a rate-limiting step.[76] In 2014, Åkermark et al. reported a library of dinuclear manganese complexes. The most active resulted in the one with a distal carboxyl group functionalized on the ligand (**15**). This feature was attributed to being essential for assisting the PCET processes on the high-valent manganese species. In this case, the chemical oxidation with $[Ru^{III}(bpy)_3]^{3+}$ at pH 7.2 resulted in a TON = 12 and a TOF = 0.05 s^{-1}.[77]

In the same year, Bonchio's group made use of its POM ligand moiety to obtain a tetra manganese-substituted tungstosilicate decorated with acetate ligands (**16**), claiming an unprecedented mimic version of the OEC. Despite an intense study of accessible S-like intermediate states by flash photolysis techniques, the complex performed 5.2 TON with a TOF = 0.0007 s^{-1} at pH 5.2 in a light-driven experiment.[78]

1.5.2 Iron

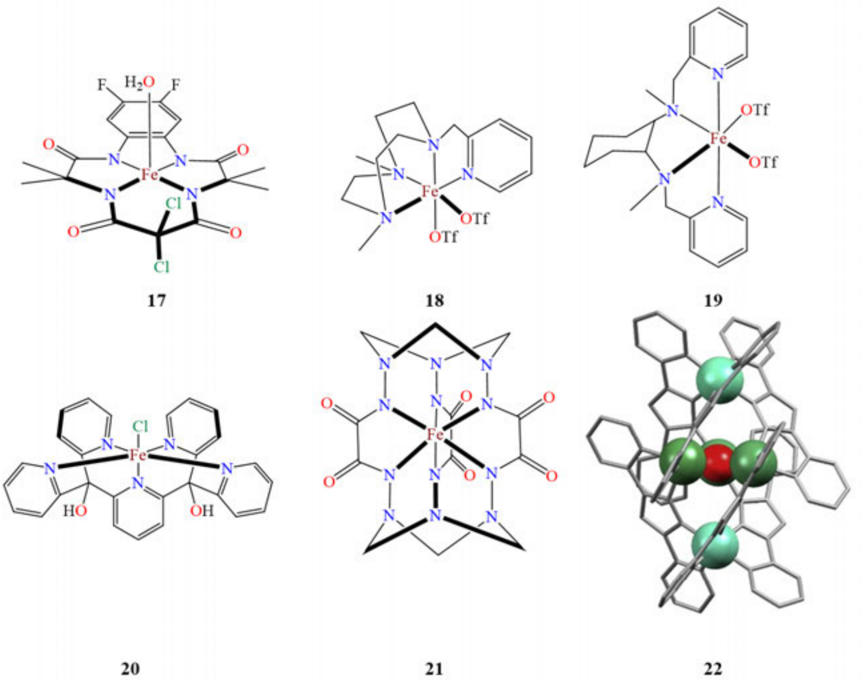

***Figure 1.12** – Selected Iron catalysts for water oxidation. Structure **22**: dark green, Fe(III); light green, Fe(II); red, O. Structure **22** reprinted with the permission of ref.*[79].

Iron is the most abundant element among the first-raw transition metals. Moreover, being in group 8 of the periodic table gives it some similarity to the well-understood ruthenium-based complexes. The first reported study of iron-based complexes for water oxidation was done in 2010 by the Collins group. Their work resulted in a series of iron complexes having a tetra-amido macrocycles ligand (TAML). An interesting feature is the stability at low pH, making it possible to use CAN as the primary oxidant.[80] In these conditions, the best performing version (**17**, Figure 1.12) has a TOF of 1.3 s^{-1} but a TON of only 16. The linear relation between the oxygen production rate and the catalyst concentration suggests a WNA pathway. A further DFT study confirmed this mechanism via Fe^{V}=O intermediate formation.[81]

Thereafter, Fillol and Costas group reported a library of iron complexes with CAN-driven water oxidation reaching the remarkable TON of 360 and 382 for complex **18** and **19**, respectively. DLS (Dynamic Light scattering) experiments were conducted on the post-catalytic solution to exclude the possibility of iron oxide nanoparticle formation, which can be active for water oxidation catalysis.[82] This last aspect becomes important when the catalysis is conducted at neutral or basic pH. A careful study made by Fukuzumi et. al investigated the stability of two iron catalysts ([Fe(BQEN)(OTf)$_2$] and [Fe(BQCN)(OTf)$_2$] (BQEN = N,N'-dimethyl-N,N'-bis(8-quinolyl)-ethane-1,2-diamine, BQCN = N,N'-dimethyl-N,N'-bis(8-quinolyl)-cyclohexanediamine) after catalysis. It turned out that a pH 1.0, the homogenous water oxidation reaction competes with the degradation of the ligand, whereas iron active hydroxide nanoparticles are formed in the photocatalytic experiment at pH 8.0–9.0.[83]

Das et al. reported the catalytic activity of a pentapyridyl (Py5) iron (II) complex under chemical-driven oxidation, **20**. The best performance was obtained with $[Ru^{III}(bpy)_3]^{3+}$ as oxidant at pH 8.0 (TOF = 0.6 s^{-1} ,TON = 43).[84] The activity and the nature of the catalysis for complexes having Py5 moiety is the work of this thesis and it will be discussed in Chapter 6, Paper IV.

More recently, an unprecedented monomeric iron complex with formal charge +4 (**21**) was reported to be also active in a photochemical water oxidation experiment (TOF = 2.27 s^{-1}; TON = 365).[85]

On the multi-metallic family, Okamura et al. reported a pentanuclear iron catalyst, **22** ($[Fe_2^{II}Fe_3^{III}(\mu_3\text{-}O)(\mu\text{-}L)_6]^{5+}$, LH = 3,5-bis(2-pyridyl)pyrazole) with the outstanding TOF of 1900 s^{-1} which was calculated with the foot of the wave analysis of the cyclic voltammetry experiment.[86] Recent studies made by Pelosin and Llobet put serious doubt on the molecular nature of **22** during electrochemical catalysis.[79]

1.5.3 Cobalt

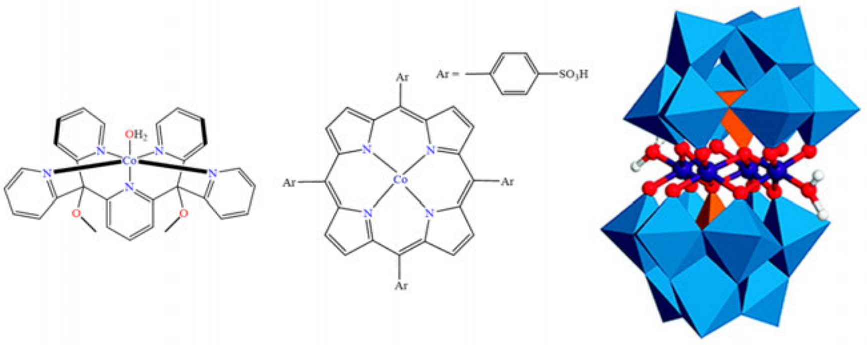

23 **24** **25**

Figure 1.13 *– Selected cobalt complexes for water oxidation catalysis. Structure* ***25*** *reprinted with permission from ref.*[87]*. Copyright 2011 American Chemical Society.*

The first molecular cobalt complex with water oxidation activity was reported by Berliguette in 2010, **23**. Efforts were put to attest the molecular complex as the real catalyst but doubts still remained.[88, 89] A similar structure, but with hydroxyl functional groups substitution was made by Das et al., and the light-driven performance at pH of 8.0 was reported (TOF = 1.3 s^{-1}, TON = 51).[90]

Porphyrin-based cobalt complexes have also been widely explored in this field. The first complete study case was conducted by Ken's group in which the phenylparasulfonic acid substituted cobalt porphyrin, **24**, resulted in the most active performing 122 TON and a TOF of 0.17 s^{-1}. In this case, the mechanism seems to follow a bimolecular I2M pathway.[91] However, other studies on this system raise the possibility of cobalt oxide particle formation.[92]

Hill's group made use of the stable POM scaffold to synthesize a Co_4O_4 cubane complex, **25**, able to operate with a TOF of 5 s^{-1} and reach 75 TON under light-driven condition at pH 8.0.[93] Nevertheless, the work of Finke's group put serious concerns on the stability of this complexes attesting the outstanding oxygen evolution activity to the cobalt ions release in the alkaline solution and subsequent formation of active oxides.[87] Despite these doubts, other Co_4O_4 cubane structures have been explored by Dismukes Patzke and Bonchio. In all of these cases, a tremendous research effort was made to give convincing experimental evidences of the stability of these compounds.[94-96]

1.5.4 Nickel

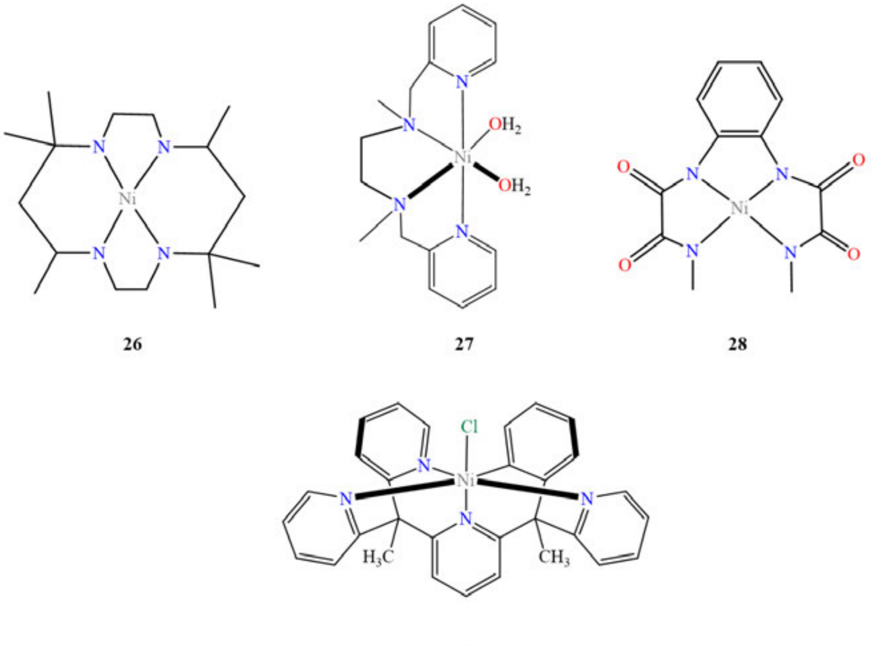

26 27 28

29

Figure 1.14 *– Selected Nickel complexes for molecular water oxidation.*

Despite many reported nickel complexes applied in the hydrogen evolution catalysis, there are only a few studies on molecular Ni-compounds acting as water oxidation catalysts.[97] The first example was reported in 2014 by Lu's group (**26**).[98] The cyclam-like meso nickel complex (Ni(meso-L)](ClO_4)$_2$ L = 5,5,7,12,12,14-hexa-methyl-1,4,8,11-tetraazacyclotetradecane), already widely employed for proton reduction, was found to be active also for water oxidation a neutral pH in a CPE experiment. A key point of the proposed mechanism is the cis-isomerization of the two axial aqua ligands prior to oxygen coupling with an I2M pathway.

Inspired by this, the same group introduced two axial pyridine ligands and left the two cis equatorial sites free for water to bind with the hope of reducing the energy activation barrier. This resulted in complex **27** ([NiL-(H_2O)$_2$]$^{2+}$, L= N,N'-dimethyl-N,N'-bis(pyridin-2-ylm ethyl)-1,2-diaminoethane), which was tested in a CPE in acetate buffer at pH 6.5. However, the evolved current and the Faradaic efficiency were lower than for **26**. The ligand modifications made on the initial compounds affected the oxygen evolution mechanism.

In the case of **27**, the acetate ions, contained in the buffer, were found indispensable for the formation of the O–O bond via an atom proton transfer mechanism.[99]

In 2017, Lin et al. reported that complex **28** is also active for electrochemical water oxidation and does not undergo degradation.[100] However, thereafter, the Llobet group made a comprehensive study on the electrode surface employed during the CPE of **28** and discovered that the complex acted as a pre-catalyst for the fabrication of a very active nickel oxide anode.[101] Another notable example for this thesis work is complex **29**, which employed the methyl-substituted Py5 moiety. Sun's group reported high activity towards water oxidation in a CPE experiment at pH 10.8 with a Faradaic efficiency close to 90%. In this case, an extensive study was conducted to exclude the presence of active heterogeneous metal oxide.[102]

Copper was also adopted in the study of molecular water oxidation catalysis. This metal is out of the scope of this thesis; however, it is worth mentioning the most relevant research using Cu-based complexes conducted by Llobet's group. A family of complexes having a Cu(II) ion embedded in a tetraamidato ligand-type (i.e, $[Cu(mox)]^{2-}$ (mox^{4-} = N^1,$N^{1\prime}$- (1,2-phenylene)bis(N^2-methyloxalamide)) demonstrates how higher oxidation states are easily accessible by the negative charge of the ligand.[103] Water oxidation performances are also enhanced by the stabilization of Cu(III) and higher oxidized intermediates. This is possible only by the singular metal-ligand cooperativity in delocalizing the accumulated charges.[104]

1.6 The flexibility of the Pentapyridyl – Py5 – scaffold

Pentapyridyl ligation (Py5) was extensively employed in the last twenty years as a robust electron donor moiety. Related to this thesis, we have seen its application in water oxidation catalysis in complexes **20**, **23**, and **29**.

So far, three variations of Py5 have been extensively adopted: methoxyl-substituted (**Py5OMe**, pyridine-2,6-diylbis[di-(pyridin-2-yl)methoxymethane]), methyl-substituted (**Py5Me**, 2,6-bis(1,1-bis(2-pyridyl)ethyl)pyridine) and hydroxyl-substituted (**Py5OH**, pyridine-2,6-diylbis[di-(pyridin-2-yl)methanol). Moreover, the Py5 complexes can differ on the sixth apical coordination, which can contain a halide (Cl / Br) or a solvent molecule (Figure 1.15). This is not a trivial aspect because of its impact on the spin properties of the complex, as will be further presented as 'fil rouge' of this thesis.

In 1997, Feringa's group implemented, for the first time, the Py5 ligand to coordinate divalent iron and manganese using the Py5OMe version obtaining $[Fe^{II}(Py5OMe)MeCN]^{2+}$ and $[Mn^{II}(Py5OMe)H_2O]^{2+}$, respectively. The main conclusion was that the σ-donor character of the five pyridines stabilizes the divalent oxidation state, which is also reflected in the LS spin electronic configuration of the MeCN-coordinated iron complex. Moreover, the liable apical coordination site easily accommodates weakly bound ligands and hydroperoxide species in an oxidative environment.[105]

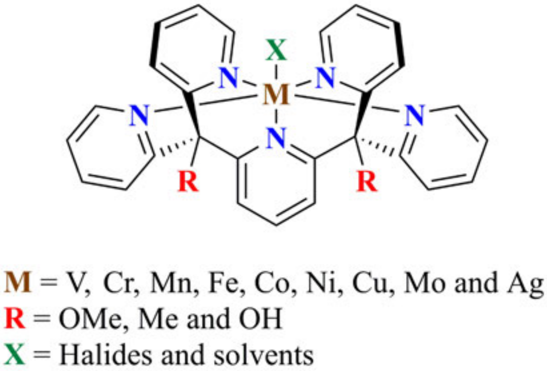

M = V, Cr, Mn, Fe, Co, Ni, Cu, Mo and Ag
R = OMe, Me and OH
X = Halides and solvents

***Figure 1.15** – Metal complexes of the Py5 family.*

This discovery paved the way for its catalytic application. In the same year, Stack's group started an intense study on divalent iron complexes bearing the Py5OMe moiety for biomimetic lipoxygenase reactions.[106-108] The same group made a comprehensive electronic and structural study on the divalent base metal (Mn, Fe, Co, Ni, Cu, and Zn).[109] The main results can be summarised as follows: (i) the different metallic ions radii give the main contribution to the distorted octahedral configuration; (ii) the fifth pyridine in the axial position is tilted due to the steric constraints of the methoxyl substituents; (iii) all the complexes are in HS configurations. The latter statement seems in disagreement with what was reported by Feringa. It is important to notice that, in this case, all the complexes were coordinated with a chloride, which is a weak-field ligand. Magnetic measurements of iron (II) complexes with Py5OMe and different apical ligands highlight how the LS-HS electronic configuration can be easily tuned. For these complexes, only strong-field ligands such MeCN, Pyridine, and CN^- give LS configuration.[110] For intermediate-strength ligands as MeOH and N_3^-, a temperature-dependent spin transition (known as spin-crossover, SCO) was measured in the solid samples.[111] It is worth noting that the SCO phenomenon is an intense field of study. SCO can be triggered by light irradiation, temperature, and pressure changes. This opens doors to manifold applications, in particular on the design of switchable materials (e.g., microthermomiters, chemical sensors, actuators, chiral switches, and thermochromatic materials).[112]

Thereafter, the Py5-family complexes were employed in different applications, such as anti-tumor agents,[113, 114] redox mediators for dye-sensitized solar cells[115, 116], and single-molecule magnet (SMM) design for information storage applications.[117] These studies on Py5-systems highlight the peculiar spin-electronic tunability and flexibility, allowing to accommodate different metals with different oxidation states.

While the state of the art of Py5OMe and Py5Me ligand-type is prosperous, complexes adopting the Py5OH-ligation have never been fully characterized. The insertion of hydroxyl substituents in the Py5 motif was designed for allowing surface immobilization to obtain hybrid anodes for water oxidation applications.[84, 90] However, due to the high tuneability of the Py5-complexes, a comprehensive study on the electronic and structural proprieties of the Py5OH complex is mandatory before being incorporated in a more systematic study on water oxidation activity.

1.7 Aim of the thesis

This thesis aims to contribute to the development of stable and highly active base metal water oxidation catalysts by conducting in-depth structural, spectroscopic, electrochemical, O_2 evolution, and theoretical studies. Through this, the understanding of the intricate interplay between structure, stability, electronic and magnetic properties, as well as reactivity shall be improved so that design principles can be developed. Specifically, the aim was to perform these studies on complexes of the Py5OH ligand family with various first-row transition metals, as here both the metal and the ligand could be varied, and the effects of the apical ligand and its exchange can be studied.

Chapter 2

Materials and Methods

In this chapter, a general introduction and description of the chemical and physical methods that are most relevant to this thesis are presented.

2.1 Synthesis and characterization

2.1.1 Py5OH: the design of a new synthetic route

The reported synthesis of the Py5OH ligand makes use of the organolithium activating agent on bromo-substituted pyridine substrate. Initially, we followed the synthetic route reported by the Stack group of Scheme 2.1.[106] A nucleophilic substitution reaction on the dipicolinic acid is used to obtain the highly reactive acid chloride version in dioxane. After four hours, the solvent was evaporated under a controlled vacuum, and the solid compound was stored in an inert and dry atmosphere. In a second step, a THF solution of 2-bromopyridine is cooled to -78 °C, and *n*-butyl-lithium (*n*-BuLi) is added dropwise to keep the temperature below -60 °C under dry argon atmosphere. Finally, the dipicolinic chloride acid was dissolved in THF and added dropwise to the reaction mixture. After 30 minutes, the reaction was quenched with MeOH, and the solution was brought to R.T.

The work-up was optimized by us and consisted of the addition of 10 mL 10% HCl $^{v}/_{v}$ to ensure the complete protonation of the Py5OH ligand followed by the evaporation of the organic solvent. The aqueous solution was washed three times with DCM to remove unreacted reagents and side-product organic species. The remaining acidic solution was then neutralized by adding sodium carbonate until precipitation of a white product stopped, which is ascribable to the neutral-charged Py5OH by conducting MS analysis (447 $^{m}/_{z}$). Unfortunately, other peaks were assigned as side products of the incomplete lithium-pyridyl nucleophilic attack resulting in a range of 2–4 pyridines assembling. The solid product was then re-dissolved in DCM, and the organic phase was washed with water and separated using a separation funnel. Traces of water were further removed with sodium sulfate, which was subsequently removed by filtration.

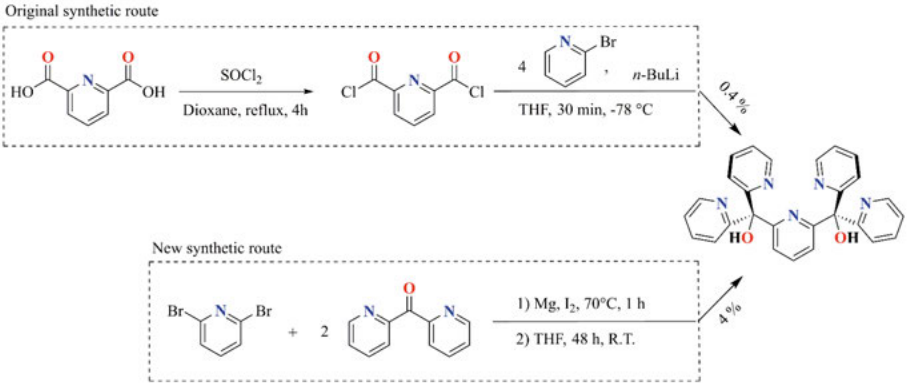
Original synthetic route
HO
OH
O
N
SOCl$_2$
Dioxane, reflux, 4h
Cl
4
Br
n-BuLi
THF, 30 min, -78 °C
0.4 %
HO
OH
New synthetic route
Br
+ 2
1) Mg, I$_2$, 70°C, 1 h
2) THF, 48 h, R.T.
4 %

__Scheme 2.1__ – The synthetic procedure of Py5OH as reported by Stack's group, top; designed by us, bottom.

The dry product was finally obtained by evaporation of the organic solvent. MS and ^{1}H-NMR showed the presence of impurities in the product. Three recrystallization steps by slow evaporation of an acetone solution were required to obtain the desired purity, which was confirmed by high-resolution mass, ^{13}C-NMR (Figure 2.1), ^{1}H-NMR, and solid FT-IR. The maximum yield was 0.4%.

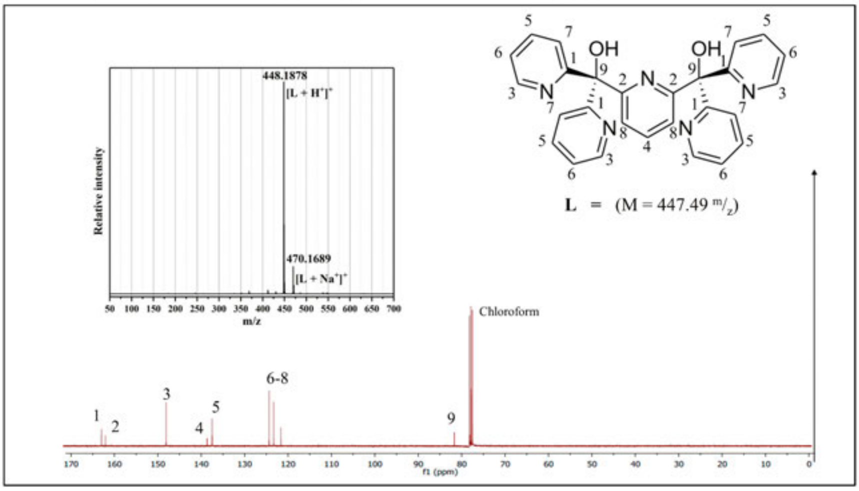

__Figure 2.1__ – ^{13}C-NMR and HR-MS spectra, as inset, of the Py5OH ligand.

We explored a new synthetic strategy to minimize possible side reactions in the organo-metallic step and conduct a more environmental and sustainable synthesis. We, therefore, designed the Grignard reaction presented in Scheme 2.1 using commercially available reagents.

An excess amount of magnesium is activated using a small amount of I_2 under gentle stirring and vacuum conditions for 30 minutes. This step is essential to remove the passive coating on the metal surface. After that, 20 mL of THF was added in argon atmosphere. A dry THF solution of Di-bromopyrdine was added dropwise to the magnesium and stirred at 70 °C until the solution turned brown. The preparation of the Grignard reagent was kept under reflux, and the sampling of the reaction mixture followed by quenching with water and TLC analysis ensured the formation of the organometallic species, in both the 2 and 6 positions of pyridine, after one hour of reaction. Therefore, the formed Grignard reagent was transferred with a canula to a THF solution containing two equivalent of dipyridyl ketone. The reaction mixture was then kept under constant stirring for two days. We used the above-described work-up procedure, but only two recrystallization steps were needed to obtain the desired purity as confirmed by MS analysis. With this new synthesis, the yield was 4%.

2.1.2 Py5OMe

The methoxyl substituted version, Py5OMe, was synthesized following Stack's procedure (Scheme 2.2).[106] The previously synthesized Py5OH compound was dissolved in THF, and five equivalents of sodium hydride (NaH) were added, which led to hydrogen evolution and formation of the alkoxide $Py5O^-$. Five equivalents of methyl iodide were then added, and the reaction was stirred at 40 °C overnight. Thereafter, the reaction was quenched with a 5% $^{v}/_{v}$ HCl solution. Sodium carbonate was then added to adjust the pH to 9.0 to precipitate the product, which was washed several times with chloroform. Traces of water were removed from the chloroform extract with sodium sulfate. The solution was then filtered, and the organic solvent was evaporated under reduced pressure to isolate the product. A single recrystallization step employing acetone/diethyl ether was sufficient to achieve the desired purity with an overall yield of 40%. This was confirmed by ^{1}H-NMR, ^{1}C-NMR, and solid FT-IR.

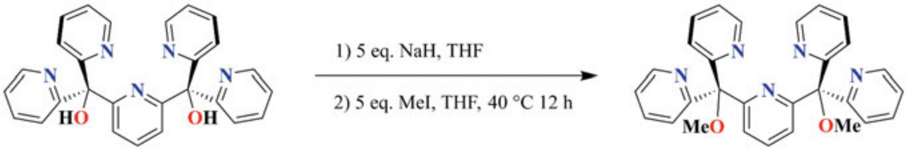

Scheme 2.2 *– Synthetic procedure of Py5OMe*

2.1.3 Synthesis of the chloride ligated complexes $[M^{II}(Py5OH)Cl]PF_6$ and $[M^{II}(Py5OMe)Cl]PF_6$

The chloride ligated complexes, having the general formula $[M^{II}(Py5OH)Cl]PF_6$ where M = Mn, Fe, Co and Ni, and $[M^{II}(Py5OMe)Cl]PF_6$ where M = Mn and Fe, were synthesized starting from their chloride metal salt precursor (MCl_2) using dry and deoxygenated solvents (see Scheme 2.3). The general synthesis was conducted under argon atmosphere as described in the following. The Py5 ligand (either Py5OH or Py5OMe) was dissolved in MeOH. One equivalent of the desired metal salt dissolved in MeOH was added dropwise to the ligand solution that was stirred at R.T. After 30 minutes, KPF_6 (potassium hexafluorophosphate) was added in slight excess to the reaction mixture, which was kept under stirring for 24 hours at R.T. Subsequently, a few drops of diethyl ether were added to promote the precipitation of the product, which was then collected with Buchner filtration. Ice-cold MeOH was used to wash the product from the excess salts. In the case of the iron complexes ($[Fe^{II}(Py5OH)Cl]PF_6$ and $[Fe^{II}(Py5OMe)Cl]PF_6$), it was possible to obtain quantitative recrystallization by slow pervaporation of ethyl acetate in the MeCN complex solution. The purity of the complex was checked by elemental analysis (Table 2.1), HR-MS and solid FT-IR. The average reaction yield for these reactions was 50%.

2.1.4 Synthesis of $[Fe^{II}(Py5OH)Solv](ClO_4)_2$

The chloride-free iron complex $[Fe^{II}(Py5OH)Solv](ClO_4)_2$, where Solv is a solvent molecule that acts as an exogenous ligand, was obtained by metalation from the metal precursor, $Fe(ClO_4)_2$, and the Py5OH ligand in the stoichiometric ratio 1:1 in dry MeOH solution (see Scheme 2.3). The work-up was done in the same fashion as described for the chloride ligated complexes. Recrystallization was carried out by slow pervaporation of ethyl acetate into a concentrated MeOH solution of the complex. The purity of the obtained $[Fe^{II}(Py5OH)MeOH](ClO_4)_2$ was checked by elemental analysis (Table 2.1), HR-MS and solid FT-IR.

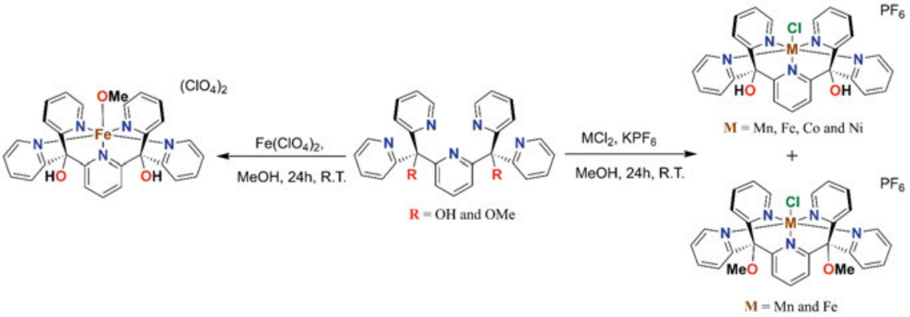

Scheme 2.3 Synthetic procedure for the metal complexes studied in this work

Elemental analysis, which quantifies elements such as carbon, nitrogen, and hydrogen by combustion of the species of interest, is maybe one of the most accurate and straightforward methods to determine the purity of a compound. This is particularly important for catalysts whenever quantitative proprieties (i.e. TON) are measured. Since the element contents are determined relative to the weight of the analyte, care must be taken to clean the compounds from residual unreacted reagents and by following a rigorous drying procedure. Furthermore, the elemental analysis of a crystalline sample might be affected by the solvent molecules included in the crystal lattice.

Table 2.1 *- CHN elemental analysis of the synthesized complexes.*

Samples	**C**		**H**		**N**	
	Theory	**Exp.**	**Theory**	**Exp.**	**Theory**	**Exp.**
$[Mn^{II}(Py5OH)Cl]PF_6$	47.49	47.78	3.10	3.28	10.26	10.08
$[Fe^{II}(Py5OH)Cl]PF_6$	47.42	47.61	3.10	3.26	10.24	10.09
$[Co^{II}(Py5OH)Cl]PF_6$	47.22	48.06	3.08	4.29	10.20	9.15
$[Ni^{II}(Py5OH)Cl]PF_6$	47.23	48.22	3.08	4.26	10.20	9.03
$[Fe^{II}(Py5OH)MeOH](ClO_4)_2$	45.80	46.30	3.43	4.30	9.54	10.98
$[Fe^{II}(Py5OMe)Cl]PF_6$	48.93	48.83	3.54	3.75	9.84	10.17
$[Mn^{II}(Py5OMe)Cl]PF_6$	49.00	47.51	3.54	4.41	9.85	9.48

Table 2.1 shows the results of the elemental analysis for the synthesized complexes of this thesis. The percentage difference from the theoretical element content is in line with what is recommended according to the method's precision (~ 1%).

2.1.5 Synthesis of $[Ru^{II}(bpy)_3](ClO_4)_2$ and $[Ru^{III}(bpy)_3](ClO_4)_3$

The chloride counter ion of the commercial photosensitizer $[Ru^{II}(bpy)_3]Cl_2$ was substituted with perchlorate (ClO_4^-) using the following procedure. A 5 M sodium perchlorate ($NaClO_4$) water solution cooled to 0 °C was added dropwise to a concentrated (0.05 M) and ice-cold solution of $[Ru^{II}(bpy)_3]Cl_2$, which induced the precipitation of the perchlorate metal complex. When no more solid was formed, the complex was collected by filtration and carefully washed with ice-cold water to remove salt excess. To ensure high purity, the product was recrystallized in hot ethanol. During this process, the vessel was covered with aluminum foil to avoid light degradation. Crystals were then collected and dried under vacuum. The MS analysis conducted at low ionization energy shows the fragment $[Ru(bpy)_3(ClO_4)]^+$ (669.0 m/z). The purity of the complex was determined to be 98% by measuring the UV-Vis absorbance of the characteristic peak at 454 nm (ε = 1.46 x 10^4 $mol^{-1}cm^{-1}$) [118] of a 50 µM solution of the complex in water.

The oxidized $[Ru^{III}(bpy)_3]^{3+}$, used for chemical-driven oxidation assays, was prepared from the commercial $[Ru^{II}(bpy)_3]Cl_2$ complex. The synthesis is an improved version of the reported procedure.[119] Lead(IV) oxide (PbO_2) was added in significant excess into a concentrated solution of $[Ru^{II}(bpy)_3]Cl_2$ (0.05 M) in 3.5 M sulfuric acid. The choice of this solvent ensures the stability of the newly formed ruthenium (III). The reaction mixture turned from orange to dark green, and it was kept under vigorous stirring for 10 minutes. Subsequently, the lead oxide was removed by filtration, and the solution was cooled in an ice bath. To promote the counter ion-exchange, cold 5 M $NaClO_4$ was added dropwise until a precipitate formed. The solid was collected by filtration and washed with ice-cold water. Due to the instability of the complex, no further purification was possible. The purity of the product was determined to be 97% by measuring the UV-Vis absorbance at 675 nm (ε = 420 $mol^{-1}cm^{-1}$) of a 2.0 mM solution in sulfuric acid (3.5 M).[120]

2.2 X-ray techniques

X-ray electromagnetic radiation can be tuned to the energies required for exciting core electrons of atoms. This energy depends, among other factors, on the atomic number. This makes X-ray spectroscopic techniques element-specific.

2.2.1 XAS

When an X-ray photon interacts with a core electron, this can be promoted to an empty higher orbital state or be ejected into the continuum. In an X-ray absorption spectroscopy (XAS) experiment, the photon´s energy is scanned with the use of a monochromator, and because of the quantization of the electronic energy´s state of the absorber, a sudden rise of the absorption is detected (edge transition). The XAS´s nomenclature names the transition according to the initial state of the absorbing electron: with a letter the principal quantum number (n) and with a number the orbital angular momentum (l) (e.g., K-edge = 1s, L_2-edge = 2p, etc.). The dipole selection rules impose that only $\Delta l = \pm 1$ transitions are allowed. However, the forbidden transition can occur because of orbital mixing or higher-order transitions (i.e., quadrupole transition) and can be observed at smaller intensity before the edge transition. For example, the transition $1s \rightarrow 3d$ is a common pre-edge transition. At energies above the edge transition, the electron is ejected into the continuum, where it interacts with atoms in the absorber´s surroundings. This can lead to backscattering of the electron wave, which modulates the absorption spectra. An XAS spectrum can be divided into two regions, as shown in Figure 2.2.

XANES (X-ray Absorption Near Edge Spectroscopy) usually is recorded at ± 30 eV from the edge. The chemical information that can be derived includes (i) oxidation state of the absorber from the edge position; (ii) spin state of the absorber due to the shape of the edge transition and (iii) ligand geometry from the pre-edge transition. Simulation of XANES is challenging because it requires a multi-body analysis. Therefore, commonly reference compounds are used to interpret the spectra.

The EXAFS (Extended X-ray Absorption Fine Structure) region is recorded from + 50 eV up to 1000 eV from the edge. Because of the absorption coefficient modulation due to the backscattering phenomena with neighboring atoms, information on (i) metal-to-ligand distances and (ii) approximate identity and the number of atom(s) at a specific distance (shell) can be obtained. The EXAFS spectrum is simulated to estimate the chemical environment of the absorbing atom type. An average of all atoms of the same element is obtained.

The ejected electron leaves behind a core hole, which in turn can be filled by another electron from a higher orbital state, and that can be accompanied by the emission of X-ray fluorescence (i.e., Kα fluorescence from 2*p* electrons filling a 1*s* core hole).

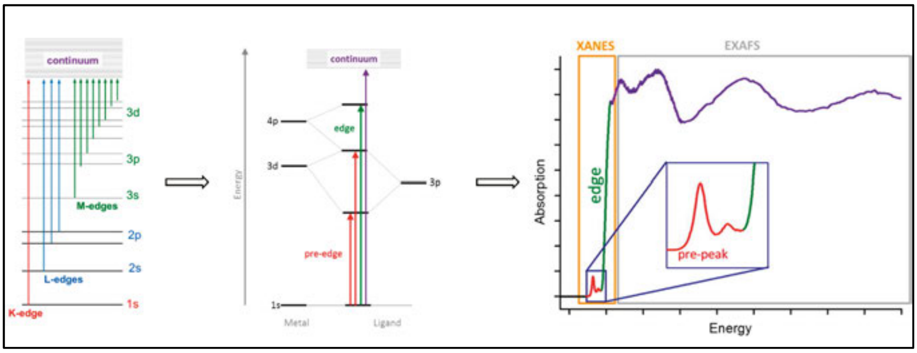

Figure 2.2 – *Graphical description of the XAS transitions. Left: edge-transition nomenclature. Center: forbidden transition, red; allowed transition, green; excitation into the continuum, purple. Right: the corresponding regions of a XAS spectrum. Reprinted with permission from ref.*[121]*. Copyright 2015 Elsevier B.V.*

The XAS experiments presented in this thesis were conducted in synchrotron facilities that provided high X-ray fluxes. The experiments were conducted in a cryostat at 20 K and 125 K, and the majority of the samples were frozen at 0.5–1.0 mM concentration. To enhance the sensitivity of the measurements, the recording was carried out in the fluorescence mode as shown in Figure 2.3, recording the Kα fluorescence from the metal using an energy-resolving silicon drift detector. This gives the exact information of the absorption because the fluorescence intensity is directly proportional to the absorption coefficient for dilute samples.

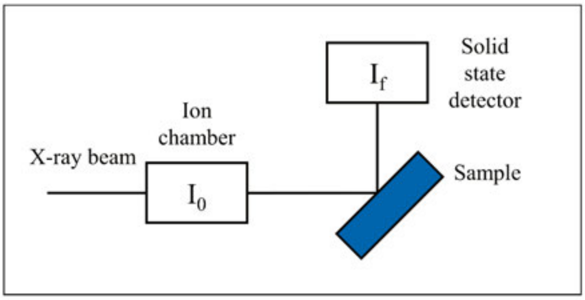

Figure 2.3 *– Fluorescence detection mode employed to measure XAS spectra in this thesis.*

2.2.2 XPS

XPS (X-ray Photoelectron Spectroscopy) is based on the photoelectric effect, which permits the identification of the surface-deposited elements and their chemical proprieties (i.e., oxidation and spin state). In an XPS experiment, monochromatic X-ray radiation (i.e., 1486.7 eV for Al Kα emission) is focused on a 10–200 µm sample area. The photoelectric effect results in the emission of core electrons, and the difference between the X-ray photon energy and the electron's kinetic energy results in the element-specific binding energy. Because XPS requires a high vacuum (i.e., 10^{-7} bar), samples must be stable in dry condition. (i.e., sublimating samples cannot be measured).

2.2.3 XRD

XRD (X-ray diffraction) techniques use X-ray photons' elastic scattering phenomena when a beam is focused on a well-packed atomic crystal structure. By measuring the angle between the incident and scattered beam (θ), Bragg´s law (Eq. 2.1) allows determining the distance between two atoms (d).

$$n\lambda = 2d\ sin\theta \qquad \text{Eq. 2.1}$$

In a typical experiment, the crystal is mounted to a rotating arm, and a diffraction pattern is measured at selected angles. Post analysis of the collected diffraction patterns allows the crystallographer to identify the atomic structure of the interesting species. Nowadays, the accuracy of many 'in-house' XRD machines is at the order of the second decimal of Å. The resolution of the resolved molecular structure also depends on the quality of the crystal, which should be free of defects and must have a uniform crystal packing. It is worth mentioning that the lattice structure provides a different chemical environment from where the chemistry is performed. High density-packing and the temperature at which XRD is measured (usually around 150 K) can have an impact on the spin state and atomic distances of the dissolved molecule.

2.3 Magnetic methods

2.3.1 EPR

The first reported EPR (Electron Paramagnetic resonance) spectrum on a manganese sulfate solution was recorded in 1944 by the Russian physician Y. K. Zavoisky.[122] EPR is the primary choice for studying paramagnetic species such as radical species and metal complexes. When an external homogenous magnetic field (B_0) is applied on a paramagnetic sample, the electronic magnetic moment of the unpaired electron with spin $S = 1/2$ splits into two states ($S_\alpha = 1/2$ and $S_\beta = - 1/2$) which align along B_0. This phenomenon is called the Zeeman effect, and the field-dependent energy difference between the two states is defined by Eq. 2.2 where g is the g-factor and μ_B is the Bohr-magneton.

$$\Delta E = g\,\mu_B\,B_0 \qquad \text{Eq.2.2}$$

In a typical EPR experiment, a micro wavelength probes, by an absorbing process, the Zeeman-splitting energetic states of the paramagnetic compound. Differently from other spectroscopies, the probing electromagnetic radiation has fixed energy while the applied magnetic field B_0 is scanned. EPR instruments are classified based on their microwave frequency. In this thesis, two EPR instruments were employed: X-band using a microwave frequency of 9.4 GHz and W-band using a microwave frequency of 94 GHz. Since the spin population difference is small (approximately 10^{-3} of the total spins according to the Boltzmann distribution for $B_0 = 0.33$ T), different strategies are applied to enhance the EPR signal, such as the recording of the derivate of the absorption signal, the use of resonator sample holder (also called cavity) in which the power of the microwave is enhanced, and the measurement under cryogenic temperatures to prevent the fast relaxation of the spin centers, which might result in the broadening of the signal.[123]

The electronic spins couple with the orbital angular momentum of the electron (spin-orbit coupling), and the measured g value differ slightly from the free electron´s value of a $g_e = 2.0023$. This is used as a fingerprint to recognize the chemical environment of the spin center. The spin-orbital coupling contribution is a direction-dependent parameter (anisotropic). Therefore, the EPR spectrum of an oriented crystalline compound might result in distinct g-terms. The EPR of a frozen solution considers the sum of all the statistical possible spin orientations, and depending on the molecular symmetry (isotropic, axial, or rhombic), the different *g* anisotropic contributions are recorded (Figure 2.4).

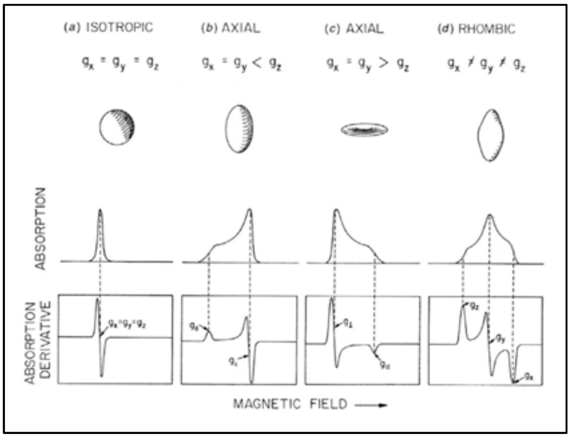

***Figure 2.4** – Schematic representation of g tensor and the consequential EPR spectra. The upper solid bodies show the shapes associated with isotropic (a), axial (b, c) and rhombic (d) magnetic moments. Underneath are shown the absorption curves. The corresponding EPR derivative curves are shown on the bottom. Figure reprinted with permission from ref.* [123].

Further energy splitting of the spin state can occur because of the coupling between the electronic spin and nuclear magnetic moment (*I*). For example, for an Mn nucleus, *I* = 5/2, the sublevel´s number will be characterized by six sub-states ($M_I=2I+1$). This phenomenon is called hyperfine coupling and can be used to recognize the element that gives origin to the EPR signal. It is worth noting that hyperfine coupling is field-independent, and the energy splitting is dictated by only the hyperfine coupling constant '*A*', which is usually two orders of magnitude smaller than the Zeeman interaction for an X-band instrument.

Systems with *n* unpaired electrons have a total spin of $S = n/2$ with a multiplicity defined as $M_S = 2S + 1$. This is very common in metal complexes with $d^{2–8}$ electronic high spin configuration. Electrons undergo exchange interaction (or spin-spin interaction), leading to a split of their ground terms (i.e., for HS, d^5-Mn^{II}: n = 5, S = 5/2, M_S = 6, and the spin term:1/2, 3/2, and 5/2). Unlike the Zeeman effect, this interaction is present even in the absence of $B_{0,}$ and it is therefore called zero-field splitting (ZFS). In experiments conducted with X-band EPR, the ZFS can be stronger than the Zeeman splitting in such cases, transitions occur within each pair. The pairs are called Kramer doublets, and for HS Mn^{II} they are: ±1/2, ± 3/2, and ± 5/2, as shown in Figure 2.5. The ZFS is represented by the axial and rhombic parameters of Eq. 2.3a-b.

$$D = \frac{3D_x}{2} \quad \text{Eq. 2.3a}$$

$$E = \frac{D_x - D_y}{2} \quad \text{Eq. 2.3b}$$

The ratio *E/D* defines the rhombicity of the system (i.e., *E/D = 1/3* for the most rhombic systems). Not all spin multiplicity terms are equally populated. Therefore, spectra have to be recorded at different temperatures to characterize the system entirely. To identify better all the single interactions, a sample should be recorded in different fields. Ultimately, simulations of the recorded EPR spectra are crucial to extrapolate all the above-discussed parameters.

The study of the ZFS splitting parameter is fundamental to understand the local geometry of the paramagnetic metallic center. Among other applications, the ZFS can be tailored to design single-molecule magnets (SMM) in which the strategy is to block the magnetization of a low-dimension magnet by enhancing the rhombicity (i.e., with large *D* and small *E*, to avoid coupling among the spin ground terms).[124] This concept will be used in Chapter 5 (Paper III).

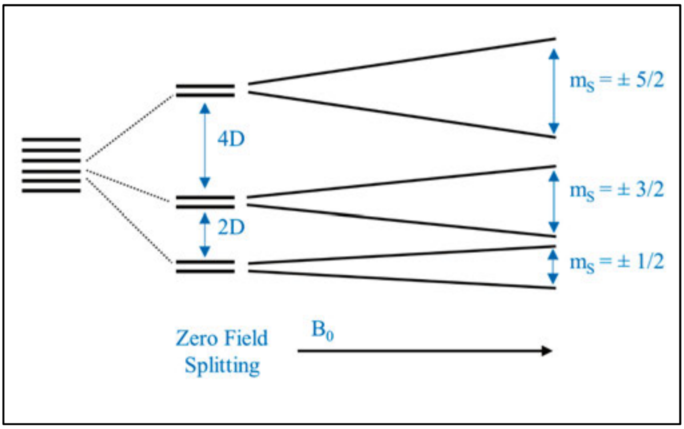

***Figure 2.5** – Zero-field splitting effects in S = 5/2 systems with a zero field splitting parameter (D) that is large compared to the microwave frequency.*

Understanding how to control the ZFS *D* parameter is important in developing SMMs for ‘high density’ information storing devices. A competitive magnetic tunneling effect tends to restore the antiferromagnetic state at room temperature, which is thermodynamically more favorable. This causes the loss of the mutual spin orientation and the degradation of the stored information. Therefore, being able to select a system with high anisotropy is essential to set a high energetic barrier.[125]

2.3.2 SQUID and the Spin crossover

SQUID (Superconductive quantum interference device) is a magnetometer employed in magnetic propriety measurements. SQUID instruments are extremely sensitive in measuring magnetic fields of the order of 10^{-18} T. [126] In this thesis, SQUID has been employed to measure the magnetic susceptibility (χ) of a Fe^{II} metal complex at different temperatures. Magnetic susceptibility measures the magnetization (M, as magnetic moment per unit volume) in an external magnetic field (B_0), and it is expressed as $\chi = M/B_0$. Paramagnetic compounds align along the B_0 direction if $\chi > 0$. Because χ is measured by varying the temperature (from 313 K to a few K), one must include Curie's law which defines the linear relationship between the measured M and temperature. This results in the $\chi_M T$ parameter (molar magnetic susceptibility, $cm^3\ K\ mol^{-1}$) proportional to the spin state multiplicity (i.e., the number of the unpaired electron, n) in a paramagnetic compound. This relation can be described with the 'Spin-Only Formula' in Eq. 2.4, where μ_B is the Bohr Magneton, while the nuclear or orbital magnetic moments are considered to be negligible.

$$\chi_M T \propto \sqrt{n(n+2)}\mu_B \qquad \text{Eq. 2.4}$$

Three different SQUID experiments are shown in Figure 2.6, where χ_M is measured by varying the temperature in a cyclic fashion.

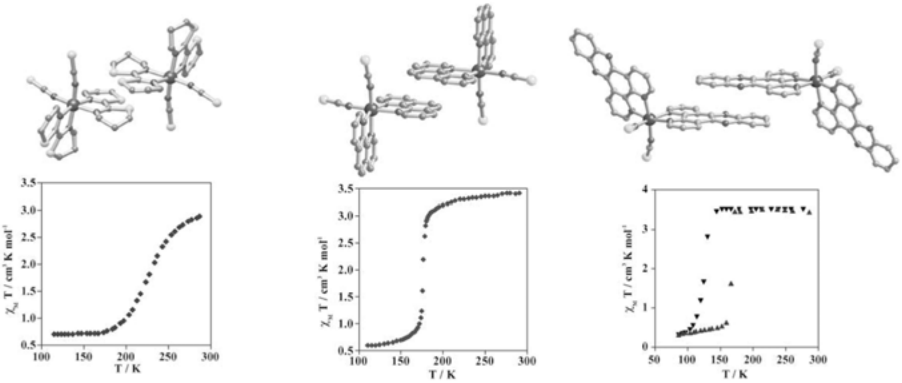

Figure 2.6 – SQUID experiments to determine the spin-crossover properties of three crystalline Fe(II) complexes depending on their intramolecular interaction. On the left continuous transition, in the center abrupt transition, on the right abrupt transition with hysteresis. Reproduced from Ref. [112] with permission from The Royal Society of Chemistry.

These experiments show different types of spin-crossover behavior, i.e., for the spin state change from HS to LS, by lowering the temperature. All three examples are for crystalline Fe^{II} complexes. The spin crossover can be continuous, discontinuous (abrupt change), and discontinuous with hysteresis depending on the intramolecular interaction and cohesive force (e.g., hydrogen bonding, π-π interactions) among the monomeric compounds, which induce cooperative behavior.[112]

2.4 Computational methods

2.4.1 General introduction

Solving chemical problems and obtaining chemical-physical parameters by calculating the exact energy ($\boldsymbol{E}$) of a system has been the unreachable dream of the computational chemistry field. The Schrödinger equation (Eq. 2.5) can be analytically solved only for hydrogen-like atoms. For 'multi-body' systems, the major problem lies in quantifying the electron's energy interactions.

$$\boldsymbol{H}\psi = \boldsymbol{E}\psi \qquad \text{Eq. 2.5}$$

In an *ab initio* calculation, Eq. 2.5 is solved by choosing an approximate model for the electronic wavefunction (ψ) from which the energy can be calculated by applying the Hamiltonian operator ($\boldsymbol{H}$). The latter is composed of mathematical operators describing the potential and kinetic energy of the system.

Almost all commonly employed quantum chemistry methods use the Born-Oppenheimer approximation, which considers the atom nuclei in a fixed position when solving the electronic wavefunction and the respective energy are calculated. This can then be followed by solving the nuclear wavefunction using the potential energy surface generated by the solutions to the electronic wavefunction. For the electronic part, the Hartree-Fock (HF) method was one of the first *ab initio* methods to be developed and forms the basis for much of the later method development. HF theory considers each electron interacting with a mean potential field generated by the other electrons of the system and the nuclei. In this way, the electronic wavefunction can be written as a product of the spin-orbital function for each electron. The true wavefunction must respect the anti-symmetry of the electronic system (Pauli exclusion principle). Therefore, the Slater determinant is used as a final form of the initial guess ψ. The ground state energy (E_0) is estimated with a self-consistent field (SCF) method by iterative minimization of the energy (ε) with a test ψ_{trial} in which coefficients in front of the basis functions are used to describe the shape of each electron spin orbital as variables. These coefficients are therefore adjusted in each iteration until the energy gradient is below a predetermined value.

$$\varepsilon = \frac{\langle \psi_{trial} | H | \psi_{trial} \rangle}{\langle \psi_{trial} \psi_{trial} \rangle} \geq E_0 \qquad \text{Eq .2.6}$$

Through the use of the Slater determinants, the HF method offers a formally correct description of the exchange energy, E_X, (repulsion among electrons with parallel spin). However, it does not consider the electron correlation energy, E_C, which comes from the adaptation of the position of an electron as a response to the instantaneous position of the other electrons. To include E_C, additional Slater determinants are usually added on top of the HF reference. This can be done in several different ways, forming different families of correlated wavefunction methods, such as configuration interaction, coupled-cluster, Møller-Plesset perturbation theory, and multi-configurational methods such as the complete active space approaches. However, the addition of a large number of additional determinants can results in significant computational cost for systems with a large number of electrons.[127]

As an alternative to the correlated wavefunction methods, in the last thirty years different forms of Density-functional theory (DFT) have demonstrated excellent accuracy relative to the computational cost, for geometries and energetics of a wide range of different systems. DFT is based on the one-to-one correspondence of the electron density of the system with its ground state energy (Hohenberg-Kohn theorem). DFT deals with finding the most accurate functional to describe the electron density, $E[\rho]$, by considering the different energetic contribution as: the kinetic energy of the electron (*T*), the potential energy of the electrons due to the attraction with the nuclei (*V*), the potential energy of the repulsion among electrons (*J*), the quantum mechanical exchange energy of the electrons (*X*), the quantum mechanic correlation energy of the electrons (*C*) (Eq. 2.7).[128]

$$E_{DFT}[\rho] = E_T[\rho] + E_V[\rho] + E_J[\rho] + E_X[\rho] + E_C[\rho] \qquad \text{Eq. 2.7}$$

In Kohn-Sham DFT (KS-DFT), Slater determinants are reintroduced to accurately evaluate the kinetic energies and a better estimate of the electronic density. The chosen functional $E_{DFT}[\rho]$ is then applied to calculate the energy, which is then minimized with respect to the basis set coefficients in an SCF procedure. The exchange and correlation parts are the most challenging to develop among the functional components as there is no known formula for approaching the exact solution. The first proposed functional based on KS-DFT was the LDA (local density approximation) in which the energy in any given point is evaluated based on a uniform electron gas, although the value of the electron density is different in different parts of the molecule. A more accurate approximation is the GGA (generalized gradient approximation) in which the energy is additionally a function of the gradient of the electron density.

A further improvement came with the hybrid functionals built with a certain percentage of the 'exact' exchange from HF theory and a GGA exchange energy functional. In this respects, the most famous, in computational molecular chemistry is B3LYP, which includes 20% of HF exchange contribution ($a = 0.2$ in Eq 2.8).[129]

$$E_X^{B3LYP}[\rho] = (1 - \mathrm{a})\, E_X^{LSDA}[\rho] + \mathrm{a}\, E_X^{HF}[\rho] + \mathrm{b}\, E_X^{B88}[\rho] + (1 - \mathrm{c})\, E_X^{LSDA}[\rho] + \mathrm{c}\, E_X^{LYP} \qquad \text{Eq. 2.8}$$

Early GGA functionals tend to overestimate correlation, leading to an overestimation of bond covalent strengths. As HF underestimates correlation and bond strength, this leads to partial error cancellation. The B3LYP functional has shown good accuracy in benchmark tests for transition metal complexes and enzymatic cofactors. The relative error for the M–L bond energy is around 3-5 kcal mol^{-1}, while for other non-hybrid methods (i.e., BLYP and BP86) the error is usually higher than 20 kcal mol^{-1}.[130]

It has been reported that including the exchange HF contribution in Eq. 2.8, stabilizes the HS state of a molecular complex.[131] This is attributed to a stronger exchange interaction since electrons are relatively closer than expected because of the lack of correlation energy. A fine tuning of the amount of HF exchange can also be applied whenever experimental data are accessible, as we did in this thesis (Paper I). Other functional based on semi-empirical methods such meta-GGA or meta-hybrid GGA give more accurate results in benchmark tests. However, as they have not been as widely used as B3LYP and related methods, less is known how well they describe different systems, and it can therefore be preferable to use older functionals with well-known error profiles.

Single-reference methods like HF and most DFT functionals lack an explicit description of dynamical correlations, and therefore a consistent treatment of the mutual instantaneous polarization that describes London dispersion. These are important for calculating the conformation of large molecules, the energy of polymeric systems, or upon ligand binding.[132] A popular alternative to take into account dispersive interactions is the empirical D3 correction (3 stands for the third version) that can be added directly to a DFT functional.[133] Solvent contributions to the total energy of the system is mostly computed using an implicit model. This is typically introduced using the polarizable continuum models (PCM), in which a continuous dielectric field is introduced around the solute cavity. The Solvation Model Based on Density (SMD) is typically more accurate for absolute solvation energies, partly because it is further parameterized against experimental data, and also uses the total solute electron density to compute the cavity-dispersion.[134]

The unknown wavefunctions are described, to a first approximation, as an expansion of know functions knows as basis sets. One of the most commonly used type is the Gaussian Type Orbital (GTO). To reduce the number of optimized variables, orbitals are typically described with a fixed normalized linear combination of primitive GTO (PGTO) giving contracted GTO (CGTO).

Minimum basis sets typically use one CGTO for each atomic orbital, which is typically not flexible enough. To further enhance the orbital descriptor's exactness, the number of basis sets can be doubled or tripled (called double-zeta or double-ζ and DZ or triple-zeta, triple-ζ or TZ). Nevertheless, it was observed that good results could be obtained with less computational effort if only the valence orbitals are described with DZ or TZ. These basis sets are called split-valence basis sets (SV). Polarization functions are also used to consider chemical bonds in which the molecular orbitals have a higher angular momentum character than the single atoms (i.e., distortions due to the presence of near atoms). For example, in the basis sets describing a σ - molecular orbital in the H_2 molecule, *p*-orbitals are included. Finally, diffuse functions are modified GTOs, where the 'tail' of the function extends out from the atomic orbital (the exponent on the GTO is smaller). The diffuse functions are important to describe anions and intramolecular bonding.

For this thesis, two families of basis sets were employed. To achieve the best accuracy with the minimum computational time, the metal center was described by an effective core potential for the core electrons while the valence orbitals are described with a double-ζ or triple-ζ basis set, i.e., the LanL2DZ (Los Alamos National Laboaratory 2 double-ζ) or the LanL2TZ(f) (triple-ζ and *f*-orbital polarization). The atoms of the ligand sphere were computed using the Pople basis sets 6-31G(p,d) at the double-ζ level. The two numbers define a double-ζ description of the wavefunction. In this case, the core orbitals are composed of six PGTOs and the valance shell by three PGTOs and a single PGTO, respectively. The polarization is added by including *p* and *d* orbitals. For triple-ζ quality, a 6-311+G(2df,2pd) (triple-ζ with diffusion and 2*df* and 2*pd* polarization orbitals) basis set was used.

2.4.2 DFT procedure

To calculate the optimized structure and the thermodynamic proprieties of the studied compounds the software Gaussian09 E. 01 was used.[135] The following calculation steps have been followed.

I. An initial geometric optimization was done using the B3LYP functional and a double-ζ basis set.

II. The thermal energy was then determined by calculating the Hessian matrix to find the vibrational energies of the nuclear wavefunction using the harmonic approximation. This gives the total Gibbs free energy expressed by all the single energetic contribution as shown Eq. 2.9.

$$\begin{aligned}\Delta G &= \Delta \mathrm{H} - \mathrm{TS} \\ &= (E_{Ele} + E_{ZPE} + E_{Vib} + E_{Rot} + E_{Trans} + k_b\mathrm{T}) - \mathrm{T} * \mathrm{S}\end{aligned} \qquad \text{Eq.2.9}$$

Where k_b is Boltzmann constant, S is the entropy, T is set at 298.15 K (unless otherwise stated), and the sum in the bracket is the internal energy divided for every single contribution and the enthalpy correction. The former is composed of the electronic energy, E_{Ele}, the Zero-point energy (i.e., the zero temperature vibrational energy), E_{ZPE}; the rotational energy, E_{rot} and the translational energy, E_{trans}. The bigger contribution comes from the electronic energy (or single point energy) which is five orders of magnitude higher than the other energetic contributions. The binding energies in this thesis are corrected with solvent entropic factor $S = k_b \ln W$, where W is the number of solvent molecules per complex.

III. The optimized structural geometry is then re-calculated with the most extensive basis sets: LanL2TZ(f) for the metal and 6-311+G(2df,2pd) for all the other atoms.

IV. Finally, the electronic energy in Eq. 2.8 is corrected with a single point calculation performed with the optimized structure in (III) using B3LYP*-D3. The * identifies that the B3LYP has been modified by varying the HF contribution to 15% as it results in the best descriptor for the spin-state energetics based on experimental data (see Chapter 3, Paper I). The obtained E_{Ele} was then included in Eq. 2.8. Correcting the electronic at this stage does not affect the accuracy of the method since the Hessian is determined at the flat energy minimum and small energy differences are not significantly affecting neither the thermal contribution nor the optimal geometry.

The redox potential for $M^{III/II}$ was calculated using Eq. 2.10

$$\mathrm{E}_{\mathrm{III/II}} = \frac{\Delta G_{\mathrm{III/II}}}{nF} - \mathrm{E}_{\mathrm{Fc^{+}/Fc}} \qquad \text{Eq.2.10}$$

Where n is the number of electrons (one for the III→II reduction), F is the Faraday constant, and $E_{Fc^{+}/Fc}$ is the redox potential for the ferrocenium/ferrocene couple used as reference (0.4 V *vs*. SHE in MeCN).

2.5 Electrochemical method

This thesis work deals with the different oxidation states of metal complexes, and it is not surprising that electrochemistry is intensively used. Electrochemistry studies the heterogenous electron transfer process between a redox-active species, dissolved in solution, and an electrode surface. Many different electrochemical techniques can be used to investigate the thermodynamic and kinetic of an electron transfer process. For this thesis, we have used cyclic voltammetry (CV) for investigating the electrochemical response of our samples and controlled potential electrolysis (CPE) to quantitively oxidized our compound to (i) produce a different species, which is then characterized with other spectroscopic methods, and (ii) supply the driving force for homogenous water oxidation catalysis.

2.5.1 General introduction of cyclic voltammetry

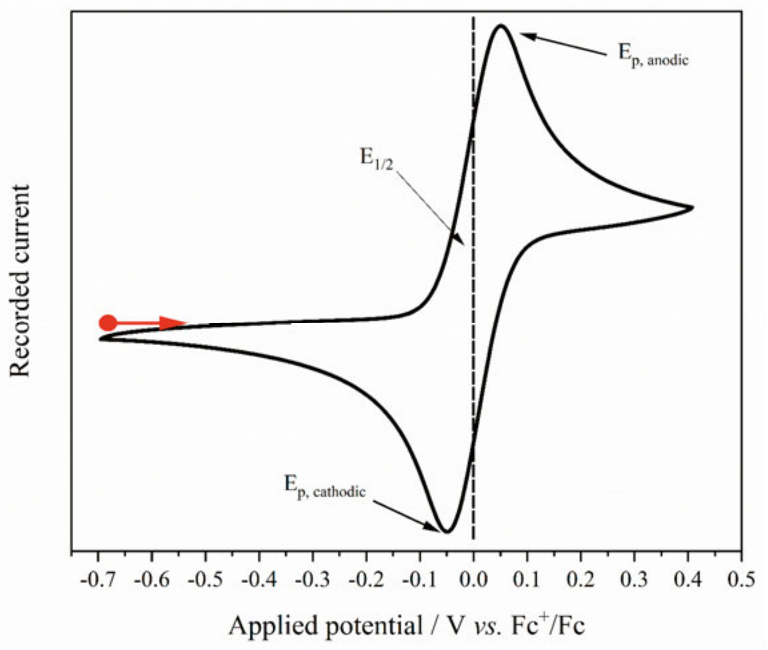

Figure 2.7 *– Cyclic Voltammogram of Ferrocene in acetonitrile.*

The cyclic voltammogram represented in Figure 2.7 represents the current generated as a function of the applied potentials of the ferrocene (Fc, reduced) complex present in the solution. A positive oxidative potential scan induces the oxidation of the species to Fc^+ (represented as an anodic current peak) until the potential is scanned backward and the reverse reduction reaction occurs. This follows the Nernstian relation in Eq. 2.11, where $E^{0\prime}$ is the formal redox potential for the species Fc^+/Fc, R is the universal gas constant, n is the number of electrons F is Faraday´s constant, and T is the temperature expressed in Kelvin.

$$E = E^{0'} + \frac{RT}{nF}\ln\frac{[Fc^{+}]}{[Fc]} \qquad \text{Eq. 2.11}$$

Because other mass transportations are suppressed (i.e., the migration transport due to electrical field gradient or mechanical convection), the shape of the current is defined by the diffusion of new reagent molecules to the electrode (i.e., the electron transfer is faster than the diffusion of Fc). The total recorded current is the superimposition of two contributions. The charging current is due to the capacitive behavior of the electrolyte solution (i.e., a transient current is generated because of each potential step and is linearly dependent on the scan rate, υ) and the Faradaic currents generated from the heterogeneous electron transfer of the electroactive species. The Randles-Sevcik numerical solution of the diffusion transfer law (Second Fick´s law) is applicable for a system in reversible Nernstian equilibrium of Eq. 2.11 (i.e., the electron transfer is considered fast) and defines the shape of the CV curves. The peak intensity is described in Eq.2.12

$$i_p = 0.446nFAC_R^{*}\left(\frac{nFD_R\upsilon}{RT}\right)^{1/2} \qquad \text{Eq. 2.12}$$

Where A is the electrode surface in cm^2, D_R and C_R* are the diffusion coefficient and the molar concentration in the solution of reduced species, respectively, and is the potential's υ scan rate. Eq. 2.12 shows a linear dependence between the concentration of the species and the recorded peak current. Moreover, the latter is proportional to the square root of the scan rate. If the generated oxidized species is unstable during the time of the experiment, the cathodic peak will result in a less intense peak or might even be absent, thus generating a quasi-reversible and irreversible wave, respectively. Other important information can be extrapolated from the position of the reversible peaks such as the half peak potential, $E_{1/2}$, which is a very good approximation of the formal redox potential of the species in solution, $E^{0'}$, and the peak-to-peak separation ΔE_p, which is inversely proportional to the number of electrons, n, transferred ($2.22\ RT/nF$).[136]

2.5.2 CV's experimental details

In a typical CV experiment, a three-electrode system is used (Figure 2.8). A glassy carbon electrode of 3 mm diameter is employed as a working electrode. A potential scan is applied (0.1 V s^{-1}) on the working electrode by referring it to a reference electrode of which potential shall be constants during the time of the experiment. A counter electrode, made of a platinum wire, has the role of closing the electron flow. The experiment is controlled by a potentiostat, which has a high resistant circuit between the reference electrode and working electrode to supply a defined potential and a second circuit between the working and counter electrodes. In the latter, the current is detected, and an arbitrary high potential is applied on the counter electrode to ensure that the current depends only on the working electrode redox reaction. The experiment is conducted in an unstirred solution. To ensure the only diffusion limit of the current on the working electrode, a highly concentrated solution (0.1 M) of an inert salt (called supporting electrolyte) is added. This also warrants a low cell resistance. The electrolyte solution was purged with MeCN-saturated argon gas to remove all dissolved O_2, which can react with the oxidized intermediates produced in the proximity of the electrodes. The working electrode was carefully polished with 1 μM, 0.3 μM, and 0.005 alumina water suspension to have the highest reproducibility on the surface area of the electrode.[137]

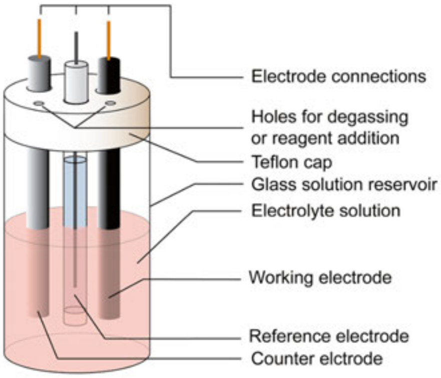

Figure 2.8 *– Electrochemical cell configuration for CV experiments. reprinted with permission from ref. [137]. Copyright 2018 American Chemical Society.*

For CVs conducted in MeCN, 0.1 M tetrabutylammonium hexafluorophosphate ($TBAPF_6$) was used as a supporting electrolyte. In this case, the reference electrode was a custom-made quasi-reference electrode which was made as follows. A brown coating of silver chloride was deposited on a silver wire by applying 1.2 V in a potassium chloride solution (3 M). The wire was then sealed in a porous glass-tipped tube and refilled with the same electrolyte solution of the chemical cell. The redox potential drift of the quasi-reference electrode was regularly checked with an Fc solution in MeCN used as reference $E_{1/2}$ (Fc^+/Fc) = 0.47 V *vs.* Ag pseudo reference. The same redox couple was also used as a reference for the reported redox potential (E^O(Fc^+/Fc) = + 0.624 *vs.* SHE).[138]

For the CV conducted in buffer solution (a 9:1 mixture of Borate buffer 100 mM at pH 8.0 and dry MeCN) the reference electrode was a Ag/AgCl 3M KCl ($E^{0'}$(Ag/AgCl) = + 0.210 *vs.* SHE).

2.5.3 Controlled potential electrolysis

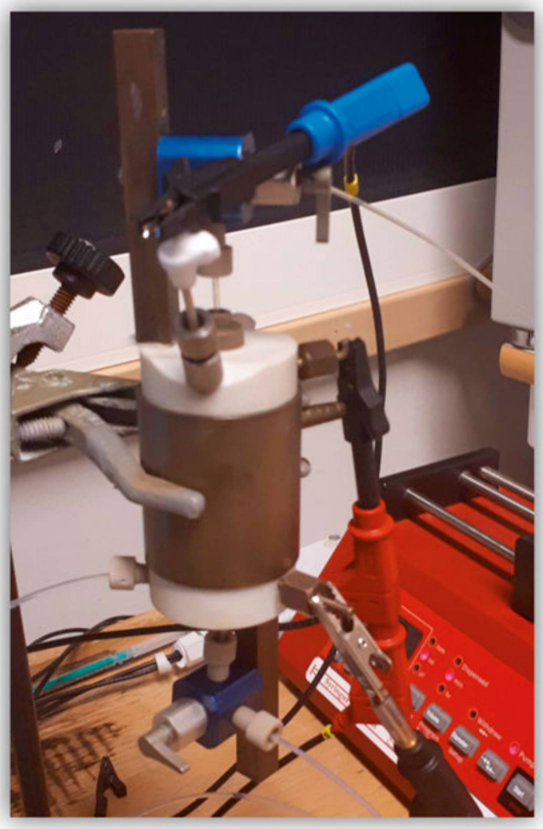

***Figure 2.9** – Flow cell for CPE samples preparation*

The oxidation of the metal (II) complexes was conducted in a custom-made electrochemical flow cell (Figure 2.9). A leak-free Ag/AgCl in 3M KCl electrode was used as a reference electrode and placed in proximity of the electrode. Working and counter electrodes are made of Reticulated Vitreous Carbon (RVC), and they are cut with a cylindrical shape and are placed inside the cell with a glass frit to divide the two compartments. During a classical sample oxidation procedure, the cell is refilled with an electrolyte solution ($TBAPF_6$, 0.3 M in MeCN), and 10 CV scans are applied in order to activate the electrodes´ surface (-1.0 to +1.5 V, 10 mV s^{-1}). The sample solution is injected into the working electrode compartment, and a preliminary CV is recorded in order to determine the oxidizing offset potential. The electrolysis is accomplished by flowing the sample solution (1 mM in acetonitrile and electrolyte) through the working electrode using a syringe pump, pushing the piston of a 5 ml glass syringe (injection speed rate: 0.05 ml/min). A Teflon tube, placed in proximity of the glass frit, guides the oxidized product out of the cell, and, in the case of 5.6% volume of water addition, a t-valve permits the product to be mixed with a 11.4% water-MeCN solution before collection. The success of the oxidation is monitored by the recording of both the flow current (usually on the order of 0.2 mA for a 0.05 ml/min flow rate) and changes in the UV-Vis spectrum.

CPE measurements for oxygen evolution were conducted in a Clark-type electrode cell for on-line O_2 measurements (Figure 2.10 and see Section 2.6). The working electrode was a GC plate (dimension 5.0 x 5.5 x 1 mm) connected to the potentiostat with a thin electrical cable that is sealed and insulated on the electrode surface. Due to the small dimension of the cylindrical cell (1 x 20 cm) a customized mini reference electrode was designed. The tip of a thin electrical cable was soldered with a 5 mm long silver wire. An AgCl layer was deposited onto the electrode following the procedure described above. It was sealed in a capillary tube 6 mm long which was refilled with a 3 M KCl solution. The free end of the tube was filled with molecular sieves as a membrane. The stability of the reference electrode was checked at the end of each CPE by measuring the $E_{½}$ of $K_4[Fe(CN)_6]$ ($E^{0'}_{FeIII/FeII}$= 0.266 V vs. Ag/AgCl 3M KCl). The counter electrode was a GC rod immersed in the electrolyte buffered solution in a glass tube sealed with a polymeric porous material.

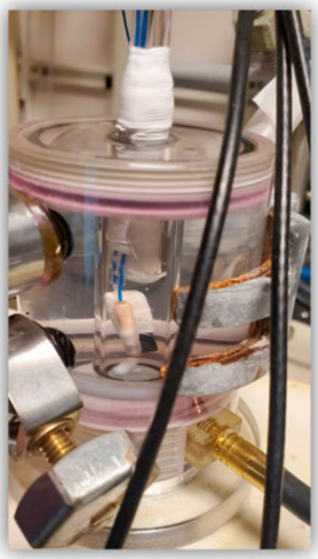

Figure 2.10 *– Clark-type electrode coupled with electrodes for CPE experiment.*

When operating, the counter electrode assembly functioned as a lid for the Clark electrode cell, which was filled with 1.6 mL of 0.5 mM complex solution in borate buffer 90 mM pH 8.0 10% $^{v}/_{v}$ MeCN. No headspace was left, and the working electrode and the mini reference electrode were completely immersed in the stirred solution. The applied potential of 1.78 V vs. Ag/AgCl 3M KCl (2 V *vs.* SHE) has been chosen based on the current detected level (at least 50 µA), and the amount of O_2 evolved. The CPE was conducted for 25 minutes. The charge quantification for the Faradaic efficiency determination was done after CPE by the integration of the measured current with the instrument´s software. Before and after each experiment, the working electrode was polished with 1.0 µM alumina suspension (3 minutes each side of the plate). The cell was cleaned with distilled water and HCl 0.01 M to remove metal traces that might deposit on the electrode surface in the following experiment. A rinse test on the GC plate was done to investigate if electrodeposition of iron metal oxides occurred in the CPE with the iron complex. This was conducted by rinsing the electrode with distilled water and acetonitrile; hereby, we were careful not to scrub the electrode and accidentally remove the possible metal oxide layer. A new CPE was run in fresh buffer with electrolyte.

2.6 O_2 detection

Oxygen evolution detection was done with two different instruments depending on the investigated oxygen evolution assay.

Chemical-driven and electrochemical oxygen evolution was conducted with a Clark electrode oxygen detector. The electrode is composed of a platinum working electrode and a silver counter electrode. A saturated KCl solution is used as an electrolyte, and a Teflon membrane separates the system from the test solution. A reducing potential is applied on the platinum, and the reaction in Eq. 2.12 takes place.

$$O_2 + 4\,e^- + 4\,H^+ \rightarrow 2\,H_2O \qquad \text{Eq 2.12}$$

The electrons generate a current response proportional to the amount of oxygen. The calibration is done by measuring two points: O_2-saturated water solution and a degassed water solution. The electrode is placed on the bottom of the Clark cell, and the solution is stirred. The solution is held at 22 °C with a thermostat. For the electrochemical oxygen evolution experiment, the electrodes are placed into the solution from above (See Figure 2.10). A chemical oxidation experiment is conducted by adding 900 µL of 11.1 µM complex solution in 44 mM borate buffer at pH 8.0, and 0.2% $^{v}/_{v}$ MeCN into the cell and wait for equilibration of the oxygen signal. A 6 mM $[Ru^{III}(bpy)_3](ClO_4)_3$ solution is prepared in water, and 100 µL are added to the cell (final concentrations: 10 µM complex, 600 µM $[Ru^{III}(bpy)_3](ClO_4)_3$, 40 mM buffer). The blank experiment is conducted in the same way but in the absence of the tested complex. The cell was cleaned with distilled water and HCl 0.01M solution between experiments.

Time resolved membrane inlet mass spectrometer (TR-MIMS) was chosen for the light-driven experiment because of its high O_2 sensitivity (nM of O_2) and reproducibility. The instrument is designed to detect different oxygen isotopes simultaneously, but for this experiment, the detector was tuned and calibrated only for mass 32. The instrument is connected to a thermostated transparent cell (22 °C) with an inlet placed on the bottom. A silicon membrane supported by porous plastic support separates the instrument's vacuum (~ 10^{-7} bar) from the solution. A customized blue LED array (470 nm, 24.8 mW) is placed around the cell, and a shutter controls the illumination. The concentration of photosensitizer ($[Ru(bpy)_3](ClO_4)_2$) and sacrificial acceptor ($Na_2S_2O_8$) were optimized for this system. We observed that a higher concentration of persulfate, for example, induces uptake of oxygen, probably due to the oxidative reaction on the photosensitizer. A higher concentration of photosensitizer, on the other hand, reduces the amount of produced oxygen because the light source cannot homogeneously illuminate the solution. Thus, a typical optimized experiment is as follows.

Under red dim light conditions, 600 µL of 1.25 mM $[Ru^{II}(bpy)_3](ClO_4)_2$ were mixed with 600 µL of borate buffer 100 mM pH 8.0, 150 µL of 100 µM of complex dissolved in water with 2% $^{v}/_{v}$ MeCN (or 150 µL of distilled water with 2% $^{v}/_{v}$ MeCN for the blank experiment) and 150 µL of 25 mM $Na_2S_2O_8$ (final concentrations: 500 µM of $[Ru^{II}(bpy)_3](ClO_4)_2$, 40 mM of buffer, 10 µM of complex and 2.5 mM of $Na_2S_2O_8$). After mixing, 1 ml of the photosensitive reaction mixture was inserted into the TR-MIMS's cell, and a plunger was placed to create a gas-tight system. The solution was kept dark and stirring for 20 minutes, allowing the instrument's vacuum to degas the solution. When the mass 32 detector reached a stable value of approximately 2000 mV, the shutter for the illumination was opened, and the oxygen trace was recorded for 10 minutes. Because of the simultaneous depletion of the oxygen by the mass spectrometer, an oxygen peak is observed rather than a stepwise increase. The top of the peak marks the point where the oxygen evolution rate starts to decrease below the gas diffusion rate of the membrane.

The cell was rinsed with distilled water and HCl 0.01 M between experiments in order to remove possible metal oxide deposits. To ensure good reproducibility, fresh solutions of all the reagents were made daily, and the blank experiment was alternated with the experiments in the presence of the complex. The calibration of the instrument was done every day by injecting different amounts of oxygen-saturated distilled water at 22 °C (274 µM) into the cell containing 840 µL of degassed water. A figure of the system is shown in Figure 2.11.

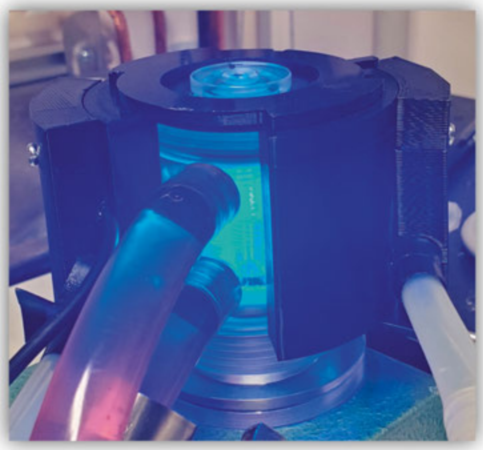

Figure 2.11 *– TR-MIMS set-up for a light-driven experiment.*

Paper I

Chapter 3

An Unexpected Spin Crossover Behavior

3.1 Introduction

As introduced in the previous chapter, spin crossover (SCO) is the ability of complexes to switch between different spin states depending on external inputs (i.e., temperature, pressure, light, and guest molecule inclusion in the lattice).[112] This molecular property, through cooperative and diffusive interactions among the spin centers, permeates the entire material resulting in the macroscopic response on color, magnetic behavior, density, and catalytic selectivity. These open the field for many applications, like sensing for microthermometry[139], gas detection,[140, 141] actuators functioning via electronic[142], optoelectronic, magnetic[143, 144] proprieties, and switchable catalysts[145, 146]. Furthermore, SCO is often accompanied by hysteresis effects, which can be used for shape-memory functions and information storage.[147]

SCO occurs in d^4–d^7 metal complexes in which both HS and LS electronic configurations are energetically accessible because they are close in energy. Crystal field orbital splitting (Δ_O) and the intra-orbital electron pairing energy (P) are the two competitive energetic dimensions that rule the electronic configuration as shown in Figure 3.1 (for $\Delta_O > P$) a LS configuration is preferred and vice versa. An important aspect is that SCO affects the occupation of the antibonding orbital e_g, resulting in longer metal-to-ligand bond distances for a HS electronic configuration. SCO can therefore be tuned by a rational ligand design that controls the crystal field strength. For ferrous d^6 complexes, chelating nitrogen aromatics and π-acceptors ligands such as cyanate (CN^-) and thiocyanate (SCN^-) have been heavily employed for SCO systems development.[148-150] Halides ions, as ligands for SCO compounds, were never employed because they stabilize the HS state due to their weak-field behavior (i.e., the π-donor character lowers Δ_O) and the large anion radii.

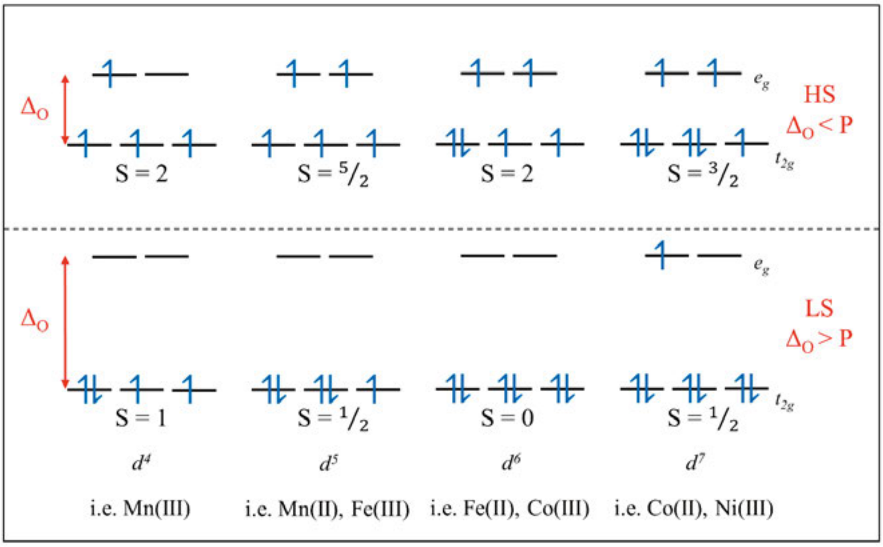

Figure 3.1 *– Octahedral ligand field splitting of metal ions with d^4-d^7 electronic configuration.*

Ferrous Py5OMe complexes with different apical ligands have been reported to undergo SCO with N_3^- and MeOH coordination, while the chloride ligated version remains, as expected, HS at all temperatures in the range between 4–300 K.[111] Also, the Py5OH analog of the latter was assigned as HS from the XRD structure conducted at 100 K.[84] However, during XAS measurements of the $[Fe(Py5OH)Cl]^+$ complex at 20 K, which was performed for the structural characterization of the $[M(Py5OH)Cl]^+$ compounds (see Chapter 4), we observed an unusually short coordination bond distance. Intrigued by this, we tested the solid complex by dropping it in liquid N_2 (~ 77 K), and a reversible color change from yellow to green occurred (Figure 3.2), which is ascribable to a SCO thermochromism behavior. We, therefore, investigated the structural and magnetic proprieties of the solid compound by SQUID and XAS and confirmed the unexpected SCO. We made use of DFT calculations to investigate the energetic contributions, and we also made a comparison to the analog Py5OMe complex. For this, a B3LYP* functional was tailored for a more accurate comparison of these compounds.

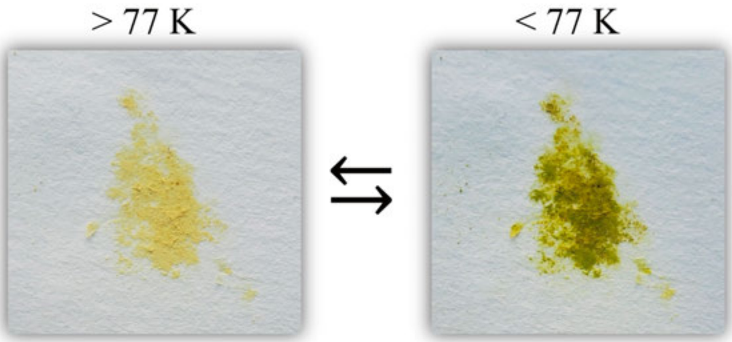

Figure 3.2 *– Reversible color transition of solid [Fe(Py5OH)Cl]PF_6 by dropping it in liquid N_2*

3.2 SQUID measurement

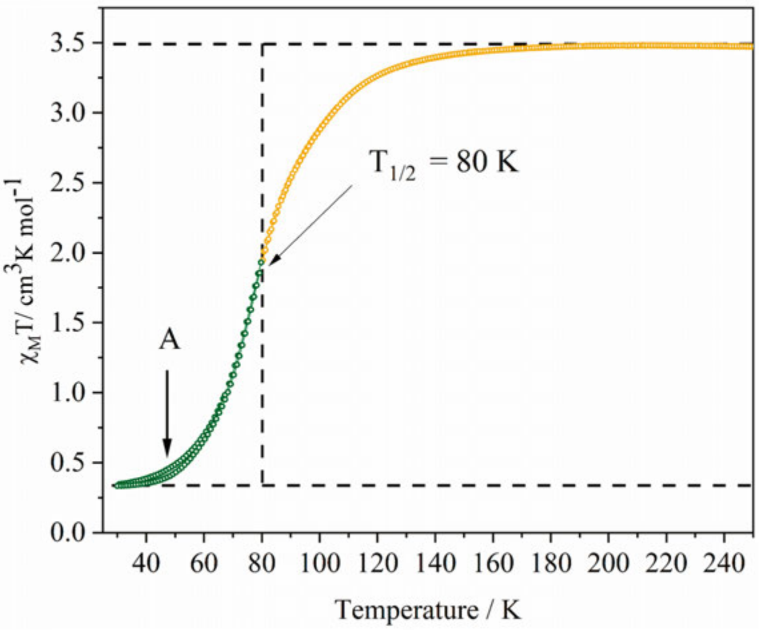

Figure 3.3 *– SQUID measurement of the solid [Fe(Py5OH)Cl]PF_6. Scan rate 2 K min^{-1}.*

The reversible spin transition of the solid [Fe(Py5OH)Cl]PF_6 taking place with the change of the temperature was monitored with a temperature-dependent SQUID measurement (the scan rate was 2 K min^{-1}). From room temperature to *ca*. 140 K, $\chi_M T$ remains constant at 3.4 cm^3 K mol^{-1}. Such value is consistent with a total spin $S = 2$ (according to Eq. 2.4), hence HS d^6. Upon further cooling to 40 K, $\chi_M T$ steadily decreases to 0.3 cm^3 K mol^{-1} which can be assigned as total loss of the electronic magnetization characteristic for a $S = 0$, LS compound. The same temperature scan is conducted in a warming regime. The reverse process is nearly identical except for a small hysteresis phenomenon (A in Figure 3.3) at *ca.* 50 K due to kinetic effects. $T_{1/2}$ for the solid [Fe(Py5OH)Cl]PF$_6$ was 80 K.

3.3 XAS measurements

The XAS spectra at 293, 150, and 20 K were measured to follow the structural changes induced by the spin transition observed with the SQUID experiment. Measurements conducted at the two highest temperatures are virtually identical. At 150 K, the K-edge transition is consistent with a $S = 2$ Fe(II) complex (HS). The simulated Fe–N and Fe–Cl bond distances reported in Table 3.1 are comparable to the XRD data recorded at 100 K.[84] At 20 K, the XANES spectra show an increased absorption for the forbidden $1s \rightarrow 3d$ transition (A) and a shift of the K-edge transition (B in Figure 3.4a). Both features are reported to be characteristic for LS ferrous compounds.[151-153] The EXAFS recorded below the SCO temperature shows a shorter distance between the absorber and all the nitrogen atoms, by *ca.* 0.2 Å, as it was previously reported for similar Fe(II) LS compounds.[154] Interestingly, even if the LS electronic configuration strengthens the metal-to-ligand bonding character, the simulated EXAFS shows that the Fe–Cl distance remains unchanged.

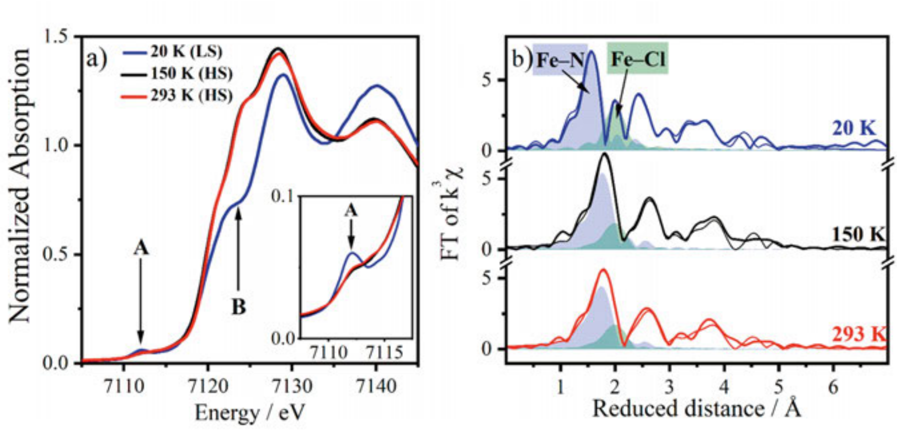

***Figure 3.4** – XANES, a) and EXAFS, b) of the solid [Fe(Py5OH)Cl]PF$_6$ at three different temperatures. Reprinted with permission of ref.[155].*

Table 3.1 *– Metal-to-ligand bond distances derived from EXAFS at different temperature and spin states assigned with SQUID and XANES.*

Temperature	**20 K**	**150 K**	**293 K**
Spin state	**LS**	**HS**	**HS**
Fe–$N_{average}$	1.993(3)	2.178(6)	2.169(7)
Fe–Cl	2.378(6)	2.38(2)	2.38(2)

3.4 DFT calculations

To rationalized the SCO behavior of the $[Fe(Py5OH)Cl]^+$, DFT calculations on this complex were made. The geometry optimization, with the B3LYP functional, of both the HS and LS electronic configuration, also shows a 0.19 Å shorter average Fe–N bond for the LS state, while the Fe–Cl distances remain virtually unchanged (- 0.03Å).

The experimental 80 K transition temperature was then used to tune *ad-hoc* the HF exchange contribution in the B3LYP functional with the idea to have a tailored functional which can systematically and accurately describe these compounds. The difference of the spin state energies (HS-LS) for $[Fe(Py5OH)Cl]^+$ were calculated at different HF exchange percentages. At the lowering of the HF exchange contribution, the energy of LS state decreases almost linearly (1.27 kcal/mol per 5% decrease), and the best fit with experimental results is observed with a 15% HF exchange contribution.

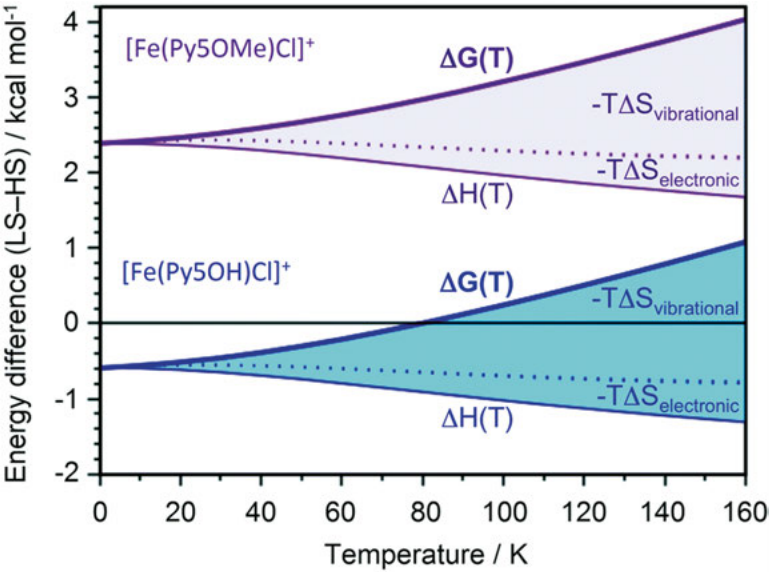

Figure 3.5 *– Calculated free energy (negative in sign) of the LS state relative to the HS as a function of the temperature. Reprinted with permission from ref.*[155].

Using the obtained B3LYP* functional, the relative free energies of LS to the HS state are calculated at different temperatures for the $[Fe(Py5OH)Cl]^+$ and the methoxyl substituted version, $[Fe(Py5OMe)Cl]^+$ (Figure 3.5). The vibrational entropic energy contributed to the increase of the relative energy towards the HS state and showed a similar trend for both complexes. The vibrionic entropic energy dependence is a consequence of the longer metal-to-ligand bond of the HS state, as described above.

For $[Fe(Py5OMe)Cl]^+$, the HS state is 2.3 kcal mol^{-1} more stable than the LS state, already at 0 K. Therefore, the absence of the SCO can also be computationally understood.

An analysis of the structure of the two compounds suggests that the steric effect of the OMe substituents accounts for the difference in SCO behavior between the sister complexes: by contrast to the Py5OH analog (Figure 3.6a), in $[Fe(Py5OMe)Cl]^+$ the axial pyridine is not parallel to the *z*-axis, but distorted by 30°(Figure 3.6b). This results in a weaker coordination bond which favors the HS state.

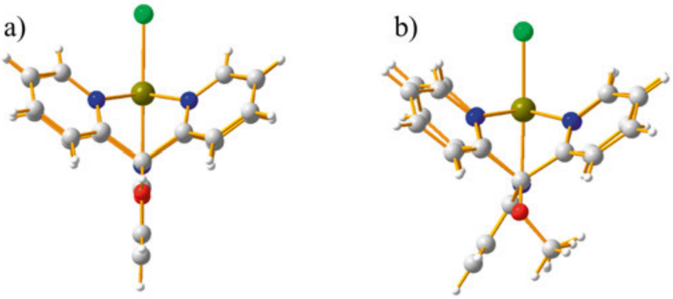

***Figure 3.6** – Calculated structure for $[Fe(Py5OH)Cl]^+$ (a) and $[Fe(Py5OMe)Cl]^+$ (b) in their HS states.*

3.5 Conclusion

This paper reported the first example of the SCO in a Fe(II) metal complex bearing a weak-field ligand. This unprecedented result will give an essential contribution to the research on SCO switchable materials.

In this work, SQUID was employed to determine the exact temperature at which the spin transient occurs, while XAS experiments highlight the structural differences between the two spin states. DFT calculations were used to rationalize these findings compared to the analog methoxyl-substituted complex, which remains HS at all temperatures. Finally, this computational study allowed us to tune the B3LYP functional to obtain more accurate DFT results in further studies of the Py5-type compounds, presented in Chapters 4 and 6.

Paper II

Chapter 4

Electrochemical and Structural Overview of Base Metal Py5OH Complexes

4.1 Introduction

So far, we have only focused on the magnetic proprieties of the iron and manganese Py5OH-ligated complexes connected with the already reported Py5OMe-family compounds. With this work, we wanted to lie our attention to the systematic comparison among four main base metal complexes ($[M(Py5OH)Cl]^{+}$ M = Mn, Fe, Co, and Ni) in their reduced (M^{II}) and oxidized form (M^{III}). X-ray techniques, namely XRD and XAS, are used to detect the structural changes upon dissolution in organic solvent and oxidation of the studied complexes, whereas the redox behavior is investigated by CV. In this paper, DFT calculations play a central role in rationalizing these finds and understanding the trends among the different metal centers that do not always follow the trends in the periodic table. The exchange reaction of the apical chloride ligand is also investigated as it might be the first step for substrate activation in catalytic applications. For this, a Cl-free complex was also made $[Fe(Py5OH)MeOH]^{2+}$, and we proved the exogenous nature of the new apical ligand, which changes according to the chosen solvent. Finally, this consistent study is compared with the related work reported by Stack´s group on the$[M(Py5OMe)Cl]^{+}$ complexes.[109]

4.2 Structural trends of M^{II} complexes and the molecular orbital configuration

Figure 4.1 shows the comparison of the metal-to-ligand bond distances of reduced $[M(Py5OH)Cl]^+$ metal complexes from the XRD crystal structures (recorded at 150 K) and the optimized geometry DFT calculations. The final free energy comparisons of the studied metal complexes were calculated at room temperature, with the B3LYP* functional adopted in Paper I. For all the reduced complexes, the HS electronic configuration was more stable. This is also confirmed by the bond distances extracted from the XRD crystal structures and the calculated optimized geometries. Trends of the metal displacement from the equatorial plane and the M–N bond distances follow the expected orbital contraction induced by the increased nuclear charge in the series. However, this is not true for the M–Cl distance, which, after a slight decrease from the Mn to the Fe complexes, increases to some extent for the Co and Ni complexes. Furthermore, the change of the ionic radius from Mn to Ni is five times smaller (0.03 Å) than what was observed for the average M–N distance difference (0.15 Å). These results are explained here based on molecular orbital analysis, which is supported by DFT calculations.

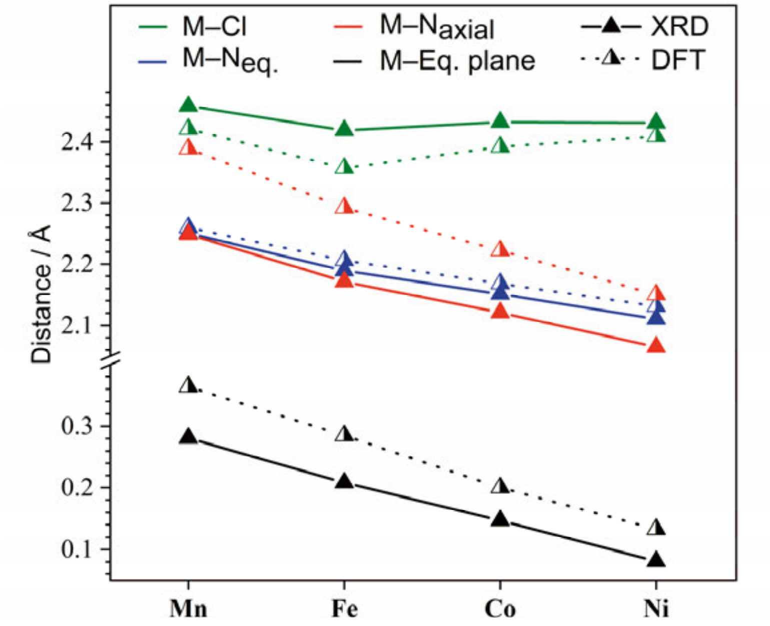

Figure 4.1 – Comparison of the distances from XRD and DFT for the $[M(Py5OH)Cl]^+$ metal complexes. Reprinted with permission of ref. [156].

From the XRD structures, $[M(Py5OH)Cl]^+$ complexes have a distorted octahedral geometry resulting in an approximated C_{4v} symmetry with the C_4-

proper axis parallel to the M–Cl ligand. The local tetragonal geometry transforms the t_{2g} and e_g orbitals to b_2 + e and a_1+ b_1. Pyridine (Py) ligands are known to be σ-donor and π-acceptor ligand while Cl$^-$ is a σ-donor and π-donor ligand. The resulting molecular orbitals (MOs) are obtained by mixing the metal 3*d* orbitals and ligand orbitals according to their symmetry (one bonding and one antibonding for each covalent interaction), as reported in the energetic diagram of Figure 4.2. The b_2 π-type bonding MO is formed by mixing the d_{xy} with the equatorial Py π-orbitals. Interestingly, the doubled degenerate d_{xz}/d_{yz} orbitals overlap with the Cl$^-$ p-orbital resulting in a π*-antibonding MO and π-bonding MO from the equatorial pyridines. These three MOs are labeled as π-type orbitals. Higher in energy, there are two σ*-type orbitals of antibonding character. The a_1 MO is formed by mixing d_{z2} and the axial ligands orbitals via σ interactions, while the b_1 MO is derived from the interaction of the $d_{x2\text{-}y2}$ with the equatorial Py σ-orbitals.

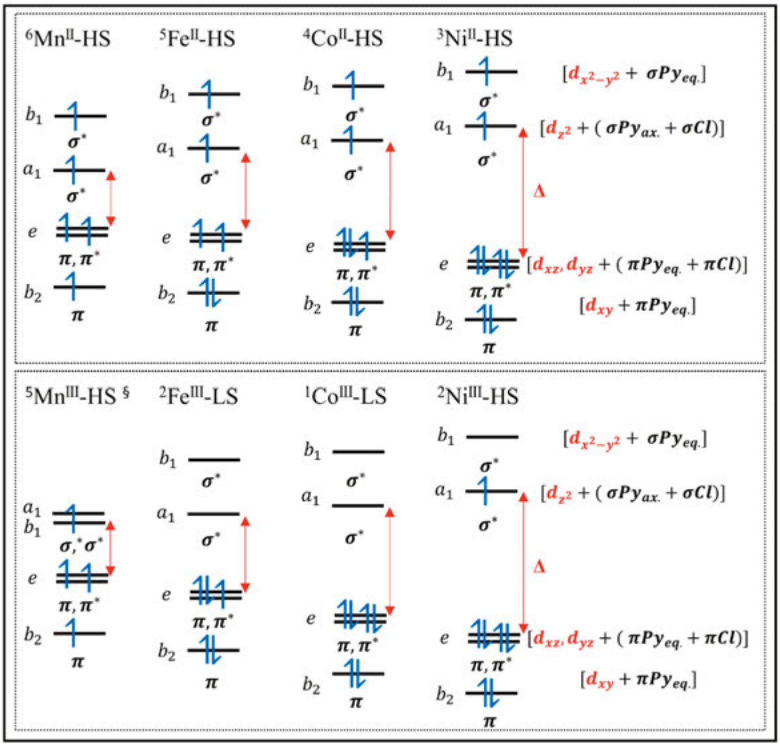
^{6}Mn^{II}-HS
^{5}Fe^{II}-HS
^{4}Co^{II}-HS
^{3}Ni^{II}-HS
b_1
a_1
e
b_2
σ*
π, π*
π
Δ
$[d_{x^2-y^2} + \sigma Py_{eq.}]$
$[d_{z^2} + (\sigma Py_{ax.} + \sigma Cl)]$
$[d_{xz}, d_{yz} + (\pi Py_{eq.} + \pi Cl)]$
$[d_{xy} + \pi Py_{eq.}]$
^{5}Mn^{III}-HS §
^{2}Fe^{III}-LS
^{1}Co^{III}-LS
^{2}Ni^{III}-HS
σ,*σ*

Figure 4.2 *– Molecular orbitals scheme of the reduced (M^{II}) in the upper panel and oxidized (M^{III}) in the lower panel of the [M(Py5OH)Cl]$^+$ metal complexes with their spin multiplicity. In the square bracket, the respective metal-ligand orbitals are indicated. The field splitting for the C$_{4v}$ geometry is marked with Δ. § MO structure for the distorted structure discussed in the text.*

With the increase of the nuclear charge, from Mn to Ni, the energy of the metal's 3*d* orbitals lower. This results in better interaction with the low-lying filled ligand orbitals but likely worse overlap with empty ligand orbitals (e.g., in π back-bonding). On the opposite direction, the σ*-antibonding orbitals get lower in energy from Mn to Ni. As covalency increases, the σ*-antibonding MOs get higher relative to metal 3*d*, but as metal 3*d* are lower, the total effect is that σ*-antibonding MOs lowered.

The interesting trend of the M–Cl bond can be also be rationalized with the analysis of the MO theory. Since all the complexes are HS, all the MO are occupied with at least one unpaired electron (see Figure 4.2 upper panel). Going from the Mn to the Ni complexes, the number of electrons in the lower π-type MO goes from 3 to 6, while in the σ-type MOs, the unpaired electron constantly remains 2.

From $[Mn(Py5OH)Cl]^+$ ($\pi^3\ \sigma^2$) to $[Fe(Py5OH)Cl]^+$ ($\pi^4\sigma^2$) a spin down electron is added to the b_2 π-bonding MO. This results in a contraction of all the distances. The situation is more interesting from $[Fe(Py5OH)Cl]^+$ to $[Co(Py5OH)Cl]^+$. In this case, the electron of the Co complex occupies one of the two degenerate MO, which, as we mentioned above, is bonding for the equatorial Pys and antibonding for Cl^-. Even if the metal´s orbital energy lowers from Mn to Fe, the antibonding effects dominate, and a longer Co–Cl distance is observed, while a contraction on the Co–N bond length occurred due to the respective bonding character. Finally, from $[Co(Py5OH)Cl]^+$ ($\pi^5\sigma^2$) to $[Ni(Py5OH)Cl]^+$ ($\pi^6\sigma^2$), the electron is also added in the *e* MO. The counter effect of the bonding/antibonding character of this π-type MO, together with a further lowering of the 3*d* orbital, results in a further contraction of the Ni–N distances and an almost unchanged Ni–Cl bond length.

4.3 Solvent effects

XAS measurements conducted at 20 K corroborate with DFT simulations, highlight the non-trivial solvent effect on the $[M(Py5OH)Cl]^+$ complexes. Metal-to-ligand distances, obtained by EXAFS simulations of spectra for the solid samples, are consistent with the XRD crystal structures and the calculated HS geometries. The only exception is for the $[Fe(Py5OH)Cl]^+$ complex, for which the XANES spectrum and the metal-ligand distances are typical for the LS state. For more insights on the spin transition phenomenon for the $[Fe(Py5OH)Cl]^+$, see Chapter 3. The XAS spectra of the complexes dissolved in acetonitrile electrolyte solutions give similar XANES and EXAFS spectra to what was recorded for the solid samples. Once again, the only exception is for $[Fe(Py5OH)Cl]^+$, which three species were identified. The best EXAFS fitting is composed by (i) 40% of LS $[Fe(Py5OH)Cl]^+$ species also observed in the solid sample, (ii) 40% of HS $[Fe(Py5OH)Cl]^+$, and (iii) 20% of a LS species in which the chloride ligand is exchanged with a MeCN solvent molecule. Interestingly, the presence of the solvent electrolyte favors the ligand exchange and prevents the complete SCO at 20 K.

4.4 Structural trends of the oxidized M^{III} complexes

The [M(Py5OH)Cl]$^+$ complexes were oxidized in MeCN with electrolyte and recorded with XAS. The one-electron oxidation was confirmed by the K-edge shift for all the complexes except for [Ni(Py5OH)Cl]$^+$. Its high oxidation potential (see next section) did not allow us to obtain a quantitative conversion. A comparison of the metal-to-ligand distances obtained from EXAFS simulation and DFT analysis is reported in Figure 4.3. Compared to the reduced complexes, the metal-ligand distances do not follow a simple trend.

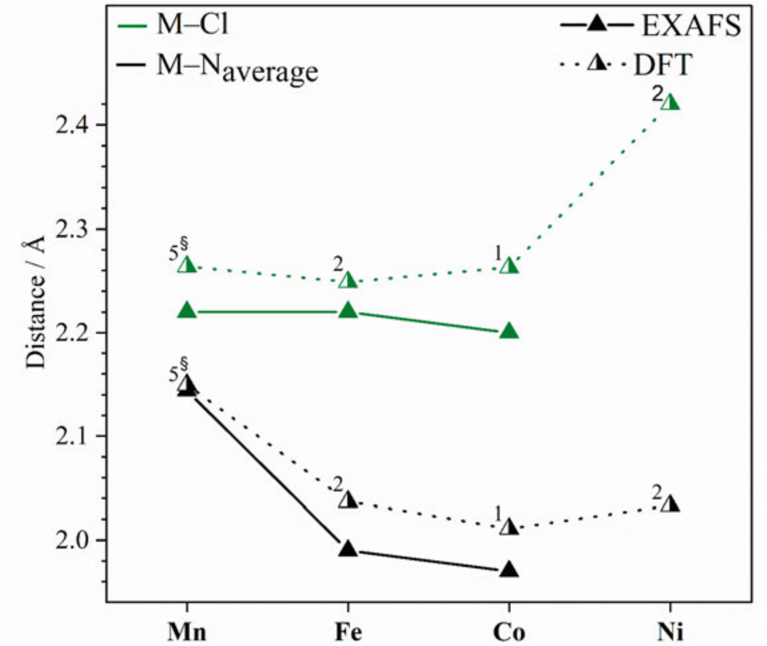

__Figure 4.3__ – Comparison of the distances from XRD and DFT for the oxidize (M^{III}) [M(Py5OH)Cl]$^+$ metal complexes. Numbers indicate the spin multiplicity. § Calculated distorted structure as described in the text. Reprinted with permission from ref.[156]*.*

The most significant deviation between experimental and calculated results is observed for the [Mn^{III}(Py5OH)Cl]$^{2+}$ complex. The EXAFS simulation gives a much shorter Mn–Cl distance compared to the calculated ($\pi^3\sigma^1$) quintet structure (2.22 Å and 2.40 Å, respectively), while a good match is found for the M–N distances. A simple explanation for the shorter than expected Mn–

Cl distance could be removing an electron from the a_1 MO of the reduced complex. However, this is not possible because a_1 is predicted to be lower in energy than b_1 (see Figure 4.2 upper panel). An alternative quintet structure (§) with shorter axial ligand and slightly elongated equatorial Mn–N distances was proposed. The energy difference to the initially calculated quintet is only 0.6 kcal mol^{-1}, and it is more consistent with an empty a_1 MO (Figure 4.2 lower panel).

For the oxidized iron complex, $[Fe^{III}(Py5OH)Cl]^{2+}$, the EXAFS fits well with a Cl-coordinated LS Fe(III) species. In contrast, we observed the presence of three species for the reduced compound. Consequently, the oxidation of the metal center caused the reversal of the exchange of the chloride ligand. The calculated metal-ligand distances for the LS configuration agree with the Fourier transform (FT) of the EXAFS. Even though, the energy difference between the HS sextet ($\pi^3\sigma^2$) and the LS doublet ($\pi^6\sigma^0$) is only 1.1 kcal mol^{-1}.

For the oxidized $[Co^{III}(Py5OH)Cl]^{2+}$ complex, the shortening of all the distances is comparable with a LS configuration as supported by DFT in which the HS Co(III) quintet ($\pi^3\sigma^1$) is 26.4 kcal mol^{-1} higher in energy than the LS singlet ($\pi^6\sigma^0$). Finally, for a hypothetical $[Ni^{III}(Py5OH)Cl]^{2+}$ complex, the doublet ($\pi^6\sigma^1$) spin electronic configuration is the most stable compared to a quartet ($\pi^5\sigma^2$, +16.7 kcal mol^{-1}). The LS configuration place an electron on the π^*-antibonding causing the elongation of all the metal-ligands bonds, with particular destabilization of the Ni–Cl. Overall, the structures of the oxidized samples are dictated by the progressive increase of the field splitting, which stabilizes the LS configuration.

4.5 Trends of the experimental redox potentials

The CVs of the studied complexes, reported in Figure 4.5, show reversible oxidation processes assigned to metal-centered one-electron oxidations. For the $[Fe(Py5OH)Cl]^+$ complex, a second wave of smaller intensity (*ca.* 25% of the total Faradaic process) is present at $E_{1/2} = 0.83$ V (in this chapter, all the redox potentials are referred to the redox couple Fc$^+$/Fc). This second reversible wave was assigned to the Fe(III→II) oxidation of the Cl-free $[Fe(Py5OH)MeCN]^{2+}$ species, as will be further discussed in Section 4.6. The small oxidation wave caused by the released Cl$^-$ is indicated by a * in Figure 4.4. These experimental results agree with the XAS measurement of the reduced iron sample in which the same species was identified.

The $E_{1/2}$ order for the oxidation of the chloride ligated complexes was: Co (0.08 V) < Fe (0.33 V) < Mn (0.58 V) < Ni (1.17 V). This trend does not follow the increasing potential due to lowering the 3*d* orbital energy as the nuclear charge increases.

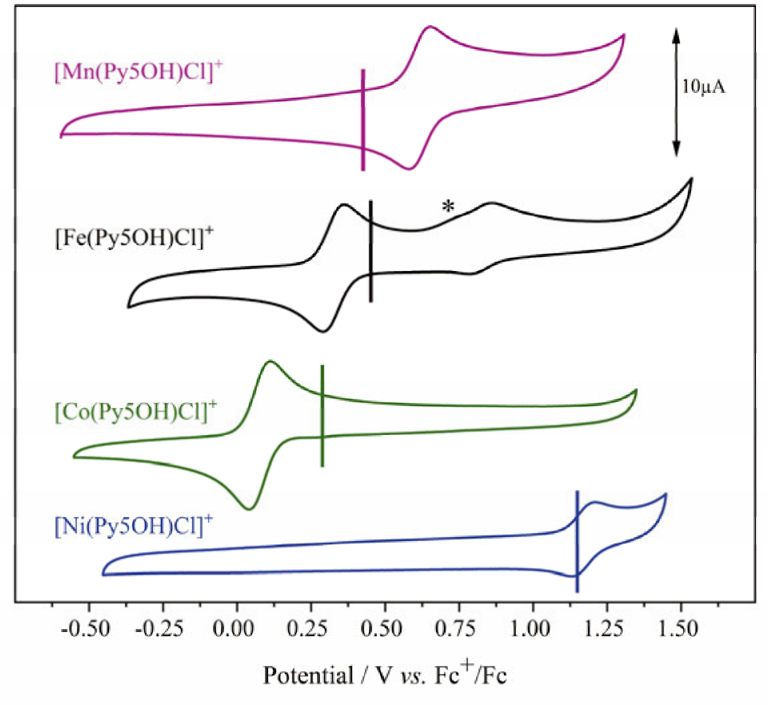

***Figure 4.4** – CVs of the [M(Py5OH)Cl]$^+$complexes in acetonitrile. Vertical lines indicate the calculated redox potentials for the II→III oxidation. * indicates Cl$^-$ oxidation. Reprinted with permission from ref.[156].*

Figure 4.4 indicates, with vertical bars, the calculated redox potential for each compound. The calculation of the redox potentials was done in a three-step process as described with the bars of different colors in Figure 4.5. The first step consists of removing an electron from the highest occupied MO, which is, for all the complexes, the σ*-type b_1 (see Figure 4.2), followed by orbital relaxation. The further geometrical relaxation allowed reaching the minimum energy geometry of the oxidized species. Ultimately, in case a more stable spin multiplicity existed, the spin changed was allowed. The comparison with experimental values (depicted as horizontal lines in Figure 4.5) highlights that once again, the more significant discrepancy comes from the oxidation of the [Mn(Py5OH)Cl]$^+$ complexes. A deviation of 0.24 V is within the expected accuracy of the method but relatively high with respect to the other complexes' results. The adoption of the new proposed quintet Mn(III) structure (§) gives only marginal improvement from the original quintet (0.37 and 0.34 V, respectively).

For the redox potential of [Fe(Py5OH)Cl]$^+$, the calculated value differs by only 0.04 V by considering that the oxidized quartet ($\pi^4\sigma^1$) Fe(III) undergoes spin relaxation to the most stable doublet ($\pi^5\sigma$).

A spin change is also required for the oxidation of $[Co(Py5OH)Cl]^+$ with a deviation from the experimental results of 0.11 V.
Finally, for the $[Ni(Py5OH)Cl]^+$ complex, the geometrical relaxation upon the b_1 σ^*-type MO electron removal gives a well-estimated redox potential with a deviation of only 0.02V.

The above-mentioned ‘expected’ trend on the redox potential is seen for the orbital and geometrical relaxation trends in Figure 4.5. It is only after accounting for the spin energetics that the experimental trends for the $[M(Py5OH)Cl]^+$ complexes are reproduced.

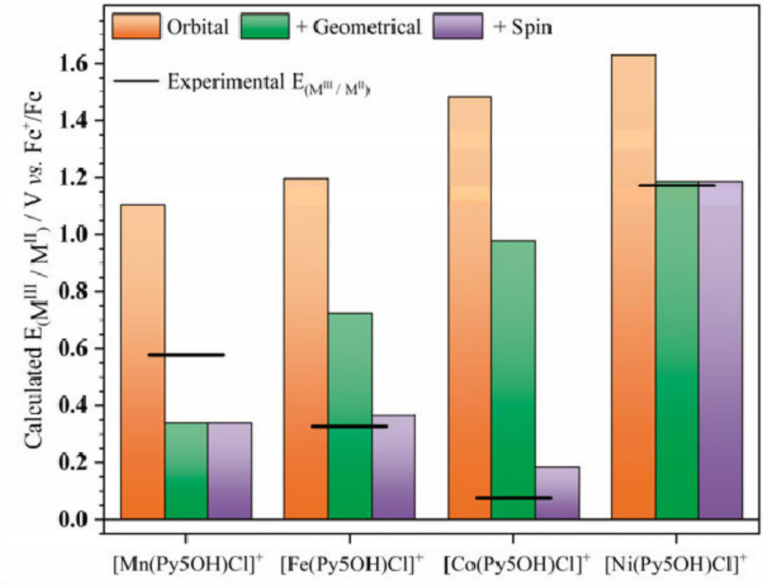

***Figure 4.5** – Calculated redox potential for the redox potential M(II/III) for the $[M(Py5OH)Cl]^+$ complexes considering a three-step process: (i) electron removal and orbital relaxation, (ii) geometrical relaxation, and (iii) spin relaxation. Horizontal bars are the experimental values.*

4.6 Apical ligand exchange

From the CV experiment shown in Figure 4.4 and the XAS results of the dissolved complexes,[156] there were indications that the $[Fe(Py5OH)Cl]^+$ complex undergoes ligand exchange when dissolved in the electrolyte solution. To gain insight into this phenomenon, $[Fe(Py5OMe)MeOH)]^{2+}$ was synthesized. XRD of a crystal obtained from a DMF solution and the mass spectrometer analysis of an acetonitrile solution of the Cl-free iron complex confirmed that the apical ligand was easily exchanged with the solvent employed in the analysis.

The XAS measurements on the reduced and oxidized Cl-free iron complex in acetonitrile electrolytic solution (therefore $[Fe^{III}(Py5OH)MeCN)]^{3+}$) support a LS configuration for both oxidation states (singlet and doublet, respectively), as also supported by DFT calculations. The CV of $[Fe(Py5OH)MeCN]^{2+}$ reveals only a one-electron oxidation process at $E_{1/2}$ = 0.83 V, which matches with the second peak observed for $[Fe(Py5OH)Cl]^{+}$. The calculated redox potential differs only by 0.07 V from the experimental value. To confirm the nature of this exchange equilibrium, we performed a titration with an organic chloride salt (TBACl), which was monitored by UV-Vis and CV. Both show the progressive formation of the $[Fe(Py5OH)Cl]^{+}$ upon Cl^{-} addition. The chloride exchange with the solvent is fostered by the electrolyte salt, stabilizing the Cl^{-} ion in the organic solvent.

$$[M(Py5OH)Cl]^{+} + MeCN \rightleftharpoons [M(Py5OH)MeCN]^{2+} + Cl^{-} \qquad \text{Eq. 4.1}$$

DFT calculations on the ligand exchange equilibrium for all four metal complexes were computed by considering Eq. 4.1. Being able to coordinate a possible substrate molecule easily in the first coordination sphere is a requirement for a catalytic reaction. The Cl^{-} binding energy comparison among the series is shown in Figure 4.6 (green bars) and follows the M–Cl distance analysis trend in Figure 4.1. For the $[Fe(Py5OH)Cl]^{+}$ complex, the chloride binding is stronger with respect to the manganese compound because of the better orbital overlapping and stronger π-bonding. The Co–Cl bond is less strong because of the additional electron in the π*-antibonding MO. Finally, Ni–Cl resulted in being the strongest likely due to the lowering in the energy of metal orbitals. Based on these considerations, the Mn complex seems to be most favorable for chloride exchange. However, from the binding energies of the metals with the MeCN (blue bars), acetonitrile coordination favors the LS configuration for $[Fe(Py5OH)MeCN]^{2+}$, resulting in a strong binding which is almost comparable with the chloride ligated complex. For the other compounds, the HS configuration remains the most stable. Despite this, the Ni–MeCN bond is more stable than the Cl^{-} compound. Once again, the reason is likely to a better orbital overlapping in the LS $[Fe(Py5OH)MeCN]^{2+}$ product. From the difference in energy between products and reagents, the free energy for the exchange can be estimated (red bars in Figure 4.6). While for the Mn and Co complexes, the chloride exchange reaction seems thermodynamically unfavorable, for the Fe and Ni complexes, the reaction seems accessible with free energies close to zero. These theoretical results were confirmed by the experiments for $[Fe(Py5OH)Cl]^{+}$ but not for $[Ni(Py5OH)Cl]^{+}$. For the latter, the kinetic limitation seems to be the reason as many Ni(II) compounds have been reported to be kinetically inert.[157]

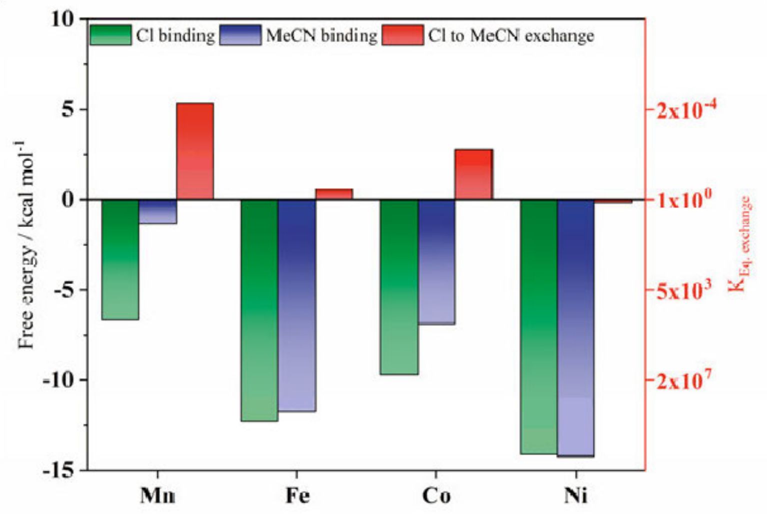

Figure 4.6 *– Calculated ligand binding energies for the [M(Py5OH)X]$^{+/2+}$ where M = Mn, Fe, Co, and Ni, and X = Cl$^-$ or MeCN. The free energy for the chloride exchange is shown as red bars*. Reprinted with permission from ref.[156].

4.7 Comparison with the [M(Py5OMe)Cl]$^+$ complexes

An important goal of this study was to systematically analyze the redox behavior and the structural changes among different base metals ligated with the Py5OH ligand. Similar work was conducted by Stack´s group of the related Py5OMe complexes, which differ only by the methylation of the distal hydroxyl groups. Chapter 3 highlighted that significant structural difference arises from the ligand distortion caused by the OMe functional groups on the axial pyridine ring. This lowers the overlap of the ligand with the metal orbitals, which stabilizes the HS configuration for the iron complexes at all temperatures.

Herein, we compare the redox potential also for the other metals bearing the Py5OMe ligand with our studied Py5OH-type compounds. In general, [M(Py5OMe)Cl]$^+$ complexes have a higher oxidation potential of ~ 0.08 V except for the [Ni(Py5OMe)Cl]$^+$, which potential was reported to be much lower than what was measured by us for the [Ni(Py5OH)Cl]$^+$ (see Table 4.1).

Based on our good agreement between experimental and calculated values, we believe that the reported oxidation potential for the [Ni(Py5OMe)Cl]$^+$ complex is not reflecting the same redox couple. The calculated redox potential for [Fe(Py5OMe)Cl]$^+$ is 0.11 V higher than the Py5OH-type analog. From the analysis of the oxidation process in Figure 4.7, the main contribution comes from the orbital relaxation, which is related to the electron extraction from the highest b_1 MO. The structural distortion observed for the Py5OMe ligand lowers the energy of the σ*-type b_1 due to poor orbital overlap. This effect is also reflected in the longer equatorial M–N distances with respect to the $[Fe(Py5OH)Cl]^+$ complex (+ 0.08Å).

***Table 4.1** – Oxidation half potential values for M(II/III) vs. Fc^+/Fc measured by cyclic voltammetry in acetonitrile at 21 °C of the $[M(Py5OH)Cl]^+$ complexes. Calculated redox potentials using the DFT method B3LYP* functional. The values are compared to the reductive half potential values vs. Fc^+/Fc reported by Stack et al. for the $[M(Py5OMe)Cl]^+$ complexes.[109]*

Metal	$E_{1/2}$ for $[M(Py5OH)Cl]^+$ (V *vs.* Fc^+/Fc)		$E_{1/2}$ for $M(Py5OMe)Cl]^+$ (V *vs.* Fc^+/Fc)	
	Exp.	**DFT**	**Exp.** [109]	**DFT**
Mn	0.58	0.34	0.66	-
Fe	0.33	0.37	0.40	0.48
Co	0.08	0.18	0.15	-
Ni	1.17	1.19	0.39	-

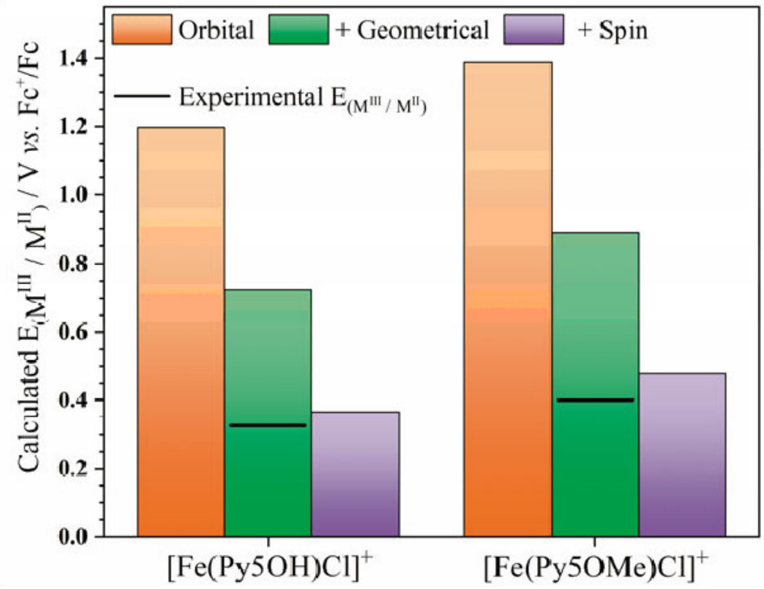

***Figure 4.7** – Calculated redox potential analysis for the oxidation M(II/III) of the $[Fe(Py5OH)Cl]^+$ and $[Fe(Py5OMe)Cl]^+$ complexes. Horizontal bars are the experimental values which, for the $[Fe(Py5OMe)Cl]^+$ was taken from the study of Stack's group.[109]*

4.8 Conclusion

In this extensive work, we analyzed the structural and electronic properties of the different divalent base metal complexes bearing the Py5OH-type and Cl^- ligands that determine their one-electron oxidation process. The results are summarized as follows.

1. All the solid $[M(Py5OH)Cl]^+$ complexes, where M = Mn, Fe, Co, and Ni, are in their HS configuration, except for the Fe complex when it is cooled to below 80 K.
2. The metal-ligand bond distances of the divalent compounds follow the periodic trends except for the M–Cl bond, which is influenced by the antibonding character of the *e* molecular orbital.
3. No changes in spin multiplicity or ligand binding are observed when the complexes were dissolved in the acetonitrile-electrolyte solvent. $[Fe(Py5OMe)Cl]^+$ is an exception to this. The complex's dissolution causes a partial (20%) substitution of the Cl^- ligand with a MeCN molecule. The new $[Fe(Py5OMe)MeCN]^{2+}$ species is LS at all temperatures. Moreover, the ferrous chloride complex in solution undergoes an incomplete spin change with half of the spin centers remaining HS at 20 K. Contrary to what is observed in the solid sample where the spin transition is complete. Upon oxidation, the exchange equilibrium in solution is reverted, and the chloride binds back quantitatively to the metal center.
4. The structural changes upon oxidation for $[Mn(Py5OMe)Cl]^+$ are tentatively explained by a ligand distortion occurring at the resulting HS Mn(III) compound. For the other complexes, the metal-to-ligand bond distances are dictated by the spin-energetics, which preferentially select the lower spin multiplicity. The same effect influences the redox potential order, which does not follow the increase of the nuclear charge along with the periodic table.
5. The chloride ligand exchange in solution occurs experimentally only for the $[Fe(Py5OMe)Cl]^+$ compound with a fast equilibrium supported by the presence of the electrolyte in the organic solvent. Calculated free energies for the reaction of the other metal complexes highlight how the MeCN coordination is thermodynamically favorable also for the Ni compounds, but its kinetic inertia makes this exchange not experimentally accessible.
6. The comparison with the analog Py5OMe compounds shows that a higher potential is required for their oxidation. This is most likely due to the stabilization of the higher b_1 antibonding orbital caused by the distortion induced by the OMe substituents.

Overall, this study provides the basis for a further reactivity analysis. The Fe compound seems the most promising for substrate binding regarding catalytic reactions. However, we have observed that the solvent can strongly influence the structural proprieties, which are also sensitive to temperature and electrolyte. Thus, it is essential to conduct the same systematic approach whenever a new species is added. This will be the focus of the Chapter 6 in relation to water oxidation catalysis.

Paper III

Chapter 5

Magnetic Anisotropy of Mn-Py5-Cl Complexes

5.1 Introduction

We have previously observed how the Py5-binding pocket in metal complexes can be used as a model to control the energy of the metal-ligand valence orbitals by tuning the ligand scaffold. The introduction of two methoxy functional groups in the peripherical position of the ligand induces a tilting of the axial pyridine. Compared to the Py5OH-ligated Fe(II) complexes, $[Fe(Py5OMe)Cl]^+$ has a worse metal-ligand orbital overlap, which lowers the antibonding orbitals energy and consequently increases the redox potential for the Fe(III)/Fe(II) couple. The magnetic proprieties are also affected, with the HS spin state being more stable than in the sister $[Fe(Py5OH)Cl]^+$ complex.

This chapter continues this analysis by investigating whether the magnetic ZFS propriety is also affected by this small ligand modification (See Section 2.3.1 for more details on ZFS). To do so, we employed the $[Mn(Py5OH)Cl]^+$ and $[Mn(Py5OMe)Cl]^+$ complexes. The choice of the Mn(II) ions as the metal center was made for the following reasons: (i) the paramagnetic behavior in EPR studies is well-known, (ii) the d^5 electron configuration gives access to different spin state interactions, which might enable interesting ZFS phenomena.

The rationalization of the ZFS and the related parameters *D* and *E/D* is still a 'hot-topic' because of the difficulty of finding a systematic approach to correlate ZFS with more general observables. Nowadays, ZFS parameters are extracted by fitting the experimental data. We still followed this path with this work by using EPR spectroscopy and the data extrapolated by fitting the spectra. However, we corroborate our findings with DFT calculations, which brings us closer to a general understanding of the ZFS´s parameters for the Mn(II)-Py5 systems.

As previously described in this thesis, ZFS arises from two types of phenomena: the first-order spin-spin (SS) interaction and the second-order spin-orbit coupling (SOC) between the ground state and the electronic excited state. Only systems with more than one unpaired electron having $S > 1/2$ are affected. The SS and SOC quantum mechanical interactions remove the degeneracy of the $2S + 1$ magnetic sublevels M_S, even in the absence of an external magnetic field. The ZFS Hamiltonian is described in Eq. 5.1.

$$H_{ZFS} = D\,[S^2_z - 1/3\ S(S+1)] + E(S^2_x - S^2_y) \qquad \text{Eq.5.1}$$

The interplay of standard X-band EPR (9.4 GHz) and the high-field high-frequency (HFHF) measurement with a W-band EPR instrument (94 GHz) helps to isolate the ZFS effect from the Zeeman contribution, which is field dependent. Neese's group developed DFT calculations based on couple perturbation theory (CP) as an accurate method to predict the SOC contribution and, therefore, studying the overall ZFS.[158-160] The details of CP go beyond the scope of this thesis. Here we analyze the effect of the different ZFS interactions affecting the *D* parameter as well as the different rhombicity between the two studied complexes. The effects of different amounts of the HF exchange contribution on the employed DFT functionals and level of approximations will not be discussed here, but more details can be found in Paper III.

5.2 X-band EPR

The EPR spectra of $[Mn(Py5OH)Cl]^+$ and $[Mn(Py5OMe)Cl]^+$ are both affected by the solvent employed, displaying hyperfine structure only in the BuCN/MeCN mixture and not in pure MeCN (Figure 5.1a). A closer look identifies several groups of hyperfine lines, each composed of six lines with approximately 8 mT splitting, typical for the mononuclear electron-nuclear dipole coupling for Mn(II) systems.[161]

The complex $[Mn(Py5OH)Cl]^+$, as well as the Py5OMe-ligated analog, has a Mn(II) described as a sextet (HS) metal center, which is evidenced by CV experiments and EXAFS analysis (see Paper III). Therefore, it was expected to observe the five $M_S = \pm1$ transitions at around $g = 2$, which is typical for an isotropic system with half-occupied d^5 orbitals. On the contrary, from Figure 5.1 it is possible to observe that the transitions cover a wider magnetic field range. This is characteristic of a highly anisotropic system. In this case, ZFS interactions are comparable or even more substantial than the field-dependent Zeeman splitting effect, resulting in a complicated spectrum characterized by inter-doublet transitions (see Section 2.3.1). A first attempt is to assign these transitions as a function of the rhombicity of the system, was done by using a rhombogram for a $S = 5/2$ system (Figure 5.1b). This gives an intermediate rhombicity value of $E/D = 0.12$.

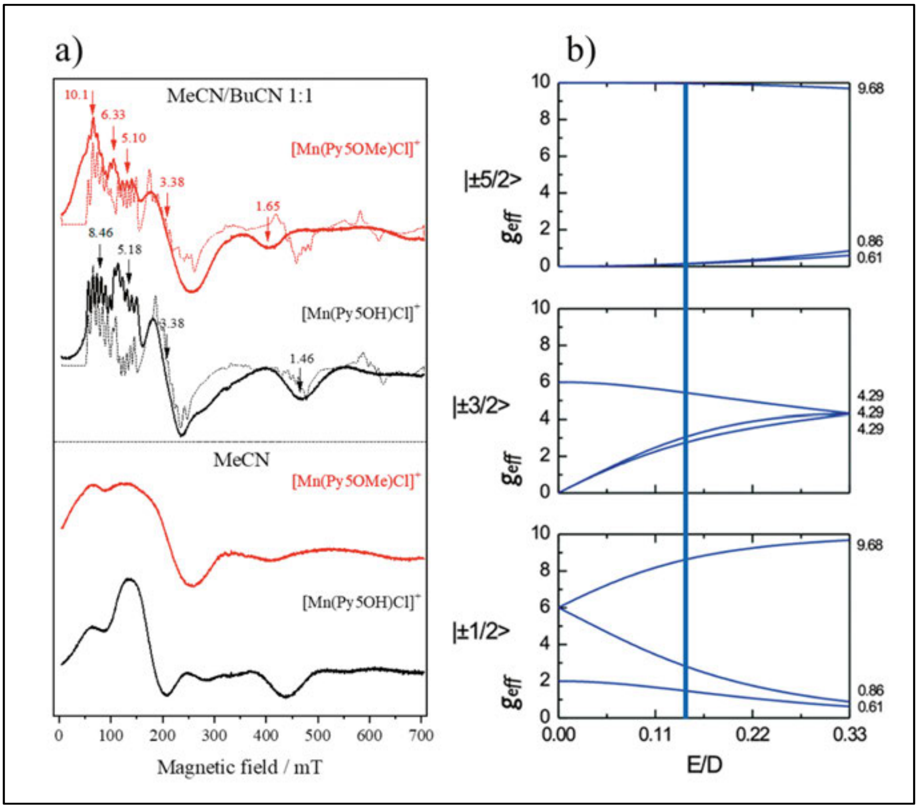

Figure 5.1 *– (a) X-band EPR of the [Mn(Py5OH)Cl]$^+$, black, and [Mn(Py5OMe)Cl]$^+$, red, in dry BuCN/MeCN 1:1 mixture (top panel) and dry MeCN (bottom panel), recorded at 10 K and 0.5 mW. The thin dashed lines are the simulated data. (b) Rhombogram for a S =5/2 system D > 0. The blue line covers the transitions observed for [Mn(Py5OH)Cl]$^+$. Figure (b) reprinted with permission from ref.*[162].

For the [Mn(Py5OMe)Cl]$^+$ spectrum, an additional feature at low field with $g = 10.10$ is found, and a more pronounced shift of the negative valley feature towards lower field, i.e., from $g = 1.65$ found for [Mn(Py5OH)Cl]$^+$ to $g = 1.46$. Overall, due to the close similarity between the spectra, we will consider the spectrum of [Mn(Py5OH)Cl]$^+$ as a model for the interpretation of the spin transitions.

5.3 W-band EPR

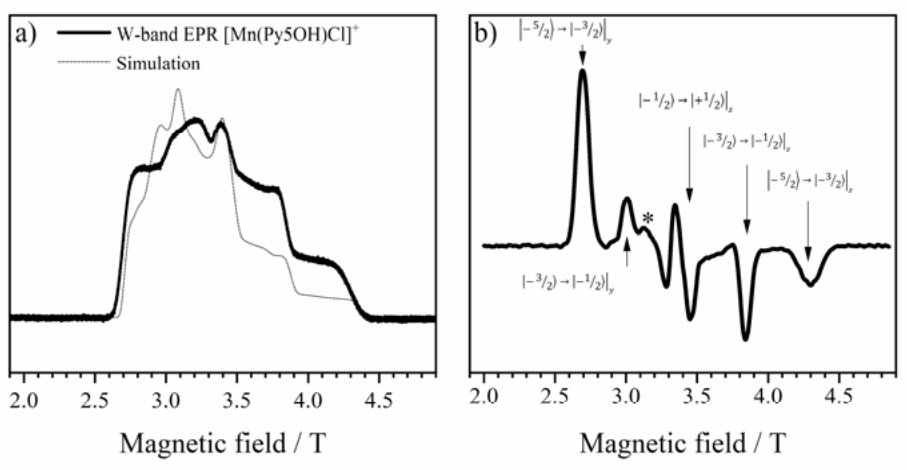

Figure 5.2 *– W-band EPR spectrum of the [Mn(Py5OH)Cl]$^+$ complex in acetonitrile recorded at 5 K. a) Experimental data (thick line) and the simulation (thin line) are shown. b) Pseudo-modulated spectrum with the EPR line transitions. The overlapping* |-*1/2>* →|+*1/2>*|$_{x,y}$ *transitions are marked as *.*

The advantage of measuring the [Mn(Py5OH)Cl]$^+$ sample with W-band EPR is that ZFS can be reduced so that primarily the Zeeman transitions are observed, while the ZFS remains a perturbation of the system. The spectrum collected in absorption mode (Figure 5.2a) and the corresponding pseudo-modulated transformation (Figure 5.2b) shows the EPR lines at around $g = 2$ (at ~ 3.4 T) because under the strong field conditions, the transition rule $\Delta M_s = \pm 1$ is obeyed. Once we identified the $g = 2$ transition M_S ±1/2 (|-1/2> →|+1/2>|$_{xyz}$) at 3.358 T, the sign of D can be determined by the relative position of the farthest EPR line, which is at 4.295 T (g_{eff}= 1.563) associated with the axial |-5/2> →|-3/2>|$_z$ transition. This occurs at a higher field (lower g), and therefore $D > 0$.[161] The D and E values are then estimated by the relative field distances from the centerline $g = 2$ (ΔB). Therefore, D = + 0.234 T (+ 0.218 cm^{-1}) from $\Delta B = 4D$, and E = 0.0336 T (0.031 cm^{-1}) from $\Delta B = 2|3E + D|$ in which the transition |-5/2> →|-3/2>|$_y$ (2.691 T, g_{eff} = 2.495) is considered. The resulting rhombicity (E/D) is 0.142, a value not far from what was obtained from the rhombogram in Figure 5.1b obtained with the X-band measurement. However, using W-band EPR spectroscopy, we had access to the spectral parameters D and E. Interestingly, the presence of the M_S = 1/2, 3/2, and 5/2 spin transition states confirm that all the lower states are populated even at 5 K.

5.4 EPR simulations

Zeeman splitting at X-band corresponds to approximately 0.3 cm^{-1}, comparable with the *D* values obtained by W-band EPR spectroscopy. This similarity indicates that employing the rhombogram of Figure 5.1b to determine the rhombicity gives only a rough estimation, as the rhombogram is valid only in 'weak filed' conditions (with Hamiltonian formalism: $H_{Zeeman} << H_{ZFS}$). We, therefore, computed EPR simulation using the Easy Spin software[163] and represented the outcomes as thin lines in the EPR spectra presented above. The resulting spectral parameters are summarized in Table 5.1.

Table 5.1 *– Spectral parameters obtained from the coupled simulation of the collected X- and W-band EPR spectra and comparison with values calculated by DFT.*

Tensors and Parameters	**[Mn(Py5OH)Cl]$^+$**		**[Mn(Py5OMe)Cl]$^+$**	
	Exp.	**DFT^a**	**Exp.**	**DFT^a**
g_1, g_2, g_3	2.175, 1.957, 1.990	--	2.200, 1.907, 2.016	--
A_1, A_2, A_3	284.52, 220.50, 196.53	--	245.9, 234.1, 178.0	--
D (cm^{-1})	0.220	0.245	0.215	0.240
E/D	0.142	0.027	0.160	0.070

[a] DFT was performed with BP86 functional and CP formalism, including the SMD solvation model with MeCN.

The EPR simulations confirm that both compounds have a relatively high anisotropy with [Mn(Py5OMe)Cl]$^+$ having a slightly higher *E/D* (+ 0.018) but smaller axial *D* parameter (- 0.05 cm^{-1}) with respect to [Mn(Py5OH)Cl]$^+$. Furthermore, the simulated energy diagrams as a function of the applied field show how the X-band allowed transitions are spread over a wide magnetic field range, while for the W-band, these transitions are gathered around $g = 2$ (see Figure 6 in Paper III).

5.5 DFT calculations

The *D* values for both compounds were also computed with DFT using the BP86 functional with the CP formalism. This resulted in values of $D = +\ 0.245$ and + 0.240 for [Mn(Py5OH)Cl]$^+$ and [Mn(Py5OMe)Cl]$^+$, respectively. While the relative difference follows the experimental results, the absolute value is slightly overestimated, but within the method's precision.[164]

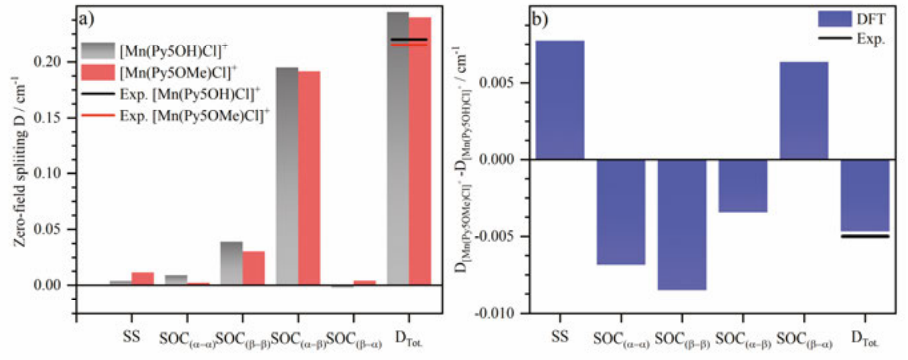

Figure 5.3 *– Experimental and calculated (BP86, CP) D values. a) Individual D value contributions. b) Difference between Py5OMe and Py5OH complexes.*

The analysis of *D* shows that SOC is the main contributor, while SS interactions marginally affect the total value for both compounds. The spin-orbit coupling of the excited states is further composed of different spin state transitions. For the Mn(II) d^5 HS ion, these states are sextet (five unpaired electrons, α) and quartet (three unpaired electrons, β). The dominant transition in both complexes is α → β. The *D* value changes linearly with the inverse of the energy difference between the sextet and quartet state,[125] which for the $[Mn(Py5OMe)Cl]^+$ complex is + 4 kcal mol^{-1} compared to $[Mn(Py5OH)Cl]^+$, as a result, the spin-orbit coupling differs between the two compounds.

Interestingly, the different contributions of the *D* value between the two complexes are not restricted to only one interaction (Figure 5.3) but a combination of many. This makes it difficult to rationalize the most significant contribution that decreases *D* for the $[Mn(Py5OMe)Cl]^+$ complex.

The calculation of the *E/D* is less accurate, with absolute values lower by more than half respect the experimental results. However, the relative trend between the two complexes is reproduced, with the $[Mn(Py5OMe)Cl]^+$ complex having a higher rhombicity (Table 5.1). The difference in rhombicity between the two complexes is interpreted to be the result of the ligand distortion caused by the methoxy groups and the subsequent addition of anisotropy in the equatorial plane.

5.6 Conclusion

With this work, we further analyzed the spin-electronic proprieties of Mn(II) complexes having Py5OH and Py5OMe ligation by studying their EPR response. The complex spectra with the X-band EPR experiment for both compounds are explained by the comparable energy dimension between the ZFS interaction and the X-band Zeeman transitions. Further investigation using HFHF measurements and supported by EPR spectra simulation allowed us to assign all the spectroscopic parameters and transitions correctly. In particular, the ZFS is affected: from $[Mn(Py5OH)Cl]^+$ to $[Mn(Py5OMe)Cl]^+$, *D* decreases while the rhombicity increases.

DFT calculations helped to rationalize these findings. The *D* value is mainly affected by the spin-orbit coupling between the sextet and quartet spin states. For the $[Mn(Py5OMe)Cl]^+$ complex, the higher energy gap between the two states results in a lower value for *D* compared to the Py5OH analog. Again, this is interpreted by lowering the antibonding orbitals due to the worse overlap between metal and ligand orbitals, which stabilize the HS state. This behavior is also responsible for the different redox proprieties of these compounds, as stated in the previous chapter. On the other hand, the high rhombicity can be explained by the equatorial anisotropy caused by the methoxy groups on the ligand.

Overall, this study demonstrates how magnetic, electronic, and geometrical proprieties are interconnected and allowed us to tune the orbital energies of the transition metal complexes of the Py5 families. These findings set the basis for further understanding of the anisotropic proprieties in metal complexes, which can be important in SMM development and for tuning catalysis.

Paper IV

Chapter 6

Base Metal Pentapyridyl Complexes: Do they Work as Molecular WOCs?

6.1 Introduction

Chapter 4 analyzed the redox trend of the $[M(Py5OH)Cl]^+$ complexes and their geometrical and electronic structure differences when dissolved in an organic electrolyte. In this chapter, we compare these changes with the effects of small water additions. This is the next step towards having a closer look at their water oxidation reactivity. The identification of catalytic intermediates is often associated with the enquiring of high-valent species. Nevertheless, the rationalization of the first catalytic events, such as the insertion of a water molecule as a substrate, is also necessary. While water oxidation is required, it might also destabilize the molecular complex and even lead to its decomposition.

We learned in Chapter 4 that solvent and electrolyte could change the properties of the complex (i.e., the coordination sphere and spin state). Therefore, a systematic analysis is also here required on the water effects. In addition to the $[M(Py5OH)Cl]^+$ complexes, we will include the analysis of the parental $[Fe(Py5OMe)Cl]^+$ compound in order to identify the differences imposed by the different coordination spheres.

The second part of this work will be entirely focused on the water oxidation activity of the complexes mentioned above. This is done by employing all three oxygen evolution assays mentioned in Section 1.2.1, as it is essential to recognize contributions from possible secondary oxidizing species. Finally, an extensive study will be conducted to attest the ‘fate’ of the most promising WOC under oxidative conditions by using a combination of techniques such as DLS, XPS, XAS, and electrochemical measurements. A significant result is that often one technique alone is insufficient to exclude/demonstrate the metal compound's degradation.

6.2 Water addition effect on the redox behavior

The electrochemical response of the $[M(Py5OH)Cl]^+$ (where M = Mn, Fe, Co, and Ni), $[Fe(Py5OH)MeCN]^{2+}$ and $[Fe(Py5OMe)Cl]^+$ is compared before and after the addition of 5.6% $^v/_v$ of water.

Before looking into this effect, the redox proprieties in the anhydrous solvent of the $[Fe(Py5OMe)Cl]^+$ compound is here briefly reinvestigated. From Figure 6.1 the CV of the Py5OMe-ligated complex in dry electrolyte has two reversible waves at $E_{1/2}$= 1.11 V and $E_{1/2}$ = 1.55 V, respectively (in this chapter, the redox potentials are reported *vs.* SHE; for a comparison with the previous results in this thesis, 0.624 V must be added to then redox potential reported *vs.* the couple Fc^+/Fc). The last peak is present as 4% of the total Faradic current, and it is associated with the chloride-free species $[Fe(Py5OMe)MeCN]^{2+}$ as reported by Feringa´s group.[105] Compared to the same Py5OH-ligated complex (which has a ratio of 75:20 of the Cl^- and MeCN coordination), a shift of 160 mV, for the chloride species and 100 mV for the MeCN-coordinated one are observed. The exchange equilibrium for the methylated complex is also shifted toward the left in the electrolyte solution, meaning that Cl^- remains coordinated to the iron center as compared to the $[Fe(Py5OH)Cl]^+$ complex, where the MeCN coordinated species is 25%. DFT calculations reproduce this experimental finding, with the chloride coordination more favorable (2.5 kcal mol^{-1}) for the Py5OMe with respect to the hydroxyl-substituted compound. As we stated in the previous chapter, the methoxy groups induce a geometrical distortion of the ligand sphere, stabilizing the HS state. Consequently, the MeCN coordination, which is present as LS, is less stable.

In the presence of 5.6% $^v/_v$ water, all Cl-coordinated complexes, with the exception of $[Mn(Py5OH)Cl]^+$ display a new irreversible anodic peak at E_p = 1.50 V. Performing the same CV experiment on the organic chloride salt TBACl, allows assigning this peak to the oxidation of Cl^- in the presence of water. Interestingly, a shift of the peak current by 160 mV is observed with respect to the water-free conditions, which is related to the hydrolysis of the obtained Cl_2 molecule (Schema 6.1).[165] The comparatively large peaks at E_p = 1.50 V show that water affects the chloride ligand exchange for all the complexes, except for the Mn complex. Below these effects are discussed in detail.

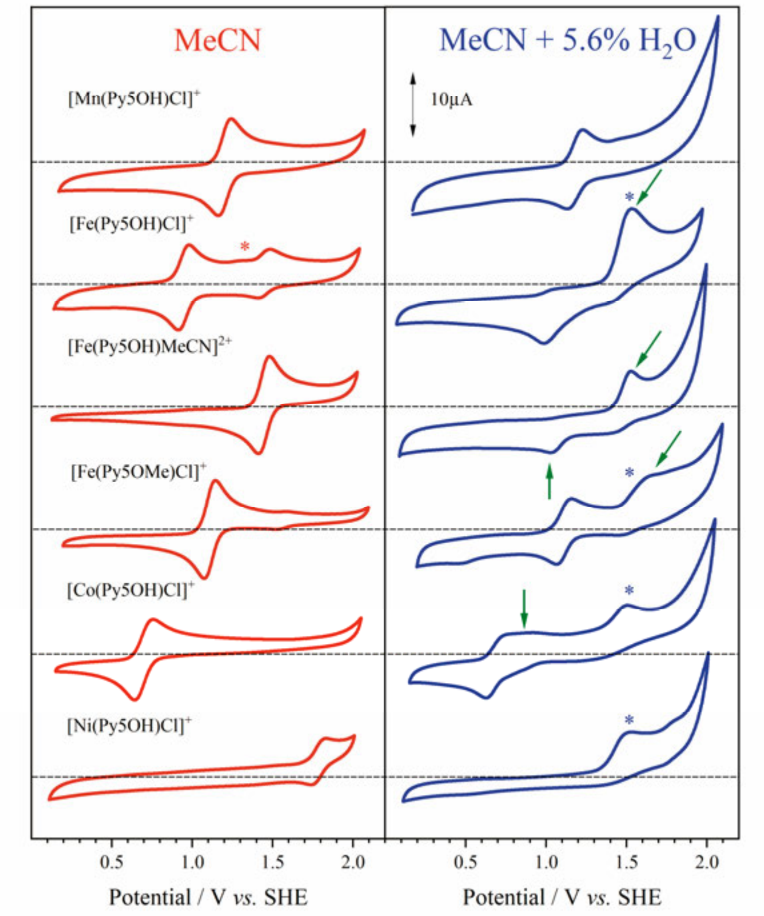

Figure 6.1 *– CV of the studied complexes in dry electrolyte (red traces) and in the presence of water (blue traces). The chloride oxidation currents are marked with *, while the formation of new species of the complexes in the presence of water are marked with green arrows and described in the text.*

Starting from [Fe(Py5OH)Cl]$^+$, the CV with 5.6% $^v/_v$ of water is very different from the one recorded in an anhydrous solution. The reversible oxidation of the [Fe(Py5OH)Cl]$^+$ species is absent, and instead a peak at 1.50 V is observed. A new irreversible wave at $E_p = 0.95$ V appears on the returning scan only when the potential is scanned to at least 1.50 V. DFT calculations were performed to study the possible exchange reactions, i.e. the binding of MeCN or water/hydroxy in the apical position. The results indicate that, for the Fe(II) complex, the MeCN coordination is more favorable than a H_2O ligand, by 7.9 kcal mol^{-1}, and OH^- ligand, by 11.7 kcal mol^{-1}. Therefore, we assign the wave at 1.50 V to the oxidation of [Fe(Py5OH)MeCN]$^{2+}$(green arrow in Figure 6.1), initiated from the exchange with Cl^- ligand in the presence of water. The chloride ions in the solution get oxidized at a potential overlapping with the

MeCN-ligated complex as a broader wave is observed. For the oxidized Fe(III) species, negatively charged ligands are favorable with respect to MeCN (Cl^- = -6.9 kcal mol^{-1} and OH^- = -8.9 kcal mol^{-1}). However, the calculated redox potential for the reduction of a $[Fe^{III}(Py5OH)OH]^{2+}$ ($E_{1/2}$ = 0.13 V) does not match with the experimental wave at 0.95 V. Chloride is still present in the solution, in the hydrated form, and the returning wave at 0.95 V is close the reduction of the $[Fe^{III}(Py5OH)Cl]^{2+}$ species (E_p = 0.90 V). We, therefore, propose the reduction of a promptly formed Fe^{III}–Cl species and a rapid exchange with MeCN ligand once Fe(II) is generated back (Scheme 6.1).

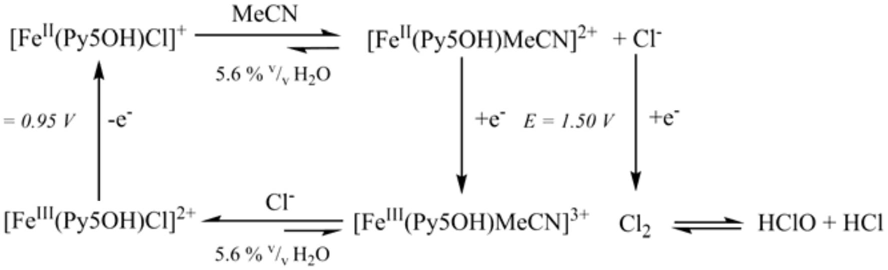

Scheme 6.1 *– Proposed oxidation and reduction pathway for the $[Fe(Py5OH)X]^{n+}$ with water mainly favors the chloride exchange reaction.*

Surprisingly, the CV of the $[Fe(Py5OH)MeCN]^{2+}$ complex in the presence of water is very similar to what was recorded for the $[Fe(Py5OH)Cl]^+$compound. On the other hand, the current peak at 1.50 V now appears narrower, indicating the Cl^- oxidation is absent. Interestingly, the UV-Vis spectra of the two related complexes with 5.6% $^{v}/_{v}$ of water are also identical, confirming this conclusion. However, even in the presence of water, the $[Fe(Py5OH)MeCN]^{2+}$ remains the prominent species (Figure 3 in Paper IV). Importantly, the peak at 0.95 V is present even in the absence of Cl^- in the solution (green arrow in Figure 6.1). This might indicate that for Fe(III), a water-derived anionic species must be responsible for the peak at 0.95 V. However, the DFT-calculated redox potential for a foreseen Fe-hydroxo species is 0.25 V, which is too low even by including the precision of the method. The unpredicted new oxygen-coordinated species likely undergoes further ligand rearrangement before reduction with a reduction potential of 0.95 V.

The $[Fe(Py5OMe)Cl]^+$ complex, after water addition, still shows the reversible oxidation of the complex with chloride bound. This is also attested in a UV-Vis experiment in which conversion of the Cl-free species is not complete (Figure 3 in Paper IV). Together with this, a broad quasi irreversible peak appears at E_p = 1.62 V, which is assigned to the superposition of the Cl^- oxidation (E_p = 1.50 V) and the redox response of the $[Fe(Py5OMe)MeCN]^{2+}$ species. In this case, no other redox-active species were observed.

The addition of water into a $[Co(Py5OH)Cl]^+$ electrolyte solution shows the chloride oxidation plus a small redox signal at $E_{1/2} = 0.86$ V. DFT calculations support the hypothesis that $[Co(Py5OH)MeCN]^{2+}$ complex is formed with a calculated $E_{1/2} = 0.99$ V.

Finally, the data show that also the $[Ni(Py5OH)Cl]^+$ complex is affected by the water addition. Even if the chloride-ligated redox species can be still be observed, the oxidation of dissolved chloride is also noticeable at E = 1.50 V, indicating a partial ligand exchange reaction.

6.3 XAS analysis on the reduced and oxidized compounds

As we did in the previous study reported in Chapter V, here we analyze the XAS results conducted at 20 K of the reduced and oxidized samples in the presence of water and compare them with the samples in anhydrous conditions. We did this to (i) confirm our interpretation of the electrochemical results and (ii) obtain structural information for the reduced M(II) and oxidized M(III) complexes.

The oxidation potential and the spin state of the synthesized reduced complexes are not affected by the presence of water except for the ferrous chloride compounds. Accordingly, for the $[Mn(Py5OH)Cl]^+$ complex, the main species remained the HS complex with Cl^- as apical ligand.

For the $[Fe(Py5OH)Cl]^+$ complex, the edge shape change is consistent with a Fe(II) LS conversion. The fitting of the EXAFS region of the spectrum shows the presence of two LS components and can be simulated as 76% of the LS Cl-free species where acetonitrile is coordinated ($[Fe(Py5OH)MeCN]^{2+}$), and the remaining 24% of the initial $[Fe(Py5OH)Cl]^+$ equally distributed between LS and HS (12%). The chloride ligation appears absent in the anodic scan of the CV experiment of this complex.

Water coordination is also not detected in the XAS of the reduced LS $[Fe(Py5OH)MeCN]^{2+}$ complex, which remains unchanged upon water addition.

The Py5OMe-ligated complex, $[Fe(Py5OMe)Cl]^+$, retains the chloride coordination when it is dissolved in the anhydrous electrolyte solution (HS state), as observed in the electrochemical experiment. However, in the presence of water, the EXAFS analysis confirms that the complex undergoes a partial ligand exchange yielding 64% of $[Fe(Py5OMe)MeCN]^{2+}$ (LS) and 34% of $[Fe(Py5OMe)Cl]^+$ (HS). Thus, the XAS results agree with the CV (Figure 6.1) and UV-Vis (Figure 3c, Paper IV) even though the exchange is more pronounced in this case.

Surprisingly, no significant changes were observed in the XAS of the $[Co(Py5OH)Cl]^+$ complex. This discrepancy to the electrochemical experiment, where $[Co(Py5OH)MeCN]^{2+}$ was assigned, might be due to the low detection limit of the XAS technique.

Finally, for the Nickel complex addition of water shifts the exchange equilibrium quantitatively toward the MeCN coordination. The ligand exchange, foreseen by the DFT calculation in Chapter 4, is here experimentally confirmed for conditions in which water helps stabilize the released Cl^- species in the organic solution.

The effect of water on the M(III) complexes was studied by adding H_2O to the electrochemically oxidized sample with a final total amount of 5.6% $^{v}/_{v}$, which corresponds to *ca.* 6700 equivalents with respect to the metal complex.

The oxidized $[Mn(Py5OH)Cl]^+$ complex, upon water addition, undergoes minor changes in XANES and EXAFS, is best fitted with the HS $[Mn^{III}(Py5OH)Cl]^{2+}$ species being dominant in the sample.

Interestingly, the XAS analysis does not show major changes between anhydrous and wet conditions for the oxidized $[Fe(Py5OH)Cl]^+$ complex. This result is in line with our interpretation of the electrochemical results in Scheme 6.1, which confirms Cl^- as the favorable ligand for Fe(III) species. Nevertheless, the rising of pre-edge on the XANES spectra indicates the presence of minor species with distorted octahedral geometry that cannot be further assigned (Figure 4b in Paper IV).

However, the EXAFS of the same oxidized sample without chloride coordination, $[Fe(Py5OH)MeCN]^{2+}$, is simulated well with a 40% contribution of a LS Fe(III)-OH species, thus indicating that the returning wave at 0.95 V is not only attributed to the reduction of Fe(III)-Cl complex. These data show that in the absence of Cl^-, which competes for the same binding site, the iron complex can coordinate a substrate water molecule.

Finally, the remaining iron complex, $[Fe(Py5OMe)Cl]^+$, is composed of 50% of LS $[Fe(Py5OMe)MeCN]^{3+}$ and the remaining half is assigned to a mono μ-oxo bridged Fe–Fe dimer. This might indicate the formation of a molecular intermediate as well as a precursor for the decomposition of the molecular species.

In the case of the cobalt complex, upon oxidation, water does not affect the XAS response. The compound remains LS in the form of $[Co^{III}(Py5OH)Cl]^{2+}$.

As for the previous study, it was impossible to obtain quantitatively oxidized material for the $[Ni(Py5OH)Cl]^+$ compound. A list of the assigned species under different conditions from this work and Chapter 4 is summarized in Table 6.1.

Table 6.1 *– Summary of the species detected with XAS measurements at 20 K as explained in this chapter and Chapter 4. The spin state can be estimated only for the Fe(II) complexes. For all the other metals, DFT calculations have been involved. The error in all percentages is estimated to be 10-20%.*

Complex	**Solid**	**MeCN + TBAPF$_6$**		**5.6% H$_2$O/MeCN + TBAPF$_6$**	
	Reduced	**Reduced**	**Oxidized**	**Reduced**	**Oxidized**
[Mn(Py5OH)Cl]$^+$	100% ^{6}Mn–Cl HS	100% ^{6}Mn-Cl HS	100% ^{5}Mn-Cl HS	100% ^{6}Mn–Cl HS	100% ^{5}Mn–Cl HS^a
[Fe(Py5OH)Cl]$^+$	100% ^{5}Fe–Cl HS	40% ^{5}Fe-Cl, HS 40% ^{1}Fe-Cl LS 20% ^{1}Fe-MeCN LS	100%, ^{2}Fe–Cl LS	12% ^{5}Fe–Cl HS 12% ^{1}Fe–Cl LS 76% ^{1}Fe–MeCN LS	~ 100% ^{2}Fe–Cl LS^a
[Fe(Py5OH)Solv]$^{2+b}$	100% ^{1}Fe–MeOH LS	100% ^{1}Fe-MeCN LS	100% $^{5\text{-}2}$Fe–MeCN HS or LS	100% ^{1}Fe–MeCN LS	60% Fe-MeCN LS 40%, Fe-OH$_x$ LS
[Fe(Py5OMe)Cl]$^+$	100% ^{5}Fe–Cl HS	100% ^{5}Fe–Cl HS	100% $^{5\text{-}2}$Fe–Cl HS or LS^c	34% ^{5}Fe–Cl HS 66% ^{1}Fe–MeCN LS	50% ^{2}Fe–MeCN LS 50% mono-μ-oxo Fe–Fe species
[Co(Py5OH)Cl]$^+$	100% ^{4}Co–Cl HS	100% ^{4}Co–Cl HS	100% ^{1}Co–Cl LS	100% ^{4}Co–Cl HS	100% ^{4}Co–Cl HS
[Ni(Py5OH)Cl]$^+$	100% ^{3}Ni–Cl HS	100% ^{3}Ni–Cl HS	--	100% ^{3}Ni–MeCN HS	--

[a] Other species are present in small amounts, making the spectrum not identical to the anhydrous oxidized sample. [b]'Solv' stands for MeOH in the solid sample, MeCN when it is dissolved in the electrolyte solution. [c]From EXAFS, it is not possible to clearly assign the spin state. However, DFT calculations suggest the LS configuration being the most stable, but only by 0.7 kcal mol^{-1}.

6.4 Water oxidation activity

So far, we have seen that Fe, Co, and Ni complexes undergo ligand exchange in the presence of 5.6% $^{v}/_{v}$ of water. MeCN is the most favorable ligand in their M(II) reduced state, but upon one-electron oxidation, the oxygen coordination becomes accessible for $[Fe(Py5OH)MeCN]^{2+}$ and $[Fe(Py5OMe)Cl]^{+}$ complexes. A particular case is the $[Fe(Py5OH)Cl]^{+}$ complex in which the Cl^{-} ligand binds back for Fe(III).

To investigate whether these complexes could perform water oxidation catalysis, we employed the light-driven experiment using TR-MIMS as explained in Section 2.6. To do so, we used 40 mM borate buffer at pH 8.0 and 0.2% $^{v}/_{v}$ MeCN to ensure good solubility for our compounds (final concentration 10 μM; for the $[Fe(Py5OMe)Cl]^{+}$ complex 1.25 μM). The TON was calculated by subtracting the average background oxygen that slightly varies for each measuring day (Figure 6.2). Given the ligand exchange trends observed above, we expected that for the $[Fe(Py5OH)Cl]^{+}$ complex, H_2O/OH^{-} coordination is most likely even in the M(II) state because water is the primary solvent in these experiments with only a low amount of MeCN as co-solvent. All the chloride ligated Py5OH compounds displayed a low activity, with the maximum TON of 2 found for the $[Fe(Py5OH)Cl]^{+}$ complex. For comparison, the divalent metal salts MCl_2 (M = Mn, Co, and Ni) and $FeSO_4$ were tested in the same condition. These metal salts displayed a very high activity so that, in most cases, the O_2 evolution was over the upper detection limit of the instrument of 250 μM of O_2 (when using the same settings as for the complexes). The only exception was the $MnCl_2$ salt. (see Figure S8, Paper IV)

The poor activity for Mn (TON = 1.3), Co (TON = 1.6), Fe (TON = 2.1), and Ni(TON = - 0.5, the blank experiment evolved more O_2) complexes (Figure 6.2) can be explained by: (i) a low propensity to the formation of the aqueous-derivate coordination (i.e., the MeCN or Cl^{-} apical ligand and the pyridines remain bound to the metal); (ii) the absence of a low energy path for subsequent catalytic steps (i.e., PCET processes or the O–O bond formation); (iii) a partial degradation resulting in a small amount of active oxides. In the latter case, small amounts of free metal ions might be released into the buffered solution with the consequent formation of active metal oxides. We have also tested $[Fe(Py5OH)MeCN]^{2+}$, but the TON was of the same order as for the Cl-complex (~ 3; not reported in Paper IV). Therefore, for $[Fe(Py5OH)Cl]^{+}$ complexes, the limitation does not lie in the Cl^{-} ligation.

Surprisingly, methylated $[Fe(Py5OMe)Cl]^{+}$ complex showed comparatively outstanding performance with a TON of 133. We, therefore, focused our attention on this complex to understand the origin of its prominent activity.

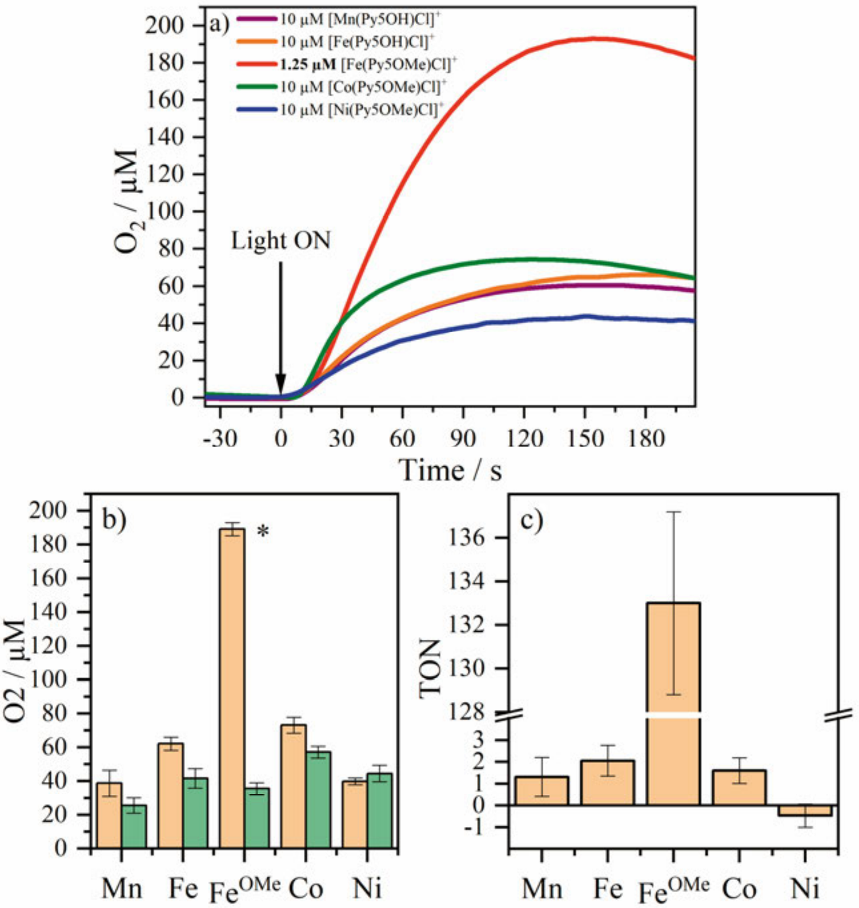

Figure 6.2 *– (a) light-driven water oxidation experiments of the complexes using TR-MIMS. (b) average of three measurements for each complex with respective blank experiments taken at the same day.(c) TON calculated after O_2 background subtraction and error bars calculated with propagation error method. For the $[Fe(Py5OMe)Cl]^+$ complex, the concentration was 1.25 µM as marked with * while for the other complexes 10 µM.*

A second water oxidation experiment was done after restoring the original pH and adding an extra amount of sacrificial electron donor ($Na_2S_2O_8$). In this case, the O_2 evolution did not exceed what was observed in a typical blank experiment where the complex is absent. This might indicate that either the complex or the photosensitizer ($[Ru(bpy)_3](ClO_4)_2$) was deactivated. We performed a DLS analysis on the post-catalytic solution, which showed no detectable nanoparticles at this low sample concentration (10 µM). However, repeating the DLS experiments at a much higher concentration of ≥ 250 µM clearly revealed nanoparticle formation (see below).

A chemical oxidation experiment was performed with Ru(III) ($E^0_{RuIII/RuII}$ = 1.53 V)[166] to exclude the contribution of the $SO_4^{\bullet-}$ radicals (redox potential ~

2.5–3.1 V)[23] to the oxygen production. The $SO_4^{\bullet -}$ radicals might enhance O_2 activity by either acting as a stronger oxidant or accelerating the complex's degradation to active metal oxides. On the other hand, they may reduce the overall activity by destroying an active molecular species. Adding 600 μM of Ru(III), the TON found for a 10 μM solution of the $[Fe(Py5OMe)Cl]^+$ complex (40 mM borate buffer with 0.2% $^v/_v$ MeCN) was 8 with, which corresponds to a yield of 50% based on the amount of oxidant. The DLS analysis conducted in the oxidized solution with 500 μM of complex and 3 mM of Ru(III) shows the presence of nanoparticles with an average hydrodynamic diameter of *ca.* 700 nm. This result might indicate the decomposition of the molecular complex in favor of active nanoparticles.

Ultimately, we performed a CPE experiment with $[Fe(Py5OMe)Cl]^+$ to further investigate the catalysis. It was necessary to apply 2.0 V to have a suitable current level (> 20 μA) and a detectable amount of O_2 using the Clark electrode as oxygen probe. On this occasion, 500 μM of the complex were used with 10% $^v/_v$ MeCN in 90 mM borate buffer (pH 8.0). The maximum Faradaic efficiency was 68% over a period of 3 minutes with 20 μM of oxygen evolved (Figure 7 in Paper IV). The same experiment was done with $FeSO_4$ salt in the same conditions described above. In this case, the maximum faradic efficiency reached 90% with 80 μM oxygen production (Figure S15 in Paper IV). Interestingly, the rinse test, which consisted of reusing the working electrode employed in the previous CPE in fresh electrolyte, did not yield any oxygen, showing the absence of active metal (oxide) deposition on the two electrodes (Figure S14 in Paper IV). However, the DLS measurement on the post-electrolysis solution of $[Fe(Py5OMe)Cl]^+$ showed the presence of particles with an average dimension of *ca.* 650 nm.

Puzzled by the absence of activity during the rinse tests but the presence of nanoparticles in the solution that might indicate active Fe_2O_3 species, we performed XPS measurements of the electrode surfaces. For the electrode used for the CPE with $[Fe(Py5OMe)Cl]^+$, there were only traces of iron with the Fe $2p_{3/2}$ peak binding energy (711.3 eV) close to what is reported for Fe_2O_3 (711.0 eV).[167] However, the shape of the satellite peaks resembled what has been observed for the dropcasted $[Fe(Py5OMe)Cl]^+$ starting material (Table 6.2). From these results, $[Fe(Py5OMe)Cl]^+$ might undergo partial electrodeposition on the electrode even if the similarity on the satellite peaks with the dropcasted precursor can also be assigned to the adsorption of the oxidized molecular complex.

For the electrode used for the CPE with $FeSO_4$, traces of iron were also observed. The Fe $2p_{3/2}$ peak has a binding energy of 712.8 eV for Fe $2p_{3/2}$ and 170.2 eV for the SO_4-S 2p, indicating the presence of ferric sulfate ($Fe_2(SO_4)_3$).[168] A common feature for both electrodes is the high oxygen content derived from the high applied voltage during CPE. A report on GC material degradation shows that at pH 8.0 the carbon surface undergoes anodization when potentials > 1.6 V are applied.[169] Surprised by the absence of Fe_2O_3

on the electrode surface even after CPE with $FeSO_4$, we investigate the literature to find similar cases. A study on a heterogeneous Co-oxide material for water oxidation reveals that the high potential induces a fast rate of oxygen evolution reaction, which lowers the pH in the proximity of the surface of the electrode. Thus, even in a buffered electrolyte, the local low pH may re-dissolve the metal oxide into the solution.

Table 6.2 *– Binding energy of the Fe 2*$p_{3/2}$ *peak as determined by XPS high-resolution spectra of carbon electrodes used for CPE experiments and respective controls.*

Samples	**Binding energy / eV**
Dropcasted $[Fe(Py5OMe)Cl]^+$	709.7
GC electrode after CPE with $[Fe(Py5OMe)Cl]^+$	711.3
GC electrode after CPE with $FeSO_4$	712.8
Fe_2O_3	711.0
$Fe_2(SO_4)_3$	713.1

6.5 Molecular catalysis versus iron nanoparticles

In the previous section, we saw that among all the tested complexes, $[Fe(Py5OMe)Cl]^+$ is particularly active toward water oxidation. Under oxidative conditions, nanoparticles are detected by DLS, but their identity was not firmly clarified via XPS analysis on the electrode surface. Here we study the electrochemical response of multiple CV scans and the UV-Vis stability of the $[Fe(Py5OMe)Cl]^+$ complex compared to the hydroxyl-substituted $[Fe(Py5OH)Cl]^+$ complex in 90 mM buffer solution (pH 8.0) with 10% $^{v}/_{v}$ MeCN.

The CV of $[Fe(Py5OH)Cl]^+$ shows a reversible wave at $E_{1/2} = 0.63$ V, likely ascribable to the redox couple $Fe^{III/II}$. During 30 potential scans, an irreversible current with an onset potential at 1.5 V slowly builds up. The subsequent rinse test, in which the used working electrodes were tested in the fresh electrolyte, shows an intense oxidation peak at $E_p = 1.8$ V, which vanishes upon the polishing of the electrode. This behavior is typical for an electrodeposition of electroactive species. The low activity measured for $[Fe(Py5OH)Cl]^+$ in the light-driven experiment might thus originate from the partial decomposition of the complex in the oxidative conditions.

The same experiment with $[Fe(Py5OMe)Cl]^+$ gave different results. The reversible wave for the $Fe^{III/II}$ oxidation was not present, and a strong wave at $E_p = 1.7$ V appears already on the first scan (Figure 6.3c, red trace). Interestingly, as the number of scan cycles increased, the wave fades until it reaches the background level. The rinse test on the used electrode shows no significant differences from the blank experiment (Figure 6.3d). Likely, the complex was already decomposed in the solution before the first scan, and the signal at E_p

= 1.7 V is attributed to the catalytic water oxidation wave originated by the active degradative species from [Fe(Py5OMe)Cl]$^+$. During the multiple potential scans to 2.0 V, the high water oxidation reaction rate and the oxidation of the electrode surface might prevent further electrode deposition and release the already formed near-electrode iron oxides species as previously discussed.

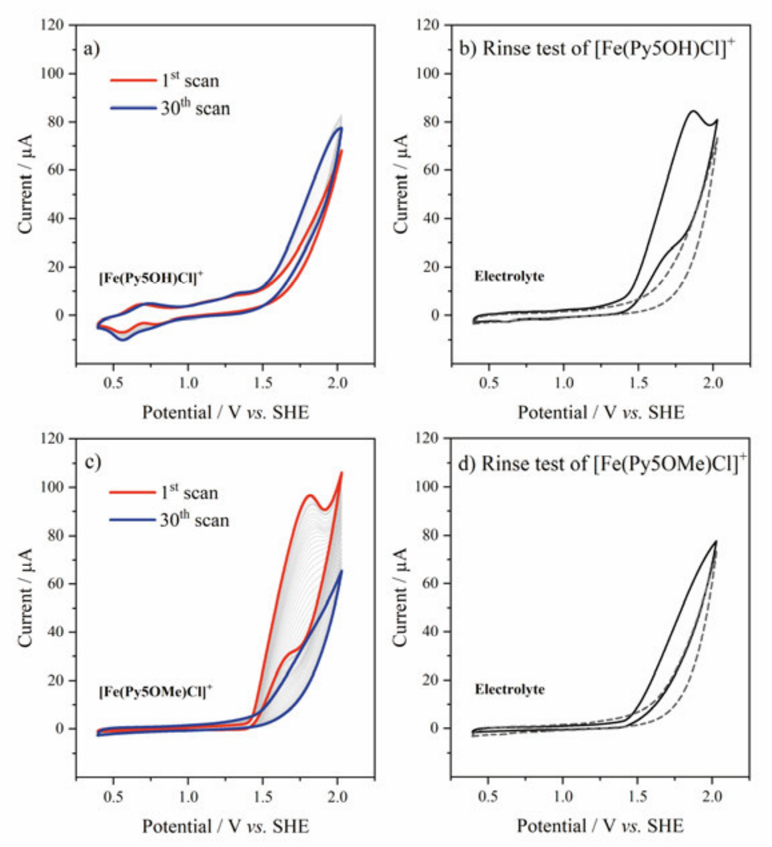

Figure 6.3 *– (a) and (c): 30 CVs scans of [Fe(Py5OH)Cl]$^+$ and [Fe(Py5OMe)Cl]$^+$ in 0.5 mM solution of 90 mM borate Buffer (pH 8.0) with 10% $^v/_v$ MeCN. (b) and (d) are the respective rinse tests of the working electrodes in fresh electrolyte. The blanks are depicted with dashed lines.*

We also follow the UV-Vis changes for both iron complexes when they were dissolved in the buffered medium by recording a spectrum every two minutes for two hours. The characteristic absorption bands of the two compounds change over time with [Fe(Py5OMe)Cl]$^+$ reaching a total conversion in only 10 minutes, while for [Fe(Py5OH)Cl]$^+$, the transformation is slower and complete only after two hours (See Figure S18 of Paper IV).

In order to follow the structural changes in [Fe(Py5OMe)Cl]$^+$ under the different conditions used in this work, we decided to make use, once again, of

XAS. Figure 6.4a shows the XANES spectra comparison of the above discussed $[Fe(Py5OMe)Cl]^+$ sample dissolved in MeCN with 5.6% $^v/_v$ water (blue line), and the same sample but under the following conditions: (i) dissolved in 90 mM borate buffer (pH 8.0) with 10% $^v/_v$ MeCN, after 2 minutes after preparation (yellow line); (ii) same as (i) but after 2 hours from the preparation (orange line); (iii) same as (i) but with the addition of 6 equivalents of Ru(III) oxidant (green line). Moreover, the XANES of the solvothermally prepared Fe(III) oxide/hydroxide (FeOOH), as reported from literature, is also portrayed (black dashed line).[170] Compared with the sample dissolved in low water content, the use of buffer at pH 8.0 as the main solvent induces a strong change in the edge position with a 2-2.5 eV shift consistent with a Fe(III) species. The two distinct peaks observed in the sample dissolved in MeCN and 5.6% $^v/_v$ merge already in the 2 minutes aged sample. The samples aged for 2 hours resemble what was reported for the FeOOH sample, while a more consistent transition towards the FeOOH species was observed after the addition of 6 eq. of Ru^{III}. The EXAFS analysis (Figure 6.4b) shows a not satisfying fit for the freshly made sample, indicating that it is composed by many species. However, in the 2 hours old sample, the FT is characterized by two strong peaks corresponding to Fe–O coordination at 1.93 Å and Fe–Fe at 2.99 Å, plus long-distance Fe–Fe peaks up to 5 Å, which are typical for a well-ordered FeOOH structure. Upon addition of the Ru^{III} oxidant, a similar FeOOH-type spectrum is obtained with a similar multimetallic FeOOH structure having Fe–Fe distance of 3.13 Å.

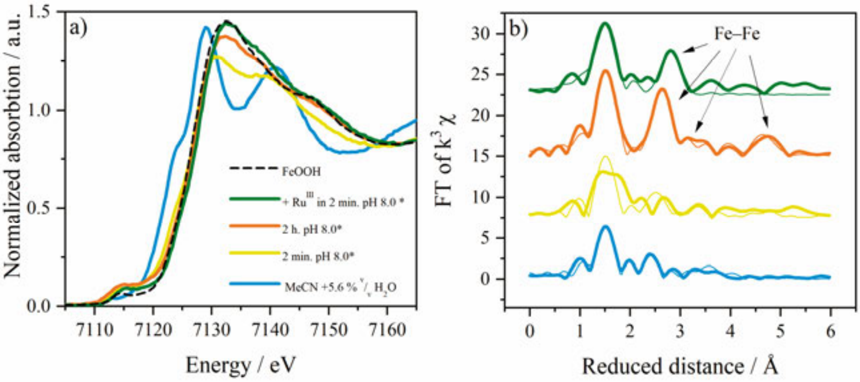

Figure 6.4 *– XANES (a) and EXAFS (b) spectra of* $[Fe(Py5OMe)Cl]^+$ *complex under different solvent conditions and with the addition of 6 eq. of* Ru^{III} *as oxidant. For * the medium consists in 90 mM borate buffer (pH 8.0) + 10%* $^v/_v$ *MeCN. XANES of the solvothermally prepared Fe(III) oxide/hydroxide (FeOOH) was reported in ref.*[170].

6.6 Conclusion

This comprehensive study focused on the effect of water addition on the series of base metal Py5OH complexes compared to the analog $[Fe(Py5OMe)Cl]^+$ complex. The electrochemical analysis revealed how the addition of 5.6% $^{v}/_{v}$ water in acetonitrile and electrolyte solvent fosters the apical ligand exchange with MeCN for all the complexes except for $[Mn(Py5OH)Cl]^+$. Interestingly, upon oxidation, oxygen coordination was seen for the iron complexes. In particular, in the oxidized $[Fe(Py5OMe)Cl]^+$ compound, low water content in the solvent promotes the formation of a dimeric μ-oxo Fe-Fe species, indicating either a molecular intermediate for the water oxidation catalysis or a precursor for a degradative pathway. Interestingly, for the $[Fe(Py5OH)Cl]^+$ complex, the Cl^- seems to be the favorable ligand after oxidation even if traces of other species with distorted octahedral geometry are observed on the XANES's pre-edge. Moreover, based on DFT calculations, we anticipate that when water is present in a more considerable amount and at basic pH, OH^- ions are more likely to bind to the oxidized metal center.

In the second part of this paper, we investigated the water oxidation activity of the studied compounds with borate buffer at pH 8.0 and 0.2% of MeCN to ensure good solubility. As expected by the XAS results, which manifest evidences of water-derived coordination, the iron complexes $[Fe(Py5OH)Cl]^+$ and $[Fe(Py5OMe)Cl]^+$ are the most active. The first performing 2 TON while the second 133 under light-driven conditions. We, therefore, confirm that Co, Mn, and Ni metal centers bearing the Py5OH ligand and an apical chloride are not suitable as molecular WOCs. One contributing factor to their low activity may be their inability to coordinate water.

The activity of the $[Fe(Py5OMe)Cl]^+$ complex was then studied by chemical and electrochemical oxidation to seek possible degradation products. Both post catalytic solutions revealed 600-700 nm diameter nanoparticles, and the XPS measurements on the employed electrode might indicate iron oxides. To define a clear picture of the behavior of the two iron complexes in buffered media, we analyzed the effect of multiple CV scans on the electrode. While for $[Fe(Py5OH)Cl]^+$ there is a clear indication of electrodeposition of redox active species, which might justify the small activity observed in the light-driven experiment, while the analog $[Fe(Py5OMe)Cl]^+$ complex degraded even before the first scan. The last evidence for nanoparticle formation came finally from the XAS analysis of the $[Fe(Py5OMe)Cl]^+$ in buffered solution before and after chemical oxidation. Once dissolved at pH 8.0, the complex undergoes a fast degradation to form active iron oxide/hydroxide species that conglomerate over time into nanoparticles.

From this study, we observed that the $[Fe(Py5OMe)Cl]^+$ complex degrades faster than the analog complex having the Py5OH ligand. From the previous chapters, we have seen that the OMe functional groups weaken the n-aromatic coordination of the central metal due to the geometrical distortion on the apical pyridine. This might results in a favorable opening of multiple coordination sites and waters to bind, resulting in the rapid hydrolysis of the iron ion and subsequent formation of iron particles at basic pH.

Thus, this work demonstrates the need to employ multiple techniques to investigate the homogenous nature of the catalysis when base metal complexes are employed for water oxidation catalysis.

Chapter 7

Summary

The scientific race to find new efficient molecular catalysts for water oxidation based on cheap base metals is still vivid. The main driving forces are their potential for upscaling to real-world applications and their suitability for developing our understanding of the fundamental relation among ligand framework, metal centers, and reactivity. The latter is also important for developing hybrid devices in which a molecular catalyst is anchored to an electrode surface or by transferring the acquired knowledge to the design of metal oxide-based heterogeneous systems.

One aspect covered in this thesis is that one of the primary limitations lies in the stability of base metal compounds. In fact, among other phenomena (e.g., oxidative degradation), base metal complexes at moderately basic pH can undergo two competitive reactions: (i) coordination of water followed by PCET processes and subsequent O–O bond formation; (ii) hydrolysis processes in which water molecules compete with the organic ligand for the metal center coordination, leading to the formation of insoluble metal-oxo species, thus losing the molecular complex. Even though freshly made metal oxides are active towards water oxidation catalysis, their performance vanishes quickly as nanoparticles start to conglomerate in a thermodynamic stable and uniform motif (i.e., fewer surface defects where the water oxidation can occur). The development of stable but also flexible molecular complexes is therefore essential to ensure long-lasting and active reactivity.

With this work, a class of well-known complexes having Py5-type ligation has been investigated for water oxidation. The penta-chelating ligand framework seemed to be the right choice for a robust coordination to the metal center. Moreover, the exogenous nature of the apical ligand is an important aspect to consider when employing this family of complexes for a catalytic reaction, as the substrate may easily coordinate via ligand exchange.

The Py5OMe ligand with different base metals for various applications, including oxidative catalytic reactions, has been well investigated, while the hydroxo-substituted version, Py5OH has been less intensively studied. Herein, I started to fill this gap with a systematic study comparing different base metals (Mn, Fe, Co, and Ni) ligated by Py5OH. Additionally, I explored the differences in the well-known Py5OMe-complex family. Even though the final goal has been to develop design principles for molecular water oxidation catalysts, this journey brought me to side studies interesting for other research branches.

In particular, with Paper I, (Chapter 3), we reported the first case of a LS ferrous complex bearing a weak-field ligand (Cl^-). This discovery is important for the development of the SCO systems and their application in switchable devices.

Another interesting finding, discussed in Paper III and Chapter 5, was the different magnetic properties of the Mn complexes having either Py5OH or Py5OMe as ligand. The difference in their anisotropic parameters was rationalized with DFT calculations. This work is interesting as it furthers the understanding of how to tune the ZFS to develop single-molecule magnets, which play a role in the information storage field.

The second part of this thesis is focused on the systematic comparison of all the Py5OH metal complexes under different conditions. In Paper II, Chapter 4, the structural and electronic trends, by adopting different base metals in their starting oxidation state, M(II), and upon one-electron oxidation in dry organic solvents to M(III), have been characterized by electrochemistry and X-ray spectroscopy and rationalized by DFT calculations as well as molecular orbital theory. An important aspect is that upon oxidation of these complexes, the spin relaxations govern the observed structural and redox potential trends. Moreover, Fe and Ni were found to have the thermodynamic propensity to exchange the apical Cl^- ligand with the organic solvent among all the complexes. Compared with the Py5OH-ligated complexes, the OMe functionalization induces a non-innocent steric distortion, destabilizing the molecular orbitals with consequences for the relative redox potentials and favorable spin states.

Finally, in Paper IV, Chapter 6, we explored the effects of water addition to the complex dissolved in an organic solvent, and we have found that, in small amount, water serves to promote the release of the apical Cl^- ligand, but that it is replaced by an organic solvent molecule, except for Mn, in which the Cl^- ligand exchange does not occur. However, upon oxidation, electrochemical and spectroscopic evidences indicated that the iron complexes, $[Fe(Py5OH)Cl]^+$ and $[Fe(Py5OMe)Cl]^+$, have water-derived coordination. These findings were confirmed by the subsequent oxygen evolution assessment, in which none of the Py5OH complexes are particularly active (i.e., a maximum TON = 2 was found for $[Fe(Py5OH)Cl]^+$) while the analog $[Fe(Py5OMe)Cl]^+$ perform 133 TON). Intrigued by this finding, we hunted to determine the catalytic nature (molecular or heterogeneous) using different water oxidation assays. A rigorous spectroscopic analysis using UV-Vis and XAS techniques attested the decomposition of the most active complex to

FeOOH nanoparticles responsible for water oxidation. Electrochemical evidences of partial decomposition of the more stable but less active $[Fe(Py5OH)Cl]^+$ complex under oxidative conditions may explain its comparatively small TON.

This work highlights the need to conduct a systematic study whenever a new base metal complex is proposed as water oxidation catalysts. This methodic work is not done only to attest to the real nature of the catalysis but also to gain a deep understanding of the electronic and structural proprieties of the investigate complexes in different conditions, such as solvent and oxidation state, and to develop on that basis design strategies for the next generation catalysts. Such studies need to be performed with a multi-techniques approach and rationalized with theoretical calculations. Even though this work might seem unnecessary due to the low water oxidation activity, this thesis taught us that by having a comprehensive range of experimental techniques, new proprieties that are not strictly related to the water oxidation catalysis could also be also discovered. This, from a personal point of view, makes this work worth to be done. Great scientific discovery has often occurred in an unexpected way.

Future works should aim to design a ligand framework that makes the molecular complex robust to compete with water hydrolysis and, at the same time, flexible to accommodate the catalytic intermediates. Due to the remarkable stability differences of the complexes having Py5OH and Py5OMe ligands, exploring other functionalization on the Py5 ligand might led to the desired result. The inclusion of two or more metallic centers can improve the catalytic activity thanks to the cooperation of different redox centers in storing the required oxidizing equivalents and by providing a structural scaffold promoting O–O bond formation. Similarly, the comparison to PSII teaches us that in the future, the tuning of spin states and the design of proton exit pathways will be essential to reach high activity. However, care must be taken that such complex structures do not lead to even less stable catalysts.

Svensk sammanfattning

Ett av världens viktigaste problem under det tjugoförsta århundradet är global uppvärmning orsakad av ökningen av koncentrationen av växthusgaser. Den största bidragsgivaren är koldioxid (CO_2) som släpps ut i atmosfären på grund av användningen av fossila bränslen. Övergången till gröna lösningar kräver att man hittar alternativa metoder för att generera energibärare som erhålls med hållbara resurser.

Naturen kan omvandla koldioxid och vatten till mer komplexa och energirika molekyler som socker och stärkelse med solljus som enda energikälla. Den primära reaktionen i denna process, känd som syregenererande fotosyntes, är den vattendelande reaktionen, som består av extraktion av fyra protoner (H^+) och fyra elektroner från två vattenmolekyler (H_2O). Som en obligatorisk biprodukt bildas syre (O_2), vilket skapat den O_2-rika atmosfären på jorden och därmed möjliggjort utvecklingen av komplexa livsformer. Forskare har studerat hur fotosyntes fungerar i många år, inte bara för nyfikenhets skull utan också för att efterlikna den. I sådana "artificiella fotosyntesprocesser" omvandlas koldioxid och vatten till hållbara "solbränslen", som antingen kan vara molekylärt väte (H_2) erhållet genom att kombinera protoner och elektroner, eller bränslen framställda genom att omvandla atmosfärisk CO_2 till energibärare med hjälp av elektroner och protoner från vatten.

På grund av H_2O-molekylernas stora stabilitet kräver delning av dem mycket energi, och därför krävs speciella ytor eller molekyler, kallade katalysatorer, för att underlätta processen. Katalysatorer kan vara heterogena material avsatta på elektroder eller molekylära komplex homogent upplösta i lösningen. Denna avhandling fokuserar på den senare eftersom deras kemiska egenskaper kan studeras djupt och selektivt modifieras.

Specifikt syftade jag till att undersöka lämpliga molekylära katalysatorer för den vattendelande reaktionen som är gjorda av rikligt tillgängliga kemiska element. För detta valde jag ett systematiskt tillvägagångssätt där alla komplex har en organisk ligandram som består av fem pyridinarmar (Py5) som håller en metall i centrum. Metallcentret varierades sedan mellan mangan (Mn), järn (Fe), kobolt (Co) och nickel (Ni). Komplexens sjätte koordinationsställe upptas vanligtvis av en kloridjon (Cl^-), med tanken att en vattenmolekyl kan ersätta den i ett första steg mot den katalytiska cykeln för O_2-utveckling. Förutom att testa effekterna av att byta ut metallcentret gjorde jag också små modifieringar av Py5-ligandramverket för att se hur detta påverkar reaktiviteten och de molekylära egenskaperna.

Det periodiska systemets ordning på grundämnena Mn → Ni följer vissa kemisk-fysiska trender. I en av mina studier observerade jag en avvikelse från en sådan trend, som ger insikter i att förstå deras lämplighet som katalysatorer för vattenuppdelning. Till exempel kan endast ett Fe-komplexet ersätta Cl^--liganden med det organiska lösningsmedlet, vilket indikerar att det kan vara särskilt aktivt när vatten tillsätts. Därefter undersökte jag effekten av att tillsätta små mängder vatten till lösningar av dessa komplex i organiska lösningsmedel i syfte att leta efter bildandet av nya former där en H_2O-molekyl binder till metallcentret istället för kloridjonen. Detta är viktigt eftersom det kan ge en första bild av hur reaktiviteten blir när komplexen löses i vatten. Jag observerade vattenligering istället för Cl- endast för de två järnkomplexen med regelbundet och något modifierat ligandramverk, men inte för någon annan testad metall.

Med hjälp av en fotosensibilisator och ljus som en energiresurs visade katalytiska experiment att endast de två Fe-komplexen utvecklar O_2. En intressant observation var att även om modifieringen av ligandramverket är relativt litet, var mängden syre väldigt annorlunda: den första ledde till produktion av två O_2, medan den andra producerade 133 O_2-molekyler innan den inaktiverades.

Att testa dessa komplex för vattenoxidation medför vissa utmaningar eftersom de kan försämras under reaktionen. Deras nedbrytning resulterar i bildningen av andra olösliga föreningar (såsom metalloxid), som initialt kan katalysera syreutvecklingsreaktionen. Därför var det sista steget att undersöka om syreaktiviteten hos det mest aktiva komplexet kommer från dess molekylära form eller dess nedbrytningsprodukter. Detta var krävande eftersom spår av metalloxider i lösningen är mycket svåra att upptäcka. Det var nödvändigt att använda olika experimentella tekniker för att bekräfta att komplexet bryts ned i lösningen med huvudsakligen vatten som lösningsmedel och att detta händer för det ”mer aktiva” järnkomplexet redan innan den katalytiska fasen började. Denna studie är relevant eftersom den visar vikten av att genomföra extremt detaljerade undersökningar av de syntetiserade molekylära katalysatorerna innan de rapporteras som ”aktiva” för vattenuppdelning till forskarsamhället. Dessutom insåg jag att utformningen av en molekylär katalysator är mycket utmanande eftersom komplexet måste ha viss flexibilitet för att reagera med H_2O-molekyler men måste också vara tillräckligt stabilt för att inte brytas ned i lösningen eller under de katalytiska cyklerna. Det är en uppgift som är mycket svår att uppnå.

Fördelen med att ha använt denna systematiska metod för att studera dessa föreningar är att jag också kunde göra oväntade upptäckter. I synnerhet observerade jag en reversibla färgförändring hos en av föreningarna när den kyldes till låg temperatur. Detta fenomen är känt som spin-crossover (SCO) och används i utformningen av sensorer. Upptäcktens unika karaktär ligger i det faktum att SCO-beteende inte var förväntat på grund av sammansättningen av denna molekyl som inkluderade en kloridjon som ligand. Därför gjordes ett betydande bidrag till detta forskningsområde. Dessutom jämförde jag och teoretiskt rationaliserade de magnetiska egenskaperna för Mn-komplexen med de två något olika liganderna. Detta resultat är intressant för forskning på enkelmolekylmagneter som används för att utveckla informationslagring i subnanometerskala.

Sammantaget låter denna avhandling oss att förstå gränserna och utmaningarna för klyvning av vatten med hjälp av billiga och miljövänliga element. Dessutom tillät de systematiska och grundläggande studierna av dessa molekyler mig att göra oväntade upptäckter som väckte min nyfikenhet och gav mig chansen att ge nya vetenskapliga bidrag.

Popular Science Summary– English

One of the worldwide most significant problems in the XXI century is global warming caused by the increase in the concentration of greenhouse gasses. The major contributor is carbon dioxide (CO_2) released into the atmosphere due to the utilization of fossil fuels. The transition towards green solutions requires finding alternative methods to generate energy carriers obtained by sustainable resources.

Nature can convert carbon dioxide and water to more complex and energy-rich molecules such as sugars and starch using sunlight as the only energy source. The primary reaction of this process known as oxygenic photosynthesis is the water-splitting reaction, which consists of the extraction of four protons (H^+) and four electrons from two water molecules (H_2O). As a mandatory side product, oxygen (O_2) is formed, which created the O_2-rich atmosphere of Earth and thereby allowed the development of complex life forms. Scientists have studied how photosynthesis works for many years, not only for the sake of knowledge but also for mimicking it. In such 'Artificial Photosynthesis' processes, carbon dioxide and water are transformed into sustainable 'solar' fuels, which can be either molecular hydrogen (H_2) obtained from combining the protons and electrons, or fuels made by converting atmospheric CO_2 into energy carriers using the electrons and protons from water.

Because of the great stability of the H_2O molecules, splitting them requires a lot of energy, and thus special surfaces or molecules, called catalysts, are required to facilitate the process. Catalysts can be heterogeneous materials deposited on electrodes or molecular complexes homogenously dissolved in the solution. This thesis focuses on the latter because their chemical proprieties can be deeply studied and selectively modified.

Specifically, I aimed to investigate suitable molecular catalysts for the water-splitting reaction that are made from abundantly available chemical elements. For this, I selected a systematic approach in which all complexes have an organic ligand framework composed of five pyridine arms (Py5) that hold a metal in its center. The metal center was then varied among manganese (Mn), iron (Fe), cobalt (Co), and nickel (Ni). The sixth coordination site of the complexes is usually occupied by a chloride ion (Cl^-), with the idea that a water molecule can replace it as a first step towards the catalytic cycle for O_2 evolution. In addition to testing the effects of exchanging the metal center, I also made small modifications to the Py5 ligand framework to see how this tunes the reactivity and molecular properties.

The periodic table´s order of the elements Mn→Ni follows certain chemical-physical trends. In one of my studies, I observed a discrepancy from such a trend, which gives insights towards understanding their suitability as catalysts for water-splitting. For example, only one the Fe complex is capable of substituting the Cl^- ligand with the organic solvent, indicating that it might be particularly active when water is added.

Next, I examined the effect of adding small amounts of water to solutions of these complexes in organic solvents with the aim of hunting for the formation of new species in which a H_2O molecule binds to the metal center instead of chloride. This is important because it can give a preview of what the reactivity will be when the complexes are dissolved in water. I observed water ligation in place of Cl^- only for the two iron complexes with regular and slightly modified ligand framework, but not for any other tested metal.

Using a photosensitizer and light as an energy resource, catalytic experiments showed that only the two Fe complexes evolve O_2. Interestingly, although the ligand framework modification appeared minor, the amount was very different: one promoted the production of two O_2, while the other produced 133 O_2 molecules before deactivating.

Testing these complexes for water oxidation entails some challenges because they may degrade during the reaction. Their degradation results in forming other insoluble species (such as metal oxide), which can initially catalyze the oxygen evolution reaction. Therefore, the last step was to investigate if the oxygen activity of the most active complex comes from its molecular form or its degradation products. This was demanding because traces of metal oxides in the solution are very difficult to detect. It was necessary to use different experimental techniques to confirm that the complex degrades in the solution with mainly water as the solvent and this happens for the ‘more active’ iron complex even before the start of the catalytic assay. This study is relevant because it proves the importance of conducting extremely detailed investigations on the synthesized molecular catalysts before reporting them as ‘active’ for water-splitting to the research community. Moreover, I realized that designing a molecular catalyst is highly challenging because the complex must have certain flexibility to react with H_2O molecules but must also be stable to not degrade in the solution or during the catalytic cycles. A task that is very difficult to achieve.

The advantage of having used this systematic approach in studying these compounds is that I was also able to make unexpected discoveries. In particular, I observed the reversible change in color of one of the compounds when it is cooled to a low temperature. This phenomenon is known as spin crossover (SCO) and is applied in the design of switchable and sensing devices. This discovery’s uniqueness lies in the fact that SCO behavior was not expected because of the composition of this molecule that included the Cl^- ligand.

Therefore, a significant contribution to this research field was made. Moreover, I also compared and theoretically rationalized the magnetic proprieties of the Mn complexes with the two slightly different ligands. This finding is interesting for research devoted to developing single molecule magnets employed for developing information storage at the sub-nanometer scale.

Overall, this thesis permits to understand the limits and challenges of water-splitting catalysis using cheap and environmentally friendly elements. Furthermore, the systematic and fundamental studies of these molecules allowed me to make unexpected discoveries that triggered my curiosity and gave me the chance to contribute to science.

Riassunto per la scienza divulgativa – Italiano

Uno dei problemi più significativi a livello mondiale del XXI secolo è il riscaldamento globale causato dall'aumento della concentrazione di gas serra. Il maggior responsabile è l'anidride carbonica (CO_2) rilasciata nell'atmosfera a causa dell'utilizzo di combustibili fossili. La transizione verso soluzioni verdi richiede la ricerca di metodi alternativi per generare vettori energetici ottenuti da risorse sostenibili.

La natura può convertire l'anidride carbonica e l'acqua in molecole più complesse e ricche di energia come zuccheri e amido utilizzando la luce solare. La reazione primaria di questo processo noto come fotosintesi clorofiliana è la reazione di scissione dell'acqua, che consiste nell'estrazione di quattro protoni (H^+) e quattro elettroni da due molecole di acqua (H_2O). Come prodotto secondario, si forma l'ossigeno (O_2), il quale ha creato l'atmosfera sulla Terra come la consciamo oggi e ha permesso lo sviluppo di forme di vita complesse. Gli scienziati hanno studiato per molti anni come funziona la fotosintesi, non solo per amor della conoscenza ma anche per imitarla. In tali processi di "fotosintesi artificiale", l'anidride carbonica e l'acqua vengono trasformate in combustibili "solari" sostenibili, che possono essere idrogeno molecolare (H_2) ottenuto dalla combinazione di protoni ed elettroni, o combustibili realizzati convertendo la CO_2 atmosferica in vettori energetici utilizzando il elettroni e protoni dall'acqua.

A causa della grande stabilità delle molecole di H_2O, la loro scissione richiede molta energia, e quindi sono necessarie superfici o molecole speciali, chiamate catalizzatori, per facilitare il processo. I catalizzatori possono essere materiali eterogenei depositati su elettrodi o complessi molecolari disciolti omogeneamente nella soluzione. Questa tesi si concentra su questi ultimi perché le loro proprietà chimiche possono essere studiate in profondità e modificate selettivamente.

In particolare, mi sono concentrato a studiare catalizzatori molecolari adatti per la reazione di scissione dell'acqua che sono costituiti da elementi chimici abbondantemente disponibili sulla crosta terrestre. Per questo, ho selezionato un approccio sistematico in cui tutti i complessi hanno una struttura organica del ligando composta da cinque bracci piridinici (Py5) che trattengono un metallo al centro. Il centro metallico è stato poi variato tra manganese (Mn), ferro (Fe), cobalto (Co) e nichel (Ni). Il sesto ed ultimo sito di coordinazione dei complessi è solitamente occupato da uno ione cloruro (Cl^-), con l'idea che una molecola d'acqua possa sostituirlo come primo passo verso il ciclo catalitico per l'evoluzione dell'O_2. Oltre a testare gli effetti dello scambio del centro metallico, ho anche apportato piccole modifiche alla struttura del ligando Py5 per vedere come questo regola la reattività e le proprietà molecolari.

L'ordine degli elementi nella tavola periodica Mn→Ni segue determinati andamenti chimico-fisici. In uno dei miei studi, ho osservato una discrepanza da tale tendenza, che fornisce spunti per comprendere la loro idoneità come catalizzatori per la scissione dell'acqua. Ad esempio, solo un complesso di ferro è in grado di sostituire il ligando Cl^- con il solvente organico, indicando che potrebbe essere particolarmente attivo quando viene aggiunta acqua.

Successivamente, ho esaminato l'effetto dell'aggiunta di piccole quantità di acqua alle soluzioni di questi complessi in solventi organici con l'obiettivo di trovare tracce per la formazione di nuove specie in cui una molecola di H_2O si lega al centro del metallo invece del cloruro. Questo è importante perché può dare un'anteprima di quale sarà la reattività quando i complessi saranno disciolti in acqua. Ho osservato la ligazione di acqua al posto del Cl^- solo per i due complessi di ferro con struttura del ligando regolare e leggermente modificata, ma non per nessun altro metallo testato.

Utilizzando un fotosensibilizzatore e la luce come risorsa energetica, gli esperimenti catalitici hanno mostrato che solo i due complessi di ferro producono O_2. È interessante notare che, sebbene la modifica della struttura del ligando apparisse minore, la quantità era molto diversa: una ha promosso la produzione di due molecole di O_2, mentre l'altra ha prodotto 133 molecole di O_2 prima di disattivarsi.

Testare questi complessi per l'ossidazione dell'acqua comporta alcune sfide perché possono degradarsi durante la reazione. La loro degradazione determina la formazione di altre specie insolubili (come ossidi di metallo), che possono inizialmente catalizzare la reazione di produzione di ossigeno. Pertanto, l'ultimo passo è stato quello di indagare se l'attività catalitica del complesso più attivo deriva dalla sua forma molecolare o dai suoi prodotti di degradazione. Questo era impegnativo perché le tracce di ossidi metallici nella soluzione sono molto difficili da rilevare. È stato necessario utilizzare diverse tecniche sperimentali per confermare che il complesso degrada nella soluzione in acqua, e ciò accade per il complesso del ferro 'più attivo' anche prima dell'inizio del saggio catalitico. Questo studio è rilevante perché dimostra l'importanza di condurre indagini estremamente dettagliate sui catalizzatori molecolari sintetizzati prima di segnalarli come 'attivi' per la scissione dell'acqua alla comunità scientifica. Inoltre, mi sono reso conto che progettare un catalizzatore molecolare è molto impegnativo perché il complesso deve avere una certa flessibilità per reagire con le molecole di H_2O ma deve anche essere stabile per non degradarsi nella soluzione o durante i cicli catalitici. Un compito molto difficile da realizzare.

Il vantaggio di aver utilizzato questo approccio sistematico nello studio di questi composti è che sono stato anche in grado di fare scoperte inaspettate. In particolare, ho osservato il cambiamento reversibile di colore di uno dei composti quando viene raffreddato a bassa temperatura. Questo fenomeno è noto come spin crossover (SCO) e viene applicato nella progettazione di dispositivi commutabili e di sensoristica. L'unicità di questa scoperta risiede nel fatto che il comportamento SCO non era previsto a causa della composizione di questa molecola che include il Cl^- come ligando. Pertanto, è stato dato un contributo significativo in questo campo di ricerca. Inoltre, ho anche confrontato e teoricamente razionalizzato le proprietà magnetiche dei complessi di Mn con i due ligandi leggermente diversi. Questa scoperta è interessante per la ricerca dedicata allo sviluppo di magneti a singola molecola impiegati per sviluppare l'archiviazione di informazioni su scala sub-nanometrica.

Nel complesso, questa tesi consente di comprendere i limiti e le sfide della catalisi dell'ossidazione dell'acqua utilizzando elementi della tavola periodica economici ed ecocompatibili. Inoltre, gli studi sistematici e fondamentali di queste molecole mi hanno permesso di fare scoperte inaspettate che hanno acceso la mia curiosità e mi hanno dato la possibilità di contribuire alla scienza.

Acknowledgements

My long trip during these years could not have been possible without the help and support of different people. Their different nationality, background, points of view, and ideas enriched me enormously. Naturally, it will be impossible to express my complete gratitude to all of you in few words, but I will try my best in the following text.

My most immense gratitude goes first to **Prof. Johannes Messinger**, my supervisor, and my mentor. You welcomed me in your research group almost six years ago in Umeå. From that moment until now, you always believed in me and my capacities. Despite our different research background, you consistently demonstrated capable of helping me with any scientific and personal issue. You are a true example of a leader, and I owe you all my professional growth.

Thanks to **Prof. Sascha Ott** for being my cosupervisor, having welcomed me in your synthetic lab, and making me always feel part of the SMC group.

Thanks to **Dr. Anders Thapper** for giving me precious advice and always being available for feedback.

Thanks to **Prof. Marcus Lundberg**. You introduced me to the world of computational chemistry. You also have been an excellent support during the writing of my papers. You always pushed me to keep a rational and critical thinking and helped me to understand the fundamental chemistry beyond my experimental results.

Thanks to **Dr. Ping Huang**, although our little misunderstandings every once and then, you always support me in interpreting the EPR experiments and their chemical interpretation.

Thanks to **Dr. 'Michael' Mun Hon Cheah**. I have always addressed you as the person 'who knows everything in the entire House 7'. You have always been available for every kind of advice, from the most technical to the more theoretical ones. You inspired my curiosity towards different topics all over these years. I will enormously miss this.

Thanks to **Dr. Petcko Chernev**. Your technical knowledge in X-ray absorption techniques and data analysis goes beyond the imagination. It was inspiring to work with you during our night shifts at the MAX IV synchrotron facility. I still remember how excited we were when we realized we could run a 'cool' spectroelectrochemical experiment at 4:00 A.M. during our last four hours of the beam.

Thanks to my mate **Dr. Casper**. We started our Ph.D. almost at the same time. Since our beginning in Umeå, we shared fears, problems, excitements. We even moved 'down' to Uppsala together with a fantastic van trip. I will keep all these memories in my heart!

A big thanks to my favorite Indian buddy **Dr. Anurag**. You made my stay in Umeå unforgettable. Particular pleasuring moments were all the time I won against you in a table tennis match (:-P) and our long (and pretty useless) light talks in our coffee breaks. You have always been there whenever I needed a place where to stay in Umeå. You were also always willing to listen to my dramas. I wish you all the best for the future!

Another important person during my stay in Umeå is **Dr. 'Dima' Dmitry Shevela**. I appreciate your tips on how to move my first steps in Sweden. I miss our long geopolitical conversations and our Friday beach volleyball matches.

In the 'Umeå' category people I would also like to thank **Dr. 'Canny' Wai Ling Kwong** and **Dr. Long Vo Pham** for your help and support during the first steps of my Ph.D.

I would like to thank all the 'past' and 'new' people in SMC group and in the physical chemistry departments. All of you made me always feel welcome and give me plenty of advice and help. In particular, I would like to mention all the people with whom I shared the synthetic lab, such as **Dr. Michele**,' il Veneto,' you made me feel like at home (even if you are not a Rovigotto, but close enough); the Hungarians **Dr. Dániel Kovács** and **Dániel Kócsi**, which synthetic chemistry skills have been very helpful; **Dr. Kamal** to be my coworkers in the synthesis of the compounds reported in this thesis; and finally, the previous master students, **Philipp** and **Thomas**.

Thanks to the people in the **Cyano group**, in particular, **João** and **Dr. Claudia**. It was very funny to chill out together in the corridor, to have light talks, and laugh during the breaks.

Thanks to the BBC's members and my office colleagues: **Prof. Gustav Berggren**, **Prof. Ann Magnuson**, **Prof. Fikret Mamedov, Prof. Felix, Dr.**

Nessima, Dr. Livia, **Dr. Henrick**, **Dr. Moritz**, **Princess**, **Holly**, **Dr. Alina**, **Dr. Sagar**, **Dr. Fatemeh**, **Orkun** and **Dr. Luca**. You have made my hours spent in the office much more pleasant.

Thanks to **Dr. Sergii** for helping me a lot with my first published paper. It has always been fun and exciting to discuss chemistry with you.

Thanks to **Marco**, the person I always went to release tension during the hardest moments. You have been a very patient colleague and good friend.

This second part of my acknowledgments goes to all the people that indirectly contributed to my wonderful Ph.D experience in the last six years.

First, I would like to mention **Stefania** and **Maja**. They both supported me very much during my Ph.D. Even if our lives have taken different paths, I will always be thankful to you, and I wish you all the best for the future.

A huge thanks to my favorite Spanish girls in Uppsala. **Mercè**, I will never be tired of listening to your life's adventures. You made me grow up in many aspects by showing me the different points of view of society. **Berta**, I will always admire your positive energy and dedication to sports and studies. I am still wondering where you find all this energy. Both of you have always been there when I needed you. You are wonderful!

I would like to thank all my volleyball buddies: **Anindya**, **Can (Djan)**, **Agnes**, **Marta**, **Mattias**, **Edison**, **Mahdi**; the people from the gym: **Lorenzo**, **Javi**, **Tiscar**, **Anna**, **Starla**, **Kelly**. Finally, I would like to express my gratitude to **Marielena**, **Alice**, and **Marcos** to always organize amazing crazy dinners/movie nights/parties and make me feel happy.

All of you guys are making Uppsala a wonderful place where to live.

A special dedication is for my favorite Spanish in Stockholm, **Cristina**. You entered *all of a sudden* in the hardest period of my life. You made me laugh when I needed it, and you were always there for me. We had wonderful trips, crazy shopping, and fancy dinners, which all I needed to recover mentally. You did this without any complaints, even if I have been intensively busy since we met. You are the best, really!

Vorrei concludere questi ringraziamenti citando chi di piu' di tutti mi ha supportato in questi anni, la mia famiglia. Un grazie enorme a mia mamma **Roberta**, mio papa' **Ivo** e mia sorella **Monica**. Nonostante la distanza, mi avete sempre fatto sentire vincino a voi e orgogliosi dell'avventura che ho intrapreso in Svezia. Vi voglio un mondo di bene!

Bibliography

[1] Ciamician, G. (1912) The Photochemistry of the Future. *Science*. 36(926), 385.

[2] Zeder, M. A. (2011) The Origins of Agriculture in the Near East. *Current Anthropology*. 52(S4), S221-S235.

[3] Meyer, R. K. P. L. A. IPCC, 2014: Climate Change 2014: Synthesis Report. Contribution of Working Groups I, II and III to the Fifth Assessment Report of the Intergovernmental Panel on Climate Change. (2014),

[4] Deng, S.; Liu, S.; Mo, X.; Jiang, L.;Bauer-Gottwein, P. (2021) Polar Drift in the 1990s Explained by Terrestrial Water Storage Changes. *Geophys. Res. Lett.* 48(7), 1-10.

[5] Steffen, W.; Rockström, J.; Richardson, K.; Lenton, T. M.; Folke, C.; Liverman, D.; Summerhayes, C. P.; Barnosky, A. D.; Cornell, S. E.; Crucifix, M.; Donges, J. F.; Fetzer, I.; Lade, S. J.; Scheffer, M.; Winkelmann, R.;Schellnhuber, H. J. (2018) Trajectories of the Earth System in the Anthropocene. *Proc. Natl. Acad. Sc.*

[6] Friedlingstein, P.; O'Sullivan, M.; Jones, M. W.; Andrew, R. M.; Hauck, J.; Olsen, A.; Peters, G. P.; Peters, W.; Pongratz, J.; Sitch, S.; Le Quéré, C.; Canadell, J. G.; Ciais, P.; Jackson, R. B.; Alin, S.; Aragão, L. E. O. C.; Arneth, A.; Arora, V.; Bates, N. R.; Becker, M.; Benoit-Cattin, A.; Bittig, H. C.; Bopp, L.; Bultan, S.; Chandra, N.; Chevallier, F.; Chini, L. P.; Evans, W.; Florentie, L.; Forster, P. M.; Gasser, T.; Gehlen, M.; Gilfillan, D.; Gkritzalis, T.; Gregor, L.; Gruber, N.; Harris, I.; Hartung, K.; Haverd, V.; Houghton, R. A.; Ilyina, T.; Jain, A. K.; Joetzjer, E.; Kadono, K.; Kato, E.; Kitidis, V.; Korsbakken, J. I.; Landschützer, P.; Lefèvre, N.; Lenton, A.; Lienert, S.; Liu, Z.; Lombardozzi, D.; Marland, G.; Metzl, N.; Munro, D. R.; Nabel, J. E. M. S.; Nakaoka, S. I.; Niwa, Y.; O'Brien, K.; Ono, T.; Palmer, P. I.; Pierrot, D.; Poulter, B.; Resplandy, L.; Robertson, E.; Rödenbeck, C.; Schwinger, J.; Séférian, R.; Skjelvan, I.; Smith, A. J. P.; Sutton, A. J.; Tanhua, T.; Tans, P. P.; Tian, H.; Tilbrook, B.; van der Werf, G.; Vuichard, N.; Walker, A. P.; Wanninkhof, R.; Watson, A. J.; Willis, D.; Wiltshire, A. J.; Yuan, W.; Yue, X.;Zaehle, S. (2020) Global Carbon Budget 2020. *Earth Syst. Sci. Data*. 12(4), 3269-3340.

[7] *Global Energy Review: CO_2 Emissions in 2020.* (2021), www.iea.org

[8] Rohde, R. Global Temperature Report for 2020. (2021), www.berkeleyearth.org

[9] Smith, D. M.; Scaife, A. A.; Hawkins, E.; Bilbao, R.; Boer, G. J.; Caian, M.; Caron, L.-P.; Danabasoglu, G.; Delworth, T.; Doblas-Reyes, F. J.; Doescher, R.; Dunstone, N. J.; Eade, R.; Hermanson, L.; Ishii, M.; Kharin, V.; Kimoto, M.; Koenigk, T.; Kushnir, Y.; Matei, D.; Meehl, G. A.; Menegoz, M.; Merryfield, W. J.; Mochizuki, T.; Müller, W. A.; Pohlmann, H.; Power, S.; Rixen, M.; Sospedra-Alfonso, R.; Tuma, M.; Wyser, K.; Yang, X.;Yeager, S. (2018) Predicted Chance That Global Warming Will Temporarily Exceed 1.5 °C. *Geophys. Res. Lett.* 45(21), 11,895-11,903.

[10] Xu, Y.; Ramanathan, V.;Victor, D. G. (2018) Global Warming Will Happen Faster than we Think. *Nature*. 564(7734), 30-32.

[11] Salzmann, M. (2016) Global Warming Without Global Mean Precipitation Increase? *Sci. Adv.* 2(6), 1-6.

[12] Karplus, V. J.; Zhang, S.;Almond, D. (2018) Quantifying Coal Power Plant Responses to Tighter SO_2 Emissions Standards in China. *Proc. Natl. Acad. Sc.* 115(27), 7004-7009.

[13] Meehl, G. A.; Hu, A.;Teng, H. (2016) Initialized Decadal Prediction for Transition to Positive Phase of the Interdecadal Pacific Oscillation. *Nat. Commun.* 7(1), 11718.

[14] Chen, X.;Tung, K.-K. (2018) Global Surface Warming Enhanced by Weak Atlantic Overturning Circulation. *Nature*. 559(7714), 387-391.

[15] IEA. Global Energy Review 2021 – Analysis. www.iea.org

[16] EV-Volumes. The Electric Vehicle World Sales Database. www.ev-volumes.com

[17] BP. Energy Outlook 2020 www.bp.com

[18] Lee, B.; Heo, J.; Kim, S.; Sung, C.; Moon, C.; Moon, S.;Lim, H. (2018) Economic Feasibility Studies of High Pressure PEM Water Electrolysis for Distributed H_2 Refueling Stations. *Energ. Convers. Manage.* 162, 139-144.

[19] IEA. The Future of Hydrogen – Analysis. www.iea.org

[20] Shiva Kumar, S.;Himabindu, V. (2019) Hydrogen production by PEM water electrolysis – A review. *Mater. Sci. Technol.* 2(3), 442-454.

[21] Mavrokefalos, C. K.;Patzke, G. R. (2019) Water Oxidation Catalysts: The Quest for New Oxide-Based Materials. *Inorganics*. 7(3), 29.

[22] Parent, A. R.; Crabtree, R. H.;Brudvig, G. W. (2013) Comparison of Primary Oxidants for Water-Oxidation Catalysis. *Chem. Soc. Rev.* 42(6), 2247-2252.

[23] Neta, P.; Huie, R. E.;Ross, A. B. (1988) Rate Constants for Reactions of Inorganic Radicals in Aqueous Solution. *J. Phys. Chem. Ref. Data*. 17(3), 1027-1284.

[24] Limburg, B.; Bouwman, E.;Bonnet, S. (2016) Rate and Stability of Photocatalytic Water Oxidation using $[Ru(bpy)_3]^{2+}$ as Photosensitizer. *ACS Catal.* 6(8), 5273-5284.

[25] Akhtar, U. S.; Tae, E. L.; Chun, Y. S.; Hwang, I. C.;Yoon, K. B. (2016) Insights into Decomposition Pathways and Fate of $Ru(bpy)_3^{2+}$ during Photocatalytic Water Oxidation with $S_2O_8^{2-}$ as Sacrificial Electron Acceptor. *ACS Catal.* 6(12), 8361-8369.

[26] Morris, N. D.; Suzuki, M.;Mallouk, T. E. (2004) Kinetics of Electron Transfer and Oxygen Evolution in the Reaction of $[Ru(bpy)_3]^{3+}$ with Colloidal Iridium Oxide. *J. Phys. Chem. A*. 108(42), 9115-9119.

[27] Morris, K. J.; Roach, M. S.; Xu, W.; Demas, J. N.;DeGraff, B. A. (2007) Luminescence Lifetime Standards for the Nanosecond to Microsecond Range and Oxygen Quenching of Ruthenium(II) Complexes. *Anal. Chem.* 79(24), 9310-9314.

[28] Kump, L. R. (2008) The Rise of Atmospheric Oxygen. *Nature*. 451(7176), 277-278.

[29] Catling, D. C.;Zahnle, K. J. (2020) The Archean Atmosphere. *Sci. Adv.* 6(9), 1-16.

[30] Sosa Torres, M. E.; Saucedo-Vázquez, J. P.;Kroneck, P. M. H. (2015). The Magic of Dioxygen. In P. M. H. Kroneck and M. E. Sosa Torres (Eds.), *Sustaining Life on Planet Earth: Metalloenzymes Mastering Dioxygen and Other Chewy Gases* (pp. 1-12). Springer International Publishing. https://doi.org/10.1007/978-3-319-12415-5_1

[31] Schirrmeister, B. E.; de Vos, J. M.; Antonelli, A.;Bagheri, H. C. (2013) Evolution of Multicellularity Coincided with Increased Diversification of Cyanobacteria and the Great Oxidation Event. *Proc. Natl. Acad. Sc.* 110(5), 1791-1796.

[32] Shevela, D.; Björn, L. O.;Govindjee. (2017). *Photosynthesis. Solar Energy for Life*. World Scientific https://doi.org/doi:10.1142/10522

[33] Lee, W. J.;Whitmarsh, J. (1989) Photosynthetic Apparatus of Pea Thylakoid Membranes: Response to Growth Light Intensity. *Plant Physiol.* 89(3), 932-940.

[34] Rappaport, F.; Guergova-Kuras, M.; Nixon, P. J.; Diner, B. A.;Lavergne, J. (2002) Kinetics and Pathways of Charge Recombination in Photosystem II. *Biochemistry*. 41(26), 8518-8527.

[35] Umena, Y.; Kawakami, K.; Shen, J.-R.;Kamiya, N. (2011) Crystal Structure of Oxygen-Evolving Photosystem II at a Resolution of 1.9 Å. *Nature*. 473(7345), 55-60.

[36] Kok, B.; Forbush, B.;McGloin, M. (1970) Cooperation of Charges in Photosynthetic O_2 Evolution: a Linear Four Steps Mechanism. *Photochem. Photobiol.* 11(6), 457-475.

[37] Joliot, P.; Barbieri, G.;Chabaud, R. (1969) Un Nouveau Modele des Centres Photochimiques du Systeme II. *Photochem. Photobiol.* 10(5), 309-329.

[38] de Lichtenberg, C.;Messinger, J. (2020) Substrate Water Exchange in the S2 State of Photosystem II is Dependent on the Conformation of the Mn_4Ca Cluster. *Phys. Chem. Chem. Phys.* 22(23), 12894-12908.

[39] Retegan, M.; Krewald, V.; Mamedov, F.; Neese, F.; Lubitz, W.; Cox, N.;Pantazis, D. A. (2016) A Five-Coordinate Mn(IV) Intermediate in Biological Water Oxidation: Spectroscopic Signature and a Pivot Mechanism for Water Binding. *Chem. Sci.* 7(1), 72-84.

[40] Kern, J.; Chatterjee, R.; Young, I. D.; Fuller, F. D.; Lassalle, L.; Ibrahim, M.; Gul, S.; Fransson, T.; Brewster, A. S.; Alonso-Mori, R.; Hussein, R.; Zhang, M.; Douthit, L.; de Lichtenberg, C.; Cheah, M. H.; Shevela, D.; Wersig, J.; Seuffert, I.; Sokaras, D.; Pastor, E.; Weninger, C.; Kroll, T.; Sierra, R. G.; Aller, P.; Butryn, A.; Orville, A. M.; Liang, M.; Batyuk, A.; Koglin, J. E.; Carbajo, S.; Boutet, S.; Moriarty, N. W.; Holton, J. M.; Dobbek, H.; Adams, P. D.; Bergmann, U.; Sauter, N. K.; Zouni, A.; Messinger, J.; Yano, J.;Yachandra, V. K. (2018) Structures of the Intermediates of Kok's Photosynthetic Water Oxidation Clock. *Nature*. 563(7731), 421-425.

[41] Siegbahn, P. E. M. (2009) Structures and Energetics for O_2 Formation in Photosystem II. *Acc. Chem. Res.* 42(12), 1871-1880.

[42] Li, X.;Siegbahn, P. E. M. (2015) Alternative Mechanisms for O_2 Release and O–O Bond Formation in the Oxygen Evolving Complex of Photosystem II. *Phys. Chem. Chem. Phys.* 17(18), 12168-12174.

[43] Messinger, J. (2004) Evaluation of Different Mechanistic Proposals for Water Oxidation in Photosynthesis on the Basis of Mn_4O_XCa Structures for the Catalytic Site and Spectroscopic Data. *Phys. Chem. Chem. Phys.* 6(20), 4764-4771.

[44] Messinger, J.; Badger, M.;Wydrzynski, T. (1995) Detection of One Slowly Exchanging Substrate Water Molecule in the S3 State of Photosystem II. *Proc Natl Acad Sci U S A*. 92(8), 3209-3213.

[45] Sproviero, E. M.; Gascón, J. A.; McEvoy, J. P.; Brudvig, G. W.;Batista, V. S. (2008) Quantum Mechanics/Molecular Mechanics Study of the Catalytic Cycle of Water Splitting in Photosystem II. *J. Am. Chem. Soc.* 130(11), 3428-3442.

[46] Sproviero, E. M.; Gascón, J. A.; McEvoy, J. P.; Brudvig, G. W.;Batista, V. S. (2008) A Model of the Oxygen-Evolving Center of Photosystem II Predicted by Structural Refinement Based on EXAFS Simulations. *J. Am. Chem. Soc.* 130(21), 6728-6730.

[47] Siegbahn, P. E. M. (2017) Nucleophilic Water Attack is Not a Possible Mechanism for O-O Bond Formation in Photosystem II. *Proc Natl Acad Sci U S A*. 114(19), 4966-4968.

[48] Siegbahn, P. E. M. (2006) O-O Bond Formation in the S4 State of the Oxygen-Evolving Complex in Photosystem II. *Chem. Eur. J.* 12(36), 9217-9227.

[49] Zhang, B.;Sun, L. (2018) Why Nature Chose the Mn_4CaO_5 Cluster as Water-Splitting Catalyst in Photosystem II: a New Hypothesis for the Mechanism of O–O Bond Formation. *Dalton. Trans.* 47(41), 14381-14387.

[50] Gersten, S. W.; Samuels, G. J.;Meyer, T. J. (1982) Catalytic Oxidation of Water by an Oxo-Bridged Ruthenium Dimer. *J. Am. Chem. Soc.* 104(14), 4029-4030.

[51] Yamada, H.; Siems, W. F.; Koike, T.;Hurst, J. K. (2004) Mechanisms of Water Oxidation Catalyzed by the cis,cis-$[(bpy)_2Ru(OH_2)]_2O_4^+$ Ion. *J. Am. Chem. Soc.* 126(31), 9786-9795.

[52] Cape, J. L.; Siems, W. F.;Hurst, J. K. (2009) Pathways of Water Oxidation Catalyzed by Ruthenium "Blue Dimers" Characterized by ^{18}O-Isotopic Labeling. *Inorg. Chem.* 48(18), 8729-8735.

[53] Liu, F.; Concepcion, J. J.; Jurss, J. W.; Cardolaccia, T.; Templeton, J. L.;Meyer, T. J. (2008) Mechanisms of Water Oxidation from the Blue Dimer to Photosystem II. *Inorg. Chem.* 47(6), 1727-1752.

[54] Sens, C.; Romero, I.; Rodríguez, M.; Llobet, A.; Parella, T.;Benet-Buchholz, J. (2004) A New Ru Complex Capable of Catalytically Oxidizing Water to Molecular Dioxygen. *J. Am. Chem. Soc.* 126(25), 7798-7799.

[55] Romain, S.; Bozoglian, F.; Sala, X.;Llobet, A. (2009) Oxygen−Oxygen Bond Formation by the Ru-Hbpp Water Oxidation Catalyst Occurs Solely via an Intramolecular Reaction Pathway. *J. Am. Chem. Soc.* 131(8), 2768-2769.

[56] Maji, S.; Vigara, L.; Cottone, F.; Bozoglian, F.; Benet-Buchholz, J.;Llobet, A. (2012) Ligand Geometry Directs O-O Bond-Formation Pathway in Ruthenium-Based Water Oxidation Catalyst. *Angew. Chem. Int. Ed. Engl.* 51(24), 5967-5970.

[57] Xu, Y.; Åkermark, T.; Gyollai, V.; Zou, D.; Eriksson, L.; Duan, L.; Zhang, R.; Åkermark, B.;Sun, L. (2009) A New Dinuclear Ruthenium Complex as an Efficient Water Oxidation Catalyst. *Inorg. Chem.* 48(7), 2717-2719.

[58] Xu, Y.; Fischer, A.; Duan, L.; Tong, L.; Gabrielsson, E.; Åkermark, B.;Sun, L. (2010) Chemical and Light-Driven Oxidation of Water Catalyzed by an Efficient Dinuclear Ruthenium Complex. *Angew. Chem. Int. Ed. Engl.* 49(47), 8934-8937.

[59] Sartorel, A.; Carraro, M.; Scorrano, G.; Zorzi, R. D.; Geremia, S.; McDaniel, N. D.; Bernhard, S.;Bonchio, M. (2008) Polyoxometalate Embedding of a Tetraruthenium(IV)-oxo-core by Template-Directed Metalation of $[\gamma\text{-}SiW_{10}O_{36}]^{8-}$: A Totally Inorganic Oxygen-Evolving Catalyst. *J. Am. Chem. Soc.* 130(15), 5006-5007.

[60] Geletii, Y. V.; Botar, B.; Kögerler, P.; Hillesheim, D. A.; Musaev, D. G.;Hill, C. L. (2008) An All-Inorganic, Stable, and Highly Active Tetraruthenium Homogeneous Catalyst for Water Oxidation. *Angew. Chem. Int. Ed. Engl.* 47(21), 3896-3899.

[61] Catalano, V. J.;Craig, T. J. (2003) Monometallic and Dimetallic Ruthenium(II)−Terpyridine Complexes Employing the Tetradentate Ligands Dipyridylpyrazolyl, Dipyridyloxadiazole, and Their Dimethyl Derivatives. *Inorg. Chem.* 42(2), 321-334.

[62] Zong, R.;Thummel, R. P. (2005) A New Family of Ru Complexes for Water Oxidation. *J. Am. Chem. Soc.* 127(37), 12802-12803.

[63] Concepcion, J. J.; Jurss, J. W.; Templeton, J. L.;Meyer, T. J. (2008) One Site is Enough. Catalytic Water Oxidation by $[Ru(tpy)(bpm)(OH_2)]^{2+}$ and $[Ru(tpy)(bpz)(OH_2)]^{2+}$. *J. Am. Chem. Soc.* 130(49), 16462-16463.

[64] Wasylenko, D. J.; Ganesamoorthy, C.; Henderson, M. A.; Koivisto, B. D.; Osthoff, H. D.;Berlinguette, C. P. (2010) Electronic Modification of the $[Ru^{II}(tpy)(bpy)(OH_2)]^{2+}$ Scaffold: Effects on Catalytic Water Oxidation. *J. Am. Chem. Soc.* 132(45), 16094-16106.

[65] Yagi, M.; Tajima, S.; Komi, M.;Yamazaki, H. (2011) Highly Active and Tunable Catalysts for O_2 Evolution From Water Based on Mononuclear Ruthenium(II) Monoaquo Complexes. *Dalton. Trans.* 40(15), 3802-3804.

[66] Duan, L.; Xu, Y.; Gorlov, M.; Tong, L.; Andersson, S.;Sun, L. (2010) Chemical and Photochemical Water Oxidation Catalyzed by Mononuclear Ruthenium Complexes with a Negatively Charged Tridentate Ligand. *Chem. Eur. J.* 16(15), 4659-4668.

[67] Duan, L.; Fischer, A.; Xu, Y.;Sun, L. (2009) Isolated Seven-Coordinate Ru(IV) Dimer Complex with $[HOHOH]^-$ Bridging Ligand as an Intermediate for Catalytic Water Oxidation. *J. Am. Chem. Soc.* 131(30), 10397-10399.

[68] Duan, L.; Bozoglian, F.; Mandal, S.; Stewart, B.; Privalov, T.; Llobet, A.;Sun, L. (2012) A Molecular Ruthenium Catalyst with Water-Oxidation Activity Comparable to that of Photosystem II. *Nat. Chem.* 4(5), 418-423.

[69] McDaniel, N. D.; Coughlin, F. J.; Tinker, L. L.;Bernhard, S. (2008) Cyclometalated Iridium(III) Aquo Complexes: Efficient and Tunable Catalysts for the Homogeneous Oxidation of Water. *J. Am. Chem. Soc.* 130(1), 210-217.

[70] Hull, J. F.; Balcells, D.; Blakemore, J. D.; Incarvito, C. D.; Eisenstein, O.; Brudvig, G. W.;Crabtree, R. H. (2009) Highly Active and Robust Cp* Iridium Complexes for Catalytic Water Oxidation. *J. Am. Chem. Soc.* 131(25), 8730-8731.

[71] Volpe, A.; Sartorel, A.; Graiff, C.; Bonchio, M.; Biffis, A.; Baron, M.;Tubaro, C. (2020) Chelating di(N-heterocyclic carbene) Complexes of Iridium(III): Structural Analysis, Electrochemical Characterisation and Catalytic Oxidation of Water. *J. Organomet. Chem.* 917, 121260.

[72] Lewandowska-Andralojc, A.; Polyansky, D. E.; Wang, C.-H.; Wang, W.-H.; Himeda, Y.;Fujita, E. (2014) Efficient Water Oxidation with Organometallic Iridium Complexes as Precatalysts. *Phys. Chem. Chem. Phys.* 16(24), 11976-11987.

[73] Menendez Rodriguez, G.; Gatto, G.; Zuccaccia, C.;Macchioni, A. (2017) Benchmarking Water Oxidation Catalysts Based on Iridium Complexes: Clues and Doubts on the Nature of Active Species. *ChemSusChem.* 10(22), 4503-4509.

[74] Naruta, Y.; Sasayama, M.-a.;Sasaki, T. (1994) Oxygen Evolution by Oxidation of Water with Manganese Porphyrin Dimers. *Angew. Chem. Int. Ed.* 33(18), 1839-1841.

[75] Limburg, J.; Vrettos, J. S.; Liable-Sands, L. M.; Rheingold, A. L.; Crabtree, R. H.;Brudvig, G. W. (1999) A Functional Model for O-O Bond Formation by the Oxygen-Evolving Complex in Photosystem II. *Science*. 283(5407), 1524.

[76] Limburg, J.; Vrettos, J. S.; Chen, H.; de Paula, J. C.; Crabtree, R. H.;Brudvig, G. W. (2001) Characterization of the O_2-Evolving Reaction Catalyzed by $[(terpy)(H_2O)Mn^{III}(O)_2Mn^{IV}(OH_2)(terpy)](NO_3)_3$ (terpy = 2,2‘:6,2‘ ‘-Terpyridine). *J. Am. Chem. Soc.* 123(3), 423-430.

[77] Arafa, W. A. A.; Kärkäs, M. D.; Lee, B.-L.; Åkermark, T.; Liao, R.-Z.; Berends, H.-M.; Messinger, J.; Siegbahn, P. E. M.;Åkermark, B. (2014) Dinuclear Manganese Complexes for Water Oxidation: Evaluation of Electronic Effects and Catalytic Activity. *Phys. Chem. Chem. Phys.* 16(24), 11950-11964.

[78] Al-Oweini, R.; Sartorel, A.; Bassil, B. S.; Natali, M.; Berardi, S.; Scandola, F.; Kortz, U.;Bonchio, M. (2014) Photocatalytic Water Oxidation by a Mixed-Valent MnIII3MnIVO3 Manganese Oxo Core that Mimics the Natural Oxygen-Evolving Center. *Angew. Chem. Int. Ed. Engl.* 53(42), 11182-11185.

[79] Pelosin, P.; Gil-Sepulcre, M.; Garrido-Barros, P.; Moonshiram, D.; Benet-Buchholz, J.; Gimbert-Suriñach, C.;Llobet, A. (2020) Analysis of the Active Species Responsible for Water Oxidation Using a Pentanuclear Fe Complex. *iScience*. 23(8), 101378.

[80] Ellis, W. C.; McDaniel, N. D.; Bernhard, S.;Collins, T. J. (2010) Fast Water Oxidation Using Iron. *J. Am. Chem. Soc.* 132(32), 10990-10991.

[81] Ertem, M. Z.; Gagliardi, L.;Cramer, C. J. (2012) Quantum Chemical Characterization of the Mechanism of an Iron-Based Water Oxidation Catalyst. *Chem. Sci.* 3(4), 1293-1299.

[82] Fillol, J. L.; Codolà, Z.; Garcia-Bosch, I.; Gómez, L.; Pla, J. J.;Costas, M. (2011) Efficient Water Oxidation Catalysts Based on Readily Available Iron Coordination Complexes. *Nat. Chem.* 3(10), 807-813.

[83] Hong, D.; Mandal, S.; Yamada, Y.; Lee, Y.-M.; Nam, W.; Llobet, A.;Fukuzumi, S. (2013) Water Oxidation Catalysis with Nonheme Iron Complexes under Acidic and Basic Conditions: Homogeneous or Heterogeneous? *Inorg. Chem.* 52(16), 9522-9531.

[84] Das, B.; Orthaber, A.; Ott, S.;Thapper, A. (2016) Iron Pentapyridyl Complexes as Molecular Water Oxidation Catalysts: Strong Influence of a Chloride Ligand and pH in Altering the Mechanism. *ChemSusChem*. 9(10), 1178-1186.

[85] Shylin, S. I.; Pavliuk, M. V.; D'Amario, L.; Mamedov, F.; Sá, J.; Berggren, G.;Fritsky, I. O. (2019) Efficient Visible Light-Driven Water Oxidation Catalysed by an Iron(IV) Clathrochelate Complex. *Chem. Commun.* 55(23), 3335-3338.

[86] Okamura, M.; Kondo, M.; Kuga, R.; Kurashige, Y.; Yanai, T.; Hayami, S.; Praneeth, V. K. K.; Yoshida, M.; Yoneda, K.; Kawata, S.;Masaoka, S. (2016) A Pentanuclear Iron Catalyst Designed for Water Oxidation. *Nature*. 530(7591), 465-468.

[87] Stracke, J. J.;Finke, R. G. (2011) Electrocatalytic Water Oxidation Beginning with the Cobalt Polyoxometalate $[Co_4(H_2O)_2(PW_9O_{34})_2]^{10-}$: Identification of Heterogeneous CoOx as the Dominant Catalyst. *J. Am. Chem. Soc.* 133(38), 14872-14875.

[88] Wasylenko, D. J.; Ganesamoorthy, C.; Borau-Garcia, J.;Berlinguette, C. P. (2011) Electrochemical Evidence for Catalytic Water Oxidation Mediated by a High-Valent Cobalt Complex. *Chem. Commun.* 47(14), 4249-4251.

[89] Wasylenko, D. J.; Palmer, R. D.; Schott, E.;Berlinguette, C. P. (2012) Interrogation of Electrocatalytic Water Oxidation Mediated by a Cobalt Complex. *Chem. Commun.* 48(15), 2107-2109.

[90] Das, B.; Orthaber, A.; Ott, S.;Thapper, A. (2015) Water Oxidation Catalysed by a Mononuclear Co^{II} Polypyridine Complex; Possible Reaction Intermediates and the Role of the Chloride Ligand. *Chem. Commun.* 51(66), 13074-13077.

[91] Nakazono, T.; Parent, A. R.;Sakai, K. (2013) Cobalt Porphyrins as Homogeneous Catalysts for Water Oxidation. *Chem. Commun.* 49(56), 6325-6327.

[92] Daniel, Q.; Ambre, R. B.; Zhang, B.; Philippe, B.; Chen, H.; Li, F.; Fan, K.; Ahmadi, S.; Rensmo, H.;Sun, L. (2017) Re-Investigation of Cobalt Porphyrin for Electrochemical Water Oxidation on FTO Surface: Formation of CoOx as Active Species. *ACS Catal.* 7(2), 1143-1149.

[93] Yin, Q.; Tan, J. M.; Besson, C.; Geletii, Y. V.; Musaev, D. G.; Kuznetsov, A. E.; Luo, Z.; Hardcastle, K. I.;Hill, C. L. (2010) A Fast Soluble Carbon-Free Molecular Water Oxidation Catalyst Based on Abundant Metals. *Science*. 328(5976), 342-345.

[94] Song, F.; Moré, R.; Schilling, M.; Smolentsev, G.; Azzaroli, N.; Fox, T.; Luber, S.;Patzke, G. R. (2017) $\{Co_4O_4\}$ and $\{Co_xNi_{4-x}O_4\}$ Cubane Water Oxidation Catalysts as Surface Cut-Outs of Cobalt Oxides. *J. Am. Chem. Soc.* 139(40), 14198-14208.

[95] McCool, N. S.; Robinson, D. M.; Sheats, J. E.;Dismukes, G. C. (2011) A Co_4O_4 "Cubane" Water Oxidation Catalyst Inspired by Photosynthesis. *J. Am. Chem. Soc.* 133(30), 11446-11449.

[96] Genoni, A.; La Ganga, G.; Volpe, A.; Puntoriero, F.; Di Valentin, M.; Bonchio, M.; Natali, M.;Sartorel, A. (2015) Water Oxidation Catalysis upon Evolution of Molecular Co(III) Cubanes in Aqueous Media. *Faraday Discuss.* 185(0), 121-141.

[97] Wang, J.-W.; Liu, W.-J.; Zhong, D.-C.;Lu, T.-B. (2019) Nickel Complexes as Molecular Catalysts for Water Splitting and CO_2 Reduction. *Coord. Chem. Rev.* 378, 237-261.

[98] Zhang, M.; Zhang, M.-T.; Hou, C.; Ke, Z.-F.;Lu, T.-B. (2014) Homogeneous Electrocatalytic Water Oxidation at Neutral pH by a Robust Macrocyclic Nickel(II) Complex. *Angew. Chem. Int. Ed. Engl.* 53(48), 13042-13048.

[99] Luo, G.-Y.; Huang, H.-H.; Wang, J.-W.;Lu, T.-B. (2016) Further Investigation of a Nickel-Based Homogeneous Water Oxidation Catalyst with Two cis Labile Sites. *ChemSusChem*. 9(5), 485-491.

[100] Lin, J.; Kang, P.; Liang, X.; Ma, B.;Ding, Y. (2017) Homogeneous Electrocatalytic Water Oxidation Catalyzed by a Mononuclear Nickel Complex. *Electrochim. Acta*. 258, 353-359.

[101] Garrido-Barros, P.; Grau, S.; Drouet, S.; Benet-Buchholz, J.; Gimbert-Suriñach, C.;Llobet, A. (2019) Can Ni Complexes Behave as Molecular Water Oxidation Catalysts? *ACS Catal.* 9(5), 3936-3945.

[102] Wang, L.; Duan, L.; Ambre, R. B.; Daniel, Q.; Chen, H.; Sun, J.; Das, B.; Thapper, A.; Uhlig, J.; Dinér, P.;Sun, L. (2016) A Nickel (II) PY5 Complex as an Electrocatalyst for Water Oxidation. *J. Catal.* 335, 72-78.

[103] Garrido-Barros, P.; Funes-Ardoiz, I.; Drouet, S.; Benet-Buchholz, J.; Maseras, F.;Llobet, A. (2015) Redox Non-Innocent Ligand Controls Water Oxidation Overpotential in a New Family of Mononuclear Cu-Based Efficient Catalysts. *J. Am. Chem. Soc.* 137(21), 6758-6761.

[104] Garrido-Barros, P.; Moonshiram, D.; Gil-Sepulcre, M.; Pelosin, P.; Gimbert-Suriñach, C.; Benet-Buchholz, J.;Llobet, A. (2020) Redox Metal–Ligand Cooperativity Enables Robust and Efficient Water Oxidation Catalysis at Neutral pH with Macrocyclic Copper Complexes. *J. Am. Chem. Soc.* 142(41), 17434-17446.

[105] E. de Vries, M.; M. La Crois, R.; Roelfes, G.; Kooijman, H.; L. Spek, A.; Hage, R.;L. Feringa, B. (1997) A Novel Pentadentate Ligand 2,6-bis[methoxybis(2-pyridyl)methyl]pyridine L for Mononuclear Iron(ii) and Manganese(ii) Compounds; Synthesis and Crystal Structures of [FeL(MeCN)][ClO_4]$_2$ and [(MnL(H_2O)][ClO_4]$_2$. *Chem. Commun.*(16), 1549-1550.

[106] Jonas, R. T.;Stack, T. D. P. (1997) C−H Bond Activation by a Ferric Methoxide Complex: A Model for the Rate-Determining Step in the Mechanism of Lipoxygenase. *J. Am. Chem. Soc.* 119(36), 8566-8567.

[107] Goldsmith, C. R.; Jonas, R. T.;Stack, T. D. P. (2002) C−H Bond Activation by a Ferric Methoxide Complex: Modeling the Rate-Determining Step in the Mechanism of Lipoxygenase. *J. Am. Chem. Soc.* 124(1), 83-96.

[108] Goldsmith, C. R.; Cole, A. P.;Stack, T. D. P. (2005) C−H Activation by a Mononuclear Manganese(III) Hydroxide Complex: Synthesis and Characterization of a Manganese-Lipoxygenase Mimic? *J. Am. Chem. Soc.* 127(27), 9904-9912.

[109] Klein Gebbink, R. J. M.; Jonas, R. T.; Goldsmith, C. R.;Stack, T. D. P. (2002) A Periodic Walk: A Series of First-Row Transition Metal Complexes with the Pentadentate Ligand PY5. *Inorg. Chem.* 41(18), 4633-4641.

[110] Goldsmith, C. R.; Jonas, R. T.; Cole, A. P.;Stack, T. D. P. (2002) A Spectrochemical Walk: Single-Site Perturbation within a Series of Six-Coordinate Ferrous Complexes. *Inorg. Chem.* 41(18), 4642-4652.

[111] Rudd, D. J.; Goldsmith, C. R.; Cole, A. P.; Stack, T. D. P.; Hodgson, K. O.;Hedman, B. (2005) X-ray Absorption Spectroscopic Investigation of the Spin-Transition Character in a Series of Single-Site Perturbed Iron(II) Complexes. *Inorg. Chem.* 44(5), 1221-1229.

[112] Real, J. A.; Gaspar, A. B.;Muñoz, M. C. (2005) Thermal, Pressure and Light Switchable Spin-Crossover Materials. *Dalton. Trans.*(12), 2062-2079.

[113] Wong, E. L.-M.; Fang, G.-S.; Che, C.-M.;Zhu, N. (2005) Highly Cytotoxic Iron(II) Complexes with Pentadentate Pyridyl Ligands as a New Class of Anti-Tumor Agents. *Chem. Commun.*(36), 4578-4580.

[114] Kwong, W.-L.; Lok, C.-N.; Tse, C.-W.; Wong, E. L.-M.;Che, C.-M. (2015) Anti-Cancer Iron(II) Complexes of Pentadentate N-Donor Ligands: Cytotoxicity, Transcriptomics Analyses, and Mechanisms of Action. *Chem. Eur. J.* 21(7), 3062-3072.

[115] Kashif, M. K.; Axelson, J. C.; Duffy, N. W.; Forsyth, C. M.; Chang, C. J.; Long, J. R.; Spiccia, L.;Bach, U. (2012) A New Direction in Dye-Sensitized Solar Cells Redox Mediator Development: In Situ Fine-Tuning of the Cobalt(II)/(III) Redox Potential through Lewis Base Interactions. *J. Am. Chem. Soc.* 134(40), 16646-16653.

[116] Baillargeon, J.; Xie, Y.; Raithel, A. L.; Ghaffari, B.; Staples, R. J.;Hamann, T. W. (2018) Spin-Doctoring Cobalt Redox Shuttles for Dye-Sensitized Solar Cells. *Inorg. Chem.* 57(18), 11633-11645.

[117] Bechlars, B.; D'Alessandro, D. M.; Jenkins, D. M.; Iavarone, A. T.; Glover, S. D.; Kubiak, C. P.;Long, J. R. (2010) High-Spin Ground States via Electron Delocalization in Mixed-Valence Imidazolate-Bridged Divanadium Complexes. *Nat. Chem.* 2(5), 362-368.

[118] Abe, T.; Tamada, Y.; Shiroishi, H.; Nukaga, M.;Kaneko, M. (1999) Catalytic Water Oxidation Using Chemically Generated Ru(bpy)$_3^{3+}$ Oxidant. *J Mol Catal A Chem.* 144(3), 389-395.

[119] Shafirovich, V. Y.; Khannanov, N. K.;Shilov, A. E. (1981) Inorganic Models of Photosystem II of Plant Photosynthesis. Catalytic and Photocatalytic Oxidation of Water with Participation of Manganese Compounds. *J. Inorg. Biochem.* 15(2), 113-129.

[120] Creutz, C.;Sutin, N. (1975) Reaction of Tris(bipyridine)ruthenium(III) with Hydroxide and its Application in a Solar Energy Storage System. *Proc. Natl. Acad. Sc.* 72(8), 2858-2862.

[121] Kowalska, J.;DeBeer, S. (2015) The Role of X-ray Spectroscopy in Understanding the Geometric and Electronic Structure of Nitrogenase. *Biochim. Biophys. Acta Mol. Cell Res.* 1853(6), 1406-1415.

[122] Salikhov, K. M.;Zavoiskaya, N. E. (2015) Zavoisky and the Discovery of EPR. *Resonance*. 20(11), 963-968.

[123] Brustolon, M.;Giamello, E. (2009). *Electron Paramagnetic Resonance : A Practitioners Toolkit*. John Wiley & Sons, Incorporated.

[124] Bar, A. K.; Pichon, C.;Sutter, J.-P. (2016) Magnetic Anisotropy in Two- to Eight-Coordinated Transition–Metal Complexes: Recent Developments in Molecular Magnetism. *Coord. Chem. Rev.* 308, 346-380.

[125] Boča, R. (2004) Zero-Field Splitting in Metal Complexes. *Coord. Chem. Rev.* 248(9), 757-815.

[126] Weinstock, H. (1996). *SQUID Sensors: Fundamentals, Fabrication and Applications*. Springer Netherlands.

[127] Atkins, P. W.;Friedman, R. (2011). *Molecular Quantum Mechanics* (5th ed ed.). Oxford University Press.

[128] Baseden, K. A.;Tye, J. W. (2014) Introduction to Density Functional Theory: Calculations by Hand on the Helium Atom. *J. Chem. Educ.* 91(12), 2116-2123.

[129] Becke, A. D. (1988) Density-Functional Exchange-Energy Approximation with Correct Asymptotic Behavior. *Phys. Rev. A*. 38(6), 3098-3100.

[130] Siegbahn, P. E. M. (2006) The Performance of Hybrid DFT for Mechanisms Involving Transition Metal Complexes in Enzymes. *J. Biol. Inorg. Chem.* 11(6), 695-701.

[131] Ioannidis, E. I.;Kulik, H. J. (2015) Towards Quantifying the Role of Exact Exchange in Predictions of Transition Metal Complex Properties. *J. Chem. Phys.* 143(3), 034104.

[132] Johnson, E. R.; Mackie, I. D.;DiLabio, G. A. (2009) Dispersion Interactions in Density-Functional Theory. *J. Phys. Org, Chem.* 22(12), 1127-1135.

[133] Grimme, S.; Antony, J.; Ehrlich, S.;Krieg, H. (2010) A Consistent and Accurate *ab initio* Parametrization of Density Functional Dispersion Correction (DFT-D) for the 94 Elements H-Pu. *J. Chem. Phys.* 132(15), 154104.

[134] Marenich, A. V.; Cramer, C. J.;Truhlar, D. G. (2009) Universal Solvation Model Based on Solute Electron Density and on a Continuum Model of the Solvent Defined by the Bulk Dielectric Constant and Atomic Surface Tensions. *J. Phys. Chem. B*. 113(18), 6378-6396.

[135] Frisch, M. J. T., G. W.; Schlegel, H. B.; Scuseria, G. E.; Robb, M. A.; Cheeseman, J. R.; Scalmani, G.; Barone, V.; Petersson, G. A.; Nakatsuji, H.; Li, X.; Caricato, M.; Marenich, A.; Bloino, J. B.; Janesko, G. R.; Gomperts, B.; Mennucci, H.; Hratchian, P.; Ortiz, J. V.; Izmaylov, A. F.; Sonnenberg, J. L.; Williams-Young, D.; Ding, F.; Lipparini, F.; Egidi, F.; Goings, J.; Peng, B.; Petrone, A.; Henderson, T.; Ranasinghe, D.; Zakrzewski, V. G.; Gao, J.; Rega, N.; Zheng, G.; Liang, W.; Hada, M.; Ehara, M.; Toyota, K.; Fukuda, R.; Hasegawa, J.; Ishida, M.; Nakajima, T.; Honda, Y.; Kitao, O.; Nakai, H.; Vreven, T.; Throssell, K.; Montgomery, J. A.; Peralta, Jr. J. E.; Ogliaro, F.; Bearpark, M.; Heyd, J. J.; Brothers, E.; Kudin, K. N.; Staroverov, V. N.; Keith, T.; Kobayashi, R.; Normand, J.; Raghavachari, K.; Rendell, A.; Burant, J. C.; Iyengar, S. S.; Tomasi, J.; Cossi, M.; Millam, J. M.; Klene, M.; Adamo, C.;

Cammi, R.; Ochterski, J. W.; Martin, R. L.; Morokuma, K.; Farkas, O.; Foresman, J. B.; Fox, D. J.; Gaussian, Inc., Wallingford CT;. (**2009**). *Gaussian 09.* In (Version Revision A.1)

[136] Bard, A. J.;Faulkner, L. R. (2001). *Electrochemical Methods: Fundamentals and Applications*.

[137] Elgrishi, N.; Rountree, K. J.; McCarthy, B. D.; Rountree, E. S.; Eisenhart, T. T.;Dempsey, J. L. (2018) A Practical Beginner's Guide to Cyclic Voltammetry. *J. Chem. Educ.* 95(2), 197-206.

[138] Pavlishchuk, V. V.;Addison, A. W. (2000) Conversion Constants for Redox Potentials Measured Versus Different Reference Electrodes in Acetonitrile Solutions at 25°C. *Inorganica Chim. Acta*. 298(1), 97-102.

[139] Salmon, L.; Molnár, G.; Zitouni, D.; Quintero, C.; Bergaud, C.; Micheau, J.-C.;Bousseksou, A. (2010) A Novel Approach for Fluorescent Thermometry and Thermal Imaging Purposes Using Spin Crossover Nanoparticles. *J. Mater. Chem.* 20(26), 5499-5503.

[140] Ohba, M.; Yoneda, K.; Agustí, G.; Muñoz, M. C.; Gaspar, A. B.; Real, J. A.; Yamasaki, M.; Ando, H.; Nakao, Y.; Sakaki, S.;Kitagawa, S. (2009) Bidirectional Chemo-Switching of Spin State in a Microporous Framework. *Angew. Chem. Int. Ed. Engl.* 48(26), 4767-4771.

[141] Bartual-Murgui, C.; Akou, A.; Thibault, C.; Molnár, G.; Vieu, C.; Salmon, L.;Bousseksou, A. (2015) Spin-Crossover Metal–Organic Frameworks: Promising Materials for Designing Gas Sensors. *J. Mater. Chem. C.* 3(6), 1277-1285.

[142] Dugay, J.; Giménez-Marqués, M.; Kozlova, T.; Zandbergen, H. W.; Coronado, E.;van der Zant, H. S. J. (2015) Spin Switching in Electronic Devices Based on 2D Assemblies of Spin-Crossover Nanoparticles. *Adv. Mater.* 27(7), 1288-1293.

[143] Shepherd, H. J.; Gural'skiy, I. y. A.; Quintero, C. M.; Tricard, S.; Salmon, L.; Molnár, G.;Bousseksou, A. (2013) Molecular Actuators Driven by Cooperative Spin-State Switching. *Nat. Commun.* 4(1), 2607.

[144] Gural'skiy, I. y. A.; Quintero, C. M.; Costa, J. S.; Demont, P.; Molnár, G.; Salmon, L.; Shepherd, H. J.;Bousseksou, A. (2014) Spin Crossover Composite Materials for Electrothermomechanical Actuators. *J. Mater. Chem. C.* 2(16), 2949-2955.

[145] Gural'skiy, I. y. A.; Shylin, S. I.; Ksenofontov, V.;Tremel, W. (2017) Spin-State-Dependent Redox-Catalytic Activity of a Switchable Iron(II) Complex. *Eur. J. Inorg. Chem.* 2017(24), 3125-3131.

[146] Andris, E.; Jašík, J.; Gómez, L.; Costas, M.;Roithová, J. (2016) Spectroscopic Characterization and Reactivity of Triplet and Quintet Iron(IV) Oxo Complexes in the Gas Phase. *Angew. Chem. Int. Ed. Engl.* 55(11), 3637-3641.

[147] Li, H.;Peng, H. (2018) Recent Advances in Self-Assembly of Spin Crossover Materials and their Applications. *Curr. Opin. Colloid Interface Sci.* 35, 9-16.

[148] Halcrow, M. A. (2016) The Effect of Ligand Design on Metal Ion Spin State—Lessons from Spin Crossover Complexes. *Crystals*. 6(5), 58.

[149] Lee, J.-J.; Sheu, H.-s.; Lee, C.-R.; Chen, J.-M.; Lee, J.-F.; Wang, C.-C.; Huang, C.-H.;Wang, Y. (2000) X-ray Absorption Spectroscopic Studies on Light-Induced Excited Spin State Trapping of an Fe(II) Complex. *J. Am. Chem. Soc.* 122(24), 5742-5747.

[150] Valverde-Muñoz, F. J.; Gaspar, A. B.; Shylin, S. I.; Ksenofontov, V.;Real, J. A. (2015) Synthesis of Nanocrystals and Particle Size Effects Studies on the Thermally Induced Spin Transition of the Model Spin Crossover Compound [Fe(phen)$_2$(NCS)$_2$]. *Inorg. Chem.* 54(16), 7906-7914.

[151] Briois, V.; Sainctavit, P.; Long, G. J.;Grandjean, F. (2001) Importance of Photoelectron Multiple Scattering in the Iron K-Edge X-ray Absorption Spectra of Spin-Crossover Complexes: Full Multiple Scattering Calculations for Several Iron(II) Trispyrazolylborate and Trispyrazolylmethane Complexes. *Inorg. Chem.* 40(5), 912-918.

[152] Mebs, S.; Braun, B.; Kositzki, R.; Limberg, C.;Haumann, M. (2015) Abrupt versus Gradual Spin-Crossover in $Fe^{II}(phen)_2(NCS)_2$ and $Fe^{III}(dedtc)_3$ Compared by X-ray Absorption and Emission Spectroscopy and Quantum-Chemical Calculations. *Inorg. Chem.* 54(24), 11606-11624.

[153] Collet, E.;Guionneau, P. (2018) Structural Analysis of Spin-Crossover Materials: From Molecules to Materials. *C. R. Chim*. 21(12), 1133-1151.

[154] Guionneau, P.; Marchivie, M.; Bravic, G.; Létard, J.-F.;Chasseau, D. (**2004**). Structural Aspects of Spin Crossover. Example of the $[Fe^{II}Ln(NCS)_2]$ Complexes. In P. Gütlich and H. A. Goodwin (Eds.), *Spin Crossover in Transition Metal Compounds II* (pp. 97-128). Springer Berlin Heidelberg. https://doi.org/10.1007/b95414

[155] Boniolo, M.; Shylin, S. I.; Chernev, P.; Cheah, M. H.; Heizmann, P. A.; Huang, P.; Salhi, N.; Hossain, K.; Thapper, A.; Lundberg, M.;Messinger, J. (2020) Spin Transition in a Ferrous Chloride Complex Supported by a Pentapyridine Ligand. *Chem. Commun.* 56(18), 2703-2706.

[156] Boniolo, M.; Chernev, P.; Cheah, M. H.; Heizmann, P. A.; Huang, P.; Shylin, S. I.; Salhi, N.; Hossain, M. K.; Gupta, A. K.; Messinger, J.; Thapper, A.;Lundberg, M. (2021) Electronic and Geometric Structure Effects on One-Electron Oxidation of First-Row Transition Metals in the Same Ligand Framework. *Dalton. Trans.* 50(2), 660-674.

[157] Greenwood, N. N.;Earnshaw, A. (1997). *Chemistry of the Elements* (2nd ed ed.). Butterworth-Heinemann.

[158] Neese, F. (2007) Calculation of the Zero-Field Splitting Tensor on the Basis of Hybrid Density Functional and Hartree-Fock Theory. *J. Chem. Phys.* 127(16), 164112.

[159] Zein, S.;Neese, F. (2008) Ab Initio and Coupled-Perturbed Density Functional Theory Estimation of Zero-Field Splittings in Mn^{II} Transition Metal Complexes. *J. Phys. Chem. A*. 112(34), 7976-7983.

[160] Zein, S.; Duboc, C.; Lubitz, W.;Neese, F. (2008) A Systematic Density Functional Study of the Zero-Field Splitting in Mn(II) Coordination Compounds. *Inorg. Chem.* 47(1), 134-142.

[161] Duboc, C.; Astier-Perret, V.; Chen, H.; Pécaut, J.; Crabtree, R. H.; Brudvig, G. W.;Collomb, M.-N. (2006) A Multifrequency High-Field EPR (9–285GHz) Investigation of a Series of Dichloride Mononuclear Penta-Coordinated Mn(II) Complexes. *Inorganica Chim. Acta*. 359(5), 1541-1548.

[162] Duboc, C. (2016) Determination and Prediction of the Magnetic Anisotropy of Mn Ions. *Chem. Soc. Rev.* 45(21), 5834-5847.

[163] Stoll, S.;Schweiger, A. (2006) EasySpin, a Comprehensive Software Package for Spectral Simulation and Analysis in EPR. *J. Magn. Reson.* 178(1), 42-55.

[164] Hureau, C.; Groni, S.; Guillot, R.; Blondin, G.; Duboc, C.;Anxolabéhère-Mallart, E. (2008) Syntheses, X-ray Structures, Solid State High-Field Electron Paramagnetic Resonance, and Density-Functional Theory Investigations on Chloro and Aqua Mn^{II} Mononuclear Complexes with Amino-Pyridine Pentadentate Ligands. *Inorg. Chem.* 47(20), 9238-9247.

[165] Morris, J. C. (1946) The Mechanism of the Hydrolysis of Chlorine. *J. Am. Chem. Soc*. 68(9), 1692-1694.

[166] Prier, C. K.; Rankic, D. A.;MacMillan, D. W. C. (2013) Visible Light Photoredox Catalysis With Transition Metal Complexes: Applications in Organic Synthesis. *Chem. Rev.* 113(7), 5322-5363.

[167] Yamashita, T.;Hayes, P. (2008) Analysis of XPS Spectra of Fe^{2+} and Fe^{3+} Ions in Oxide Materials. *Appl. Surf. Sci.* 254(8), 2441-2449.

[168] Descostes, M.; Mercier, F.; Thromat, N.; Beaucaire, C.;Gautier-Soyer, M. (2000) Use of XPS in the Determination of Chemical Environment and Oxidation State of Iron and Sulfur Samples: Constitution of a Data Basis in Binding Energies for Fe and S Reference Compounds and Applications to the Evidence of Surface Species of an Oxidized Pyrite in a Carbonate Medium. *Appl. Surf. Sci.* 165(4), 288-302.

[169] Yi, Y.; Weinberg, G.; Prenzel, M.; Greiner, M.; Heumann, S.; Becker, S.;Schlögl, R. (2017) Electrochemical Corrosion of a Glassy Carbon Electrode. *Catal. Today*. 295, 32-40.

[170] Görlin, M.; Chernev, P.; Ferreira de Araújo, J.; Reier, T.; Dresp, S.; Paul, B.; Krähnert, R.; Dau, H.;Strasser, P. (2016) Oxygen Evolution Reaction Dynamics, Faradaic Charge Efficiency, and the Active Metal Redox States of Ni–Fe Oxide Water Splitting Electrocatalysts. *J. Am. Chem. Soc*. 138(17), 5603-5614.

Acta Universitatis Upsaliensis

Digital Comprehensive Summaries of Uppsala Dissertations from the Faculty of Science and Technology 2055

Editor: The Dean of the Faculty of Science and Technology

A doctoral dissertation from the Faculty of Science and Technology, Uppsala University, is usually a summary of a number of papers. A few copies of the complete dissertation are kept at major Swedish research libraries, while the summary alone is distributed internationally through the series Digital Comprehensive Summaries of Uppsala Dissertations from the Faculty of Science and Technology. (Prior to January, 2005, the series was published under the title "Comprehensive Summaries of Uppsala Dissertations from the Faculty of Science and Technology".)

Distribution: publications.uu.se
urn:nbn:se:uu:diva-447009

ACTA
UNIVERSITATIS
UPSALIENSIS
UPPSALA
2021